Performance of a tracking telescope for crystal channeling measurements and evaluation of the CMS Binary Chip

William Ferguson

High Energy Physics Group
Department of Physics
Imperial College London

A thesis submitted to Imperial College
for the degree of Doctor of Philosophy
and the Diploma of Imperial College.

February 2014

Declaration

The work presented in this thesis is my own work, and the work of others is explicitly referenced.

Common to chapters 2, 3 and 4 were beam tests in the CERN H8 beamline, carried out between June 2010 and December 2012. My typical involvement during each test was:

- Assistance with the telescope hardware setup and dismantling
- Assistance with the commissioning of the telescope, including pedestal runs, adjusting APV25 latency settings, and plane alignment
- Daily data-taking shifts during running periods, which involved monitoring telescope performance and optimising its configuration, controlling the data acquisition system, and controlling the goniometer during crystal scans to find the channeling orientation

Individual contributions involved with Chapter 2 were:

- Development and implementation of the straight track and bent track fitting algorithms
- Use of the telescope hit and track reconstruction to characterise the telescope performance
- Contribution to the development of the standardised approach to analysis of crystal channeling
- Analysis of data to characterise the channeling performance of various crystals

Individual contributions involved with Chapter 3 were:

- Participation in the evaluation of the performance of the telescope planes in the presence of a heavy ion beam
- Development and implementation of a suitable hit reconstruction algorithm from the saturated APV25 chips
- Use of the telescope hit and track reconstruction to characterise the telescope performance
- Analysis of data to characterise the heavy ion beam

Individual contributions involved with Chapter 4 were:

- Probe station testing and selection of silicon sensors for use with CBC modules
- Full analysis of data collected with the CBC
- Development of toy Monte Carlo and Geant4 simulations to model energy deposition and δ-ray production in the CBC sensor

William Ferguson, February 2014

Abstract

The High-Luminosity LHC (HL-LHC) foresees an increase in luminosity towards 5×10^{34} cm^{-2}s^{-1} over the next decade. Increased luminosity will have heavy implications for the CMS Tracker, due to increased detector occupancies, trigger rates and radiation damage. Notable areas for development in the Tracker include sensor and readout systems. Additionally, CMS will for the first time require the use of Tracker information in the Level-1 Trigger.

A beam telescope has been designed and constructed for the primary purpose of testing future detector modules for upgrades of the CMS Tracker. The telescope is based on the readout chain of the CMS Tracker, and measures the trajectories of charged particles with the use of five pairs of orthogonal silicon strip sensors. Beam tests have been carried out in the H8 proton beamline at CERN through the UA9 collaboration, which looks into the phenomenon of crystal channeling as a possible means of improved beam collimation. The telescope was found to have good performance and has allowed the observation of crystal channeling in a variety of crystals.

The telescope has also been tested in a heavy ion beam at the H8 beamline. Large signals in the telescope sensors have been shown to momentarily saturate the APV25 readout chip, which has led to the need for modified hit reconstruction. The telescope has been shown to perform sufficiently well to allow measurements of crystal channeling of heavy ions.

The increased data rates at the HL-LHC and the need for compatibility with existing systems necessitate the use of a binary, unsparsified chip for the readout of silicon strips in the upgraded CMS Tracker. The CMS Binary Chip is a prototype of such a chip, and has been tested in conjunction with the beam telescope at the H8 proton beam. The chip has been shown to perform well.

Acknowledgements

First and foremost, I thank Geoff Hall for taking me on as a student and for supervising me for the last four years. Many thanks to Mark Pesaresi and Mark Raymond for continuously sharing their wisdom and advice throught this work, and for their hard work and good company during the long hours of the beam tests at CERN.

Thanks to Paul Dauncey and Louis Lyons for useful discussions, and to Jad Marrouche, Jonni Fulcher and Philippe Schoofs for their help with a range problems of various magnitudes.

On a more personal note, many thanks to Arash Mostofi and all of the Subwardens and Seniors that I've had the pleasure of living and working with at Wilkinson Hall for the last four years. Thank you to my friends from the Serpentine (both human and avian), for providing much valuable escapism throughout this work. Thanks to Nathalie Skrzypek for providing me with some light relief and a comfortable sofa in the final stages of writing up. Thanks to so many other friends for their inspiration and encouragement over the years.

A big thank you to Katy for her support and patience over the last year. Many thanks to Eleanor for the chats, the laughs, and the encouragement. Finally I'd like to thank my parents for their full and continual support throughout my whole education. Mum and Dad, this is for you.

Contents

List of Figures

List of Tables

Chapter 1

Introduction

1.1 Overview

This thesis presents the results of experimental work conducted in the H8 external beamline at CERN, with an underlying motivation of coping with luminosity upgrades at the LHC. A tracking telescope based on the CMS Tracker has been designed and constructed, for the purpose of accurately measuring proton trajectories in crystal channeling experiments. The telescope has also been used to measure heavy ion trajectories and to provide a platform for measurements with a prototype for the new readout chip for the CMS Tracker.

This introductory chapter provides the relevant background material on the LHC and the CMS experiment, and gives an overview of the planned luminosity upgrades at the LHC.

Chapter 2 gives an overview of collimation at the LHC, and introduces the necessary theoretical background for the phenomenon of crystal channeling, which it is hoped can eventually be used in advanced LHC collimation systems. The design and construction of the telescope is described, and beam test results characterising its performance are presented. Finally its measurements of crystal channeling are summarised.

Chapter 3 Gives an overview of crystal channeling of heavy ions as well as the issues associated with their measurement in the beam telescope. The performance of the telescope in a heavy ion beam is described, and observations made are presented.

Chapter 4 provides an overview of the CMS Binary Chip, which is a prototype readout chip for the upgraded CMS Tracker. The integration of the chip with the telescope is described and its performance is evaluated. The prospects for future iterations of the chip are given.

Chapter 5 concludes the work and provides an overview of the future prospects for crystal channeling aided beam collimation and the CMS Tracker at the higher luminosities foreseen in the coming decade.

1.2 The Large Hadron Collider

The Large Hadron Collider (LHC) is a two-ring superconducting hadron accelerator and collider based at CERN [1]. The LHC is situated in the 26.7 km circumference LEP tunnel, which lies 45-170 m underground and straddles the Swiss-French border. The LHC is designed to collide bunches of protons from each beam with a centre of mass energy of $\sqrt{s} = 14$ TeV, at a frequency of 40 MHz. It is also designed to collide lead ions at $\sqrt{s} = 2.8$ TeV [1]. The primary aims of the LHC and its detectors are to search for the Higgs boson and to look for physics beyond the Standard Model by studying the products of collision interactions.

The accelerator comprises eight straight sections and eight arcs. At four nominal interaction points along the straight sections the two beams are brought together for particles to collide. The rate of interactions generated, for a certain process, p, is given by

$$\frac{\mathrm{d}N_{\mathrm{p}}}{\mathrm{d}t} = L\sigma_{\mathrm{p}} \tag{1.1}$$

where L is the machine luminosity and σ_{p} is the cross section for p [1]. The luminosity depends on the beam parameters and can be written

$$L = \frac{N^2 n f \gamma}{4\pi \epsilon_{\mathrm{n}} \beta^*} F \tag{1.2}$$

where N is the number of protons per bunch, n is the number of bunches per beam, f is the revolution frequency, γ is the Lorentz factor, F is the geometric reduction factor that is a result of the non-zero crossing angle of the two beams at the interaction point, ϵ_{n} is the normalised transverse beam emittance and β^* is the beta function at the collision point. The emittance in a certain direction quantifies the area of the beam in position-momentum phase space, and is a constant at all positions along the beamline. The beta function characterises the focussing of the beam at the collision point, and for a given emittance scales with the square of the beam width. The LHC is designed to circulate 2808 proton bunches in each beam (out of 3564 available bunch spaces), with each beam containing 1.15×10^{11} protons. With a design luminosity of 10^{34} cm^{-2}s^{-2}, the LHC can generate around 10^9 interactions per second at each interaction point.

At each of the four interaction points sits one of the main LHC detectors: CMS [2] and ATLAS [3], which are general purpose detectors, LHCb [4], which is optimised for the study of b-physics, and ALICE [5], which is for the study of quark-gluon plasma. Each detector must have good time, energy and spatial resolution to allow precise event reconstruction with low track ambiguity. Online trigger systems are required to reduce the enormous data rate to manageable levels by selecting only the most interesting events for storage, imposing the need for readout systems to provide data buffering while the online trigger decisions are made. Detectors must also be capable of operating in a high radiation environment for prolonged periods without degradation.

1.2.1 Design and layout

Figure 1.1 shows the overall layout of the LHC, including the four main experiments and pre-accelerators. Each particle beam reaches its final energy and bunch structure via a multi-stage injection chain of pre-accelerator systems. Initially the linear

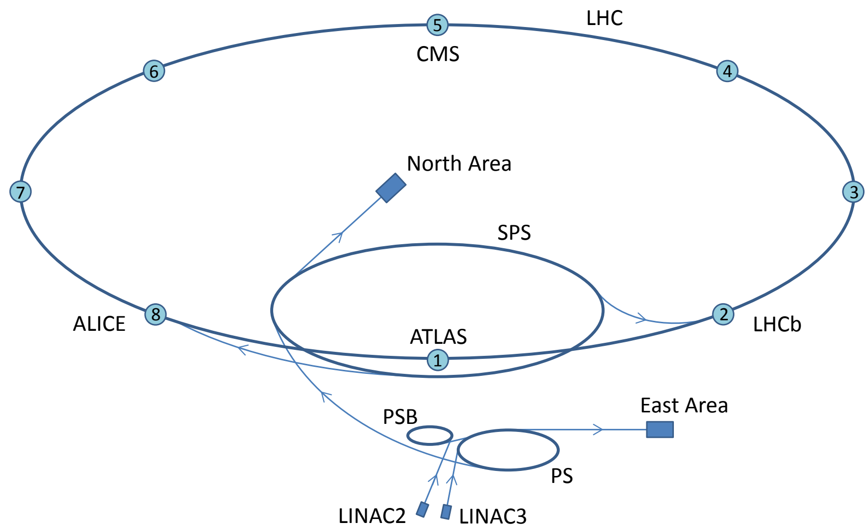

Figure 1.1: Layout of the LHC and its pre-accelerators (not to scale). Also shown are the four main experiments; CMS, ATLAS, LHCb and ALICE.

accelerator LINAC2 injects a pulse of protons into the Proton Synchrotron Booster (PSB) at 50 MeV, every 1.2 s. The PSB accelerates protons to 1.4 GeV and injects them into the Proton Synchrotron (PS). The PS gives protons the required bunch structure and accelerates them to 25 GeV before injection into the Super Proton Synchrotron (SPS). The SPS accelerates protons to 450 GeV and injects bunches into the LHC, in two opposing directions, at injection insertions located near Points 2 and 8. The LHC then accelerates protons to their full energy. A similar process accelerates heavy ions, with initial injection from LINAC3.

The LHC itself comprises 1232 dipole and 392 quadrupole superconducting magnets, which bend and focus the beams respectively. As both beams carry the same charge sign, each must be accelerated by a separate series of magnets. The accelerator is based upon a twin-bore magnet design in which both beam pipes pass through a single magnet, which saves space in the tunnel. 16 RF cavities accelerate particles and maintain a tight bunch structure. It takes approximately 4 minutes per ring to fill the LHC, and a further 20 minutes for protons to be accelerated from 450 GeV to 7 TeV.

1.2.2 Physics goals

The Standard Model of particle physics is the most precise and experimentally verified model of fundamental physics available. It describes electroweak symmetry breaking through the Higgs mechanism, which recovers the gauge invariant electromagnetic field, while generating masses for the $W^{\pm}$ and Z vector bosons and keeping the photon massless. The Higgs mechanism also predicts the existence of a massive scalar boson, the Higgs boson, which had yet to be observed before the LHC.

One of the primary objectives of the LHC is the discovery of the Higgs boson. According to the Standard Model, a Higgs particle may be created in high energy collisions through one of four main processes: gluon fusion via a top-quark loop ($gg \rightarrow H$), top-quark fusion ($gg \rightarrow Ht\bar{t}$), weak boson fusion ($qq \rightarrow Hqq$) and weak boson bremsstrahlung ($q\bar{q} \rightarrow HW, Z$). Once produced the Higgs rapidly decays, and it is the job of the LHC detectors to observe the products of these decays to infer the prior existence of the Higgs. The Higgs may decay in a number of ways, according to its mass, m_H, and Figure 1.2 shows the branching ratio of Higgs decay modes as a function of m_H. As the Standard Model does not predict the mass of the Higgs, experiments must look for an excess of a certain decay mode over the Standard Model predicted background level, at a certain mass. In July 2012 CMS reported to have observed a new boson, consistent with the Higgs, at a mass of 125 GeV/c^2, with searches performed in five decay modes; $\gamma\gamma$, ZZ, W^+W^-, $\tau^+\tau^-$, $b\bar{b}$ [6]. A similar result was reported from ATLAS [7]. As well as searches for the Higgs, the LHC will allow further precision studies of the Standard Model through quantum chromodynamics, electroweak and flavour physics. Top quark production at the Hz level allows the measurement of Standard Model couplings, provided good identification of b-jets from top quark decays.

Further studies at the LHC include searches for physics beyond the Standard Model. Supersymmetry is a proposed extension to the Standard Model that is able to resolve the hierarchy problem, and may provide a candidate for dark matter. The decay of supersymmetric particles, such as squarks and gluinos, may be inferred by LHC

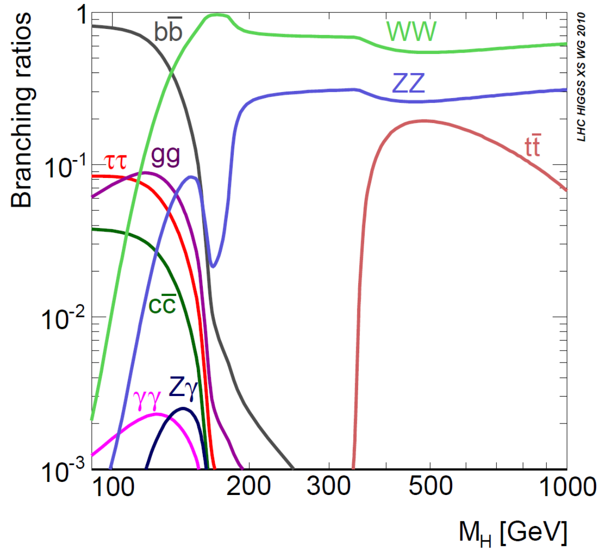

Figure 1.2: Higgs boson decay branching ratios as a function of mass [8].

experiments from missing transverse energy. Missing transverse energy may also provide a signature for the presence of extra dimensions [9].

Collisions of heavy ions at unprecedented energies at the LHC will allow the probing of quark-gluon plasmas and the extension of studies performed at the Relativistic Heavy Ion Collider (RHIC) [10]. Signatures for very strongly interacting nuclear matter include the suppression of high p_{T} particles (jet quenching). The study of jet quenching, energy flow and quarkonium production require experiments to have high performing calorimeters and flexible triggers [9].

1.3 The Compact Muon Solenoid

The Compact Muon Solenoid (CMS) is one of the two general purpose detectors at the LHC, and is situated at Point 5 on the north side of the LHC ring. CMS has been designed to investigate the full range of new physics available at the LHC. One of the main objectives of CMS is to confirm the existence of the Higgs boson, and determine its characterising parameters. Following the lower mass limit of 114.4 GeV/c^2 provided by LEP [11], CMS was designed to have sensitivities to Higgs decay channels in the mass range 100 GeV/c^2 $< m_{\mathrm{H}} <$ 1000 GeV/c^2 [9].

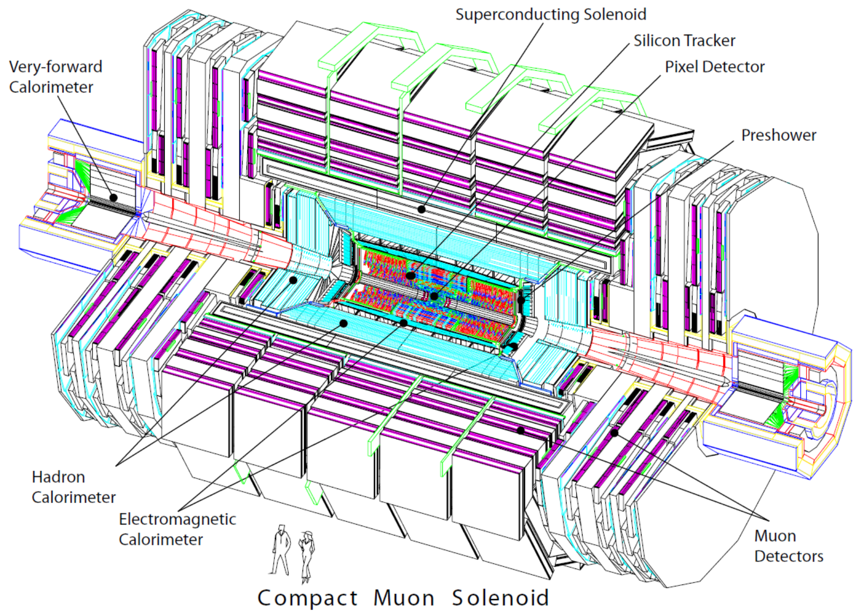

Figure 1.3: Layout of the CMS detector [9].

Other goals include the search for evidence of supersymmetry, new massive vector bosons or extra dimensions [9]. CMS also provides a useful tool for studying high energy heavy ion collisions at the LHC. Although not explicitly designed for this purpose, the use of the Tracker in conjunction with the muon system allows the reconstruction of dimuon invariant masses, thus providing a probe for the study of quark gluon plasma [12].

The design of CMS has been optimised for the identification of muons, electrons, photons and jets, and the accurate measurement of their momenta and energy over a large range, within a high luminosity environment. Fundamental to the detector is the large solenoidal magnet, which provides a field of 3.8 T. The magnetic field in CMS is required to allow the momentum of charged particles to be measured. The magnet houses (with increasing radius) an inner tracker comprising a pixel detector and a silicon strip tracker, and electromagnetic and hadronic calorimeters. Beyond the magnet is the iron return yoke, interspersed with the muon detection layers. Endcap layers at either end of the magnet also provide calorimetry and muon detection layers. This overall layout is shown in Figure 1.3.

1.3.1 Coordinate system

The coordinate system convention adopted by CMS has the origin centred at the nominal interaction point in the centre of the detector, with x pointing radially inwards towards the centre of the LHC ring, y vertically up, and z along the beam direction towards the Jura mountains. The radial distance from the z-axis is denoted r, and the azimuthal angle, ϕ, is measured from the x-axis in the x-y plane. Pseudorapidity is defined as $\eta = -\ln \tan(\theta/2)$, where θ is the polar angle measured from the positive z-axis [9].

1.3.2 Magnet

The CMS magnet is a cylindrical superconducting solenoid, 13 m long with an internal diameter of 5.9 m, and provides a magnetic field of 3.8 T in the inner region. The magnetic flux is returned via a 1.5 m thick fully saturated iron yoke, which is instrumented with four layers of of muon chambers. The magnetic field within the yoke is large enough to achieve good muon momentum resolution within a compact machine, without making stringent demands on the muon chamber resolution and alignment [9]. Good momentum resolution is necessary for efficient muon triggering at the first level trigger, and for calibration of the electromagnetic calorimeter [13].

1.3.3 Tracker

The CMS Tracker is required to accurately measure the trajectories of charged particles through the magnetic field in order to provide accurate momentum measurements and to determine the position of any vertices. The Tracker is an all silicon detector, comprising the inner Pixel detector and outside of this the Silicon Strip Tracker (SST). Figure 1.4 shows a z-r quarter section, showing pixel and strip regions. The SST comprises the Tracker Inner Barrel (TIB), the Tracker Outer Barrel (TOB), the Tracker Inner Disks (TIDs), and the Tracker Endcaps (TECs).

As well as the active sensor material, the Tracker includes all the necessary readout electronics, cooling systems and support structures. The Tracker was designed

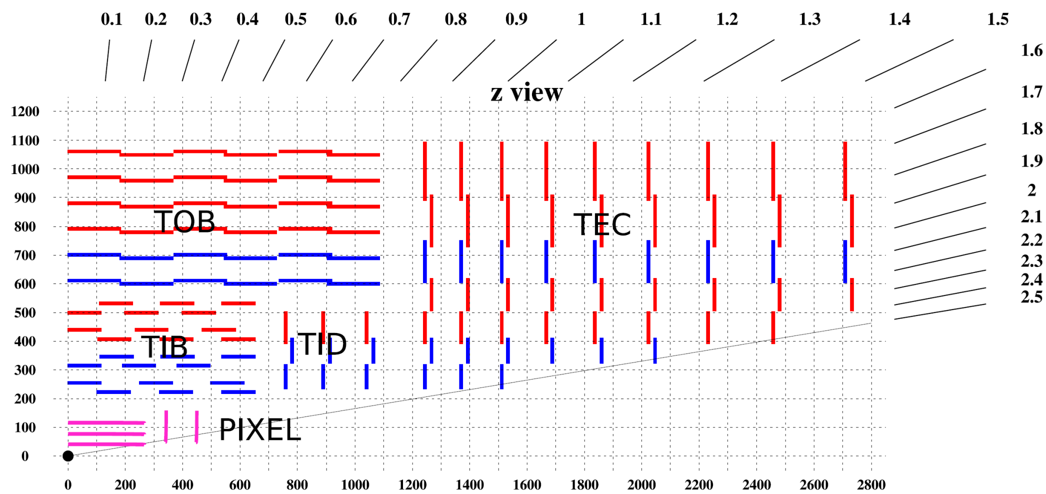

Figure 1.4: Quarter cross section of the CMS Tracker in z-r. Length measurements (mm) are to the bottom and left, with pseudorapidity to the top and right. Red and blue lines represent single and double sided modules respectively [14].

to minimise its material budget in order to minimise multiple scattering, electron bremsstrahlung and photon conversion, which would compromise the performance of not just the Tracker, but also the ECAL and Muon system [12]. Of particular importance is that sensitivity to the important $H \to \gamma\gamma$ decay channel is not lost through excessive photon conversions. Figure 1.5 shows the material budget in radiation lengths as a function of pseudorapidity, for both subdetector and material type.

Particle fluences are extremely high in the Tracker region, so high radiation tolerance of sensors and electronics is an important feature. Table 1.1 shows the hadron fluence and radiation dose at different radii throughout the tracker region, following an integrated luminosity of 500 fb^{-1} (corresponding to $\sim$10 years of operation) [9]. The high flux environment also imposes strict criteria on granularity, in order to keep occupancies down to the percent level [12].

Pixel Detector

The Pixel detector is the closest detector to the interaction point. As seen in Figure 1.4, it comprises three barrel layers in the radial range 41 mm $< r <$ 112 mm, with two end disk layers at either end at $|z| = 345$ mm and $|z| = 465$ mm. All

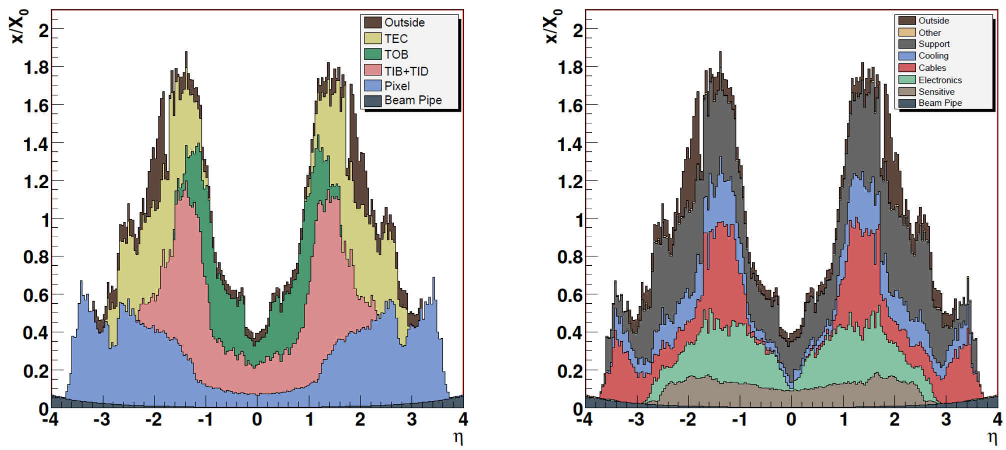

(a) (b)

Figure 1.5: CMS Tracker material budget in radiation lengths as a function of pseudorapidity, by (a) subdetector, and (b) material type [2].

Table 1.1: Hadron fluence and radiation dose in different radial layers in the CMS Tracker (barrel region), for an integrated luminosity of 500 fb^{-1} ($\sim$10 years) [9].

Radius [cm]	Fluence of fast hadrons [10^{14} cm^{-2}]	Dose [kGy]	Charged particle flux [cm^{-2}s^{-1}]
4	32	840	10^8
11	4.6	190	
22	1.6	70	6×10^6
75	0.3	7	
115	0.2	1.8	3×10^5

layers are composed of modular detector units. Pixels are 100×150 μm^2 in both barrel and end disk regions, and pixel layers are bump-bonded to analogue readout chips that amplify and process signals before readout upon a trigger. Pixels are n-on-n devices, meaning that their response is strongly affected by Lorentz drift as a result of the high electron mobility, which dominates charge carrying. This is a useful effect as increased charge sharing improves position resolution. In the end disk regions where the electric and magnetic fields would otherwise be parallel, the modules are rotated by 20° about r to induce such an effect. This layout of barrel and disk modules is shown in Figure 1.6. Spatial resolution has been measured to be $\sim$10 μm for the r-ϕ measurement and $\sim$20 μm for the z measurement in the barrel layers, thus providing precise vertex position resolution in three dimensions [9, 12].

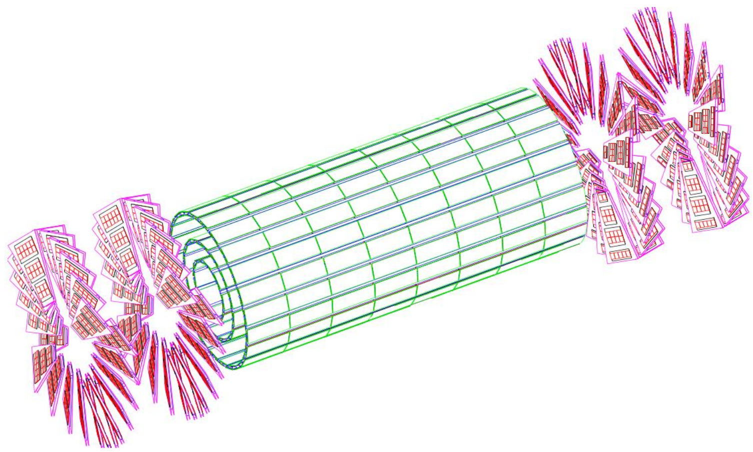

Figure 1.6: Layout of the CMS Pixel detector [9].

Silicon Strip Tracker

Beyond the Pixel detector lies the Silicon Strip Tracker. The layers in the SST are made up of modules, each of which contains p-on-n silicon strip sensors of various pitches read out by 2-12 APV25 readout chips, mounted on a support structure. Each APV25 amplifies and processes data from 128 sensor strips, and pairs of APV25s are multiplexed and sent off-detector via optical links (see Section 1.4).

In the high radiation environment the sensors and electronics need to be radiation hard to survive ∼10 years of operation without significant degradation. Damage to the bulk material reduces the signal to noise ratio and increases leakage current. Bulk damage through the introduction of acceptor defects in the n-type material gradually causes inversion to a p-type material, The gradual increase in acceptor defect concentration increases the bias voltage required to fully deplete the sensor [12]. For this reason the sensors are designed to be able to withstand a high voltage (>450 V) without breaking down [14]. Irradiation also imposes strict cooling requirements on silicon sensors. Low temperatures help to limit the radiation induced increase in required depletion voltage, and also help to remove heat that results from increased leakage current of irradiated sensors. For these reasons the sensors are operated at a temperature of $< -10°\mathrm{C}$ [12].

Figure 1.4 shows that the barrel regions of the SST comprise the TIB and the TOB, both with strips parallel to z. The TIB has four layers and extends to $|z| = 55$ cm.

Sensors are $\sim$12 cm long and 320 μm thick, with strip pitch of 80 μm in the first two layers and 120 μm in the next two layers. The narrower pitch in the inner layers increases granularity and helps to keep occupancies down. The TOB consists of six layers extending to $|z| < 118$ cm. Sensors in the TOB are $\sim$18 cm long and 500 μm thick, with pitch of 183 μm in the first four layers and 122 μm in the outer two layers. Both TIB and TOB use stereo modules on their inner two layers (shown in blue on Figure 1.4). Stereo modules make use of two sensors aligned with an angular offset of 100 mrad to provide information on the z position of the track. This provides a measurement resolution of 23-24 μm in r-ϕ and 230 μm in z.

Endcap regions are provided by the TID and the TEC, and have strips that are perpendicular to z, leading to a pitch that varies with r. The TID provides a disk layer at either end of the TIB, and within the inner radius of the TOB. Each TID comprises three disks of sensor modules, each arranged as three rings. Sensors are 320 μm thick, with mean pitch varying from 100 μm to 141 μm [15]. Beyond the z range of the TOB and the TID sit the TEC layers. Each TEC comprises nine disks, each instrumented with up to seven rings. The inner four ring layers have a thickness of 320 μm with the outer three having a thickness of 500 μm. Mean strip pitch varies from 97 μm to 184 μm. As in the TIB and TOB, the TID and TEC both employ stereo modules. The first two rings of the TID and the first two and fifth rings of the TEC have stereo modules, which allows a measurement of r to be made alongside the ϕ-z measurement [9]. Overall the SST has almost 10^7 channels, and provides sufficient granularity to keep occupancies down to the required percent level.

1.3.4 Calorimetry

The calorimetry is provided by an Electromagnetic Calorimeter (ECAL) and a Hadronic Calorimeter (HCAL). Both systems are placed within the magnet coil, which benefits energy measurements as it eliminates interactions with the magnet system.

ECAL

Despite its small branching ratio, the $H \to \gamma\gamma$ decay mode provides a distinctive signature in the intermediate Higgs mass range (90-150 GeV/c^2), and is the primary design consideration of the ECAL. This decay mode has a small branching ratio (Figure 1.2), so the requirement to observe a clear two photon mass peak above the background imposes stringent requirements on ECAL granularity and energy resolution [16].

The ECAL consists of over 75000 lead tungstate ($PbWO_4$) scintillating crystals shared between the barrel and endcap regions, and provides coverage up to $|\eta| < 3$. The crystals have radiation length 0.89 cm, Molière radius 22 mm, and are radiation hard up to 10 Mrad. Photons and electrons deposit their energy in the crystals via an electromagnetic shower. This results in the production of scintillation light, which is detected by silicon avalanche photodiodes (APDs) in the barrel region, and vacuum photodiodes in the (VPTs) in each endcap region [9].

Crystals have a length of around 26 radiation lengths, and are aligned in the direction of the origin to ensure low energy leakage. The barrel and endcap crystals have a front face of $\sim 22 \times 22$ mm^2 and $\sim 29 \times 29$ mm^2 respectively. This corresponds to the Molière radius, and provides sufficient granularity [16]. Energy resolution varies with energy, but a resolution of $\Delta E/E < 1\%$ is seen for $E \gtrsim$100 GeV [9, 16]. A preshower device consisting of two lead and silicon strip layers is placed in front of the crystals in the endcap region, improving the position determination of particles. The preshower is only required in the endcap regions as the small angular separation of the two photons from π_0 decays in the forward region may lead to the faking of a high energy isolated photon from a Higgs decay. The preshower thus allows rejection of the large $\pi_0 \to \gamma\gamma$ background that would otherwise compromise the $H \to \gamma\gamma$ signal.

HCAL

The HCAL is required to measure the energy deposited by strongly interacting particles. It must provide good energy containment and hermiticity for measurements of missing transverse energy, and is required to minimise the non-Gaussian tails in the energy resolution. The HCAL therefore maximises the material inside the magnet coil, in terms of interaction length [9].

Plastic scintillator tiles of thickness 3.7 mm are sandwiched between brass absorber layers of thickness ∼5 cm, with wavelength shifting fibres collecting and channeling the light to hybrid photodiodes [9]. A further layer of hadronic calorimetry is located just beyond the magnet coil, and increases the effective thickness of the HCAL to over 10 interaction lengths. This helps the HCAL to reach its performance goals, and to protect the muon system from contamination. HCAL endcaps provide coverage up to $|\eta| < 3$. The Hadron Forward (HF) calorimeter is situated beyond the muon system endcaps and extends coverage up to $|\eta| < 5$. It is composed of steel absorbers and quartz fibres. The jet transverse energy (E_{T}) resolution varies with the region of HCAL and with energy, but for energies above 100 GeV, resolutions of $\Delta E_{\mathrm{T}}/E_{\mathrm{T}} \sim 0.1$ are seen.

1.3.5 Muon system

Unlike electrons, photons and hadrons, muons are able to propagate through the ECAL, HCAL and magnet with minimal interaction. Muons therefore provide a strong indication of an interesting event over the background, so are prime candidates for triggering. Furthermore, dimuon events are signatures of important Higgs decay modes such as $H \to ZZ \to 4l$ and $H \to WW \to ll\nu\bar{\nu}$. It is therefore important for CMS to be able to identify muons and accurately measure their trajectories [9].

Three types of gaseous ionisation detectors are used in the muon system, and are interspersed throughout the iron return yoke in the barrel and endcaps. Drift Tube chambers (DTs) are used in the barrel region and Cathode Strip Chambers (CSCs) in the endcaps, with Resistive Plate Chambers (RPCs) used in both the barrel and endcaps. The RPCs provide a fast response and good time resolution, but coarser spatial resolution than the DTs and CSCs. The DTs and CSCs operate independently from the RPCs, and together the detectors provide complementary information that is used for triggering and reconstruction [9].

The momentum resolution of high p_{T} muons is determined by the position resolution of the muon detectors, but the resolution for lower p_{T} muons (<200 GeV/c) is affected by multiple scattering before the muon stations. Measurements from the Tracker do however provide good resolution at lower momentum, and the best overall resolution is achieved when information from the muon detectors and the Tracker is combined [9].

1.4 Silicon Strip Tracker control and readout

The control and readout systems of the SST are illustrated is Figure 1.7. Control of the SST modules is based upon the Front-End Controller (FEC) interface board, and involves the distribution of the 40 MHz LHC clock and first-level trigger signals to the front-end electronics, as well as the monitoring of the operating conditions and the configuration of modules prior to data taking.

Readout of the data from SST modules is based upon the APV25 readout chip [17], analogue optical links [18], and the Front-End Driver (FED) processing board [19]. Each sensor module requires an Analogue Optohybrid (AOH) to convert electrical signals into optical signals, using a Linear Laser Driver (LLD). Optical signals are then transmitted at 40 MHz along ∼65 m fibres to the off-detector electronics.

1.4.1 Control

The control of the SST is provided by the Front-End Controller boards. Each FEC distributes slow control commands to the front-end modules via the I^{2}C protocol [20]. Each FEC also receives the 40 MHz clock Level-1 trigger signals from the Trigger, Timing and Control (TTC) system, and encodes and distributes to the front-end modules. The TTC receives information from the Trigger Control System (TCS), which provides the clock and trigger signals and maintains synchronisation between

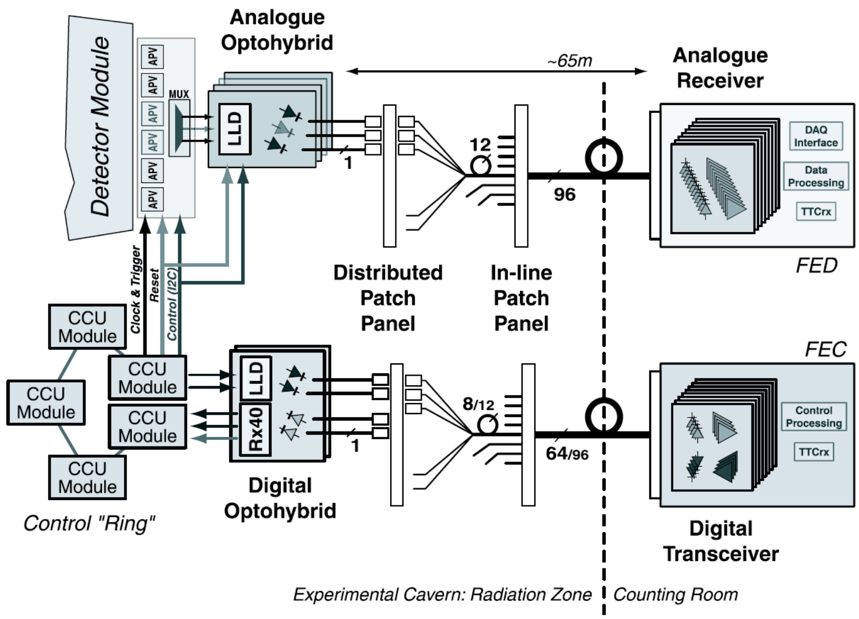

Figure 1.7: Control (bottom) and readout (top) systems of the CMS Tracker [18].

readout and data acquisition systems. The Trigger Throttle System monitors all buffers in the SST and sends a signal to the TCS to throttle the trigger rate in order to avoid buffer overflows where necessary.

Signals are distributed from the FEC via optical links. Optical signals are converted via Digital Optohybrids to electrical signals, and a ring control network is used to communicate signals to the detector front-end modules. Token control rings have a series of Communication and Control Units (CCUs) that communicate directly with several detector modules via a Phase Locked Loop (PLL), which provides a phase adjustable clock signal to the local electronics in order to maintain synchronisation between modules [12, 21].

1.4.2 APV25 readout chip

Readout of all silicon strips within the SST is provided by the APV25 Application Specific Integrated Circuit (ASIC). The APV25 is a 128 channel analogue pipeline readout chip, and a total of ∼76000 are needed to read out the full SST. The chip is fabricated with 250 nm CMOS technology, which provides high circuit density and high radiation tolerance, with low noise and low power [17]. Power consumption has been measured at ∼2.7 mW/channel [22] and noise of 270 + 38/pF or 430 + 61/pF electrons (depending on operational mode) [23].

Each channel contains a preamplifier, CR-RC pulse shaper, and a 192 cell analogue pipeline. Upon sampling and amplifying signals at 40 MHz, the pulse shaper provides a CR-RC waveform, with a peaking time of ∼50 ns. The peaking time is longer than the bunch crossing time of 25 ns, and was limited by the speed at which the CMOS circuits could provide efficient pulse shaping [24]. The analogue pipeline stores the amplifier outputs while external trigger decisions are made. The pipeline depth allows a programable latency of up to 4 μs, corresponding to 160 cells. The remaining 32 cells of the pipeline are reserved for storing any data awaiting readout.

Upon a trigger, each channel of the pipeline is read out by an Analogue Pulse Shape Processor (APSP), which is composed of a charge amplifier and a switched capacitor network, and is DC coupled to the pipeline read bus [17]. The APSP can be operated in one of two modes: *peak* or *deconvolution*. In peak mode, only the sample corresponding to the peak of the CR-RC pulse shape is read. In deconvolution mode, the three consecutive samples are read out from the pipeline and processed with a deconvolution filter. This results in an appropriately weighted sum of the measured signal amplitudes that produces an effective one-sample reading from a signal with a time constant of 25 ns; thus confining the pulse to a single bunch crossing period [24]. Deconvolution mode has the advantage of reducing pileup at high luminosities due to the shorter pulse. It does however require three pipeline samples, meaning that the 32 cells of the pipeline reserved for buffering can only store data for up to ten triggers. Figure 1.8 shows the resulting pulse shapes from peak and deconvolution modes.

Following pulse shaping, the data from pairs of APV25s are multiplexed into a single output frame at 40 MHz. The signal output has a dynamic range equivalent to approximately 8 MIPs. The output frame consists of a 12-bit header and 256 analogue samples from the two APV25s, and is therefore ∼7 μs in length. The pedestal value of the analogue output samples is adjustable to allow positive signal excursions, as well as negative excursions due to noise fluctuations or common mode

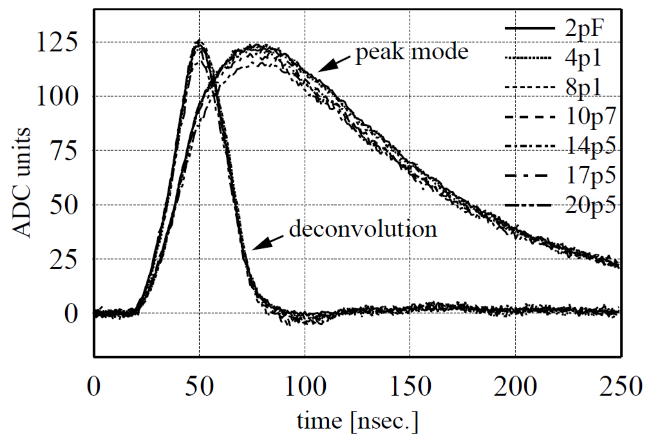

Figure 1.8: APV25 pulse shapes produced in peak and deconvolution modes (for various input capacitances) [25].

effects. The 12-bit header comprises a 3-bit start signal, an 8-bit pipeline address, and an error bit. Additionally a tick mark is also included every 1.75 μs if no data are present, in order to maintain synchronisation with the data acquisition system [17]. Figure 1.9 shows a typical data frame, before and after the reordering of analogue data into channel order by the Front-End Driver (FED) (Section 1.4.3). The 12-bit header and tick mark are shown, along with a typical 1 MIP signal.

1.4.3 Front-End Driver

Upon receipt of a Level-1 trigger, the data from multiplexed pairs of APV25s are transmitted via analogue optical links to a Front-End Driver [19]. The FED is a Field Programmable Gate Array (FPGA) based card, required to receive optical signals from the APV25 chips, and to digitise and process the raw data for analysis. 440 FEDs are required by the SST, and each receives the multiplexed optical signals from up to 192 APV25s.

Optical signals are converted to electrical signals and digitised at 40 MHz with 10-bit analogue to digital converters [19]. FEDs then buffer and process the digitised data. Processing of data is performed by 8 front-end FPGAs, with each one merging the data from 24 APV25s. The FPGAs check the synchronisation of the APV25s according to the tick marks in the data frames. Provided that the APV25s

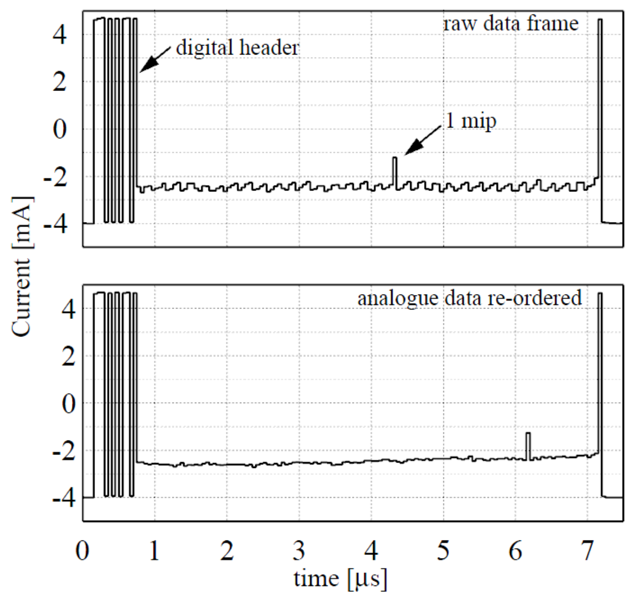

Figure 1.9: Example APV25 output data frame [25]. The upper plot shows the raw data (after multiplexing), and the lower plot shows the same frame with the analogue data in channel order.

are synchronised, data can be processed in one of three ways. In virgin raw mode, data remain unchanged: 10-bit digitised with no reordering. This mode is used for testing, commissioning and calibration. In processed raw mode, data are 10-bit digitised, reordered into channel order and pedestals are subtracted. In zero suppressed mode, data are 8-bit digitised, reordered and pedestal and common mode noise are subtracted. Clustering also happens at this stage, where only clusters of strips that pass a certain configurable threshold are accepted. Zero suppression reduces the data rate by more than an order of magnitude, and is the normal operating mode for the FED [14, 19].

The pipeline address and an error bit from the APV25 are recorded by the front-end Field Programmable Gate Arrays (FPGAs). The data will be forwarded with an error if, for example, a header is not detected or the channels are not synchronised, or if an error bit is already present in the APV25 data frame. The TTS provides input to the FED on how to proceed if synchronisation is lost.

Processed data are read out by a single back-end FPGA, which merges data from each of the front-end FPGAs. The back-end FPGA combines the processed data with information from the first-level trigger, and data are buffered while awaiting readout to the data acquisition system by the Front-end Readout Links (FRLs) [14, 19].

1.5 Trigger

At the nominal LHC design luminosity of 10^{34} cm^{-2}s^{-1}, an event size of 1-2 MB is expected per bunch crossing [9]. At 40 MHz this corresponds to an extremely large data rate of several tens of TB of data every second. The maximum event rate that can be written to permanent storage is of the order 100 Hz, so a trigger system with a rejection factor of $\sim 10^6$ is required. The trigger achieves this rejection in two steps; first the Level-1 Trigger (L1T) is designed to reduce the initial 40 MHz event rate down to 100 kHz, and then the High-Level Trigger (HLT) provides the further rejection down to the 100 Hz level.

1.5.1 Level-1 Trigger

The L1T [26] provides a fast online decision on whether to keep an event, with trigger algorithms provided by a custom hardware platform based on FPGAs and ASICs. Decisions must be made within the L1T latency of ~ 4 μs, during which time event details are stored on each subdetector in pipeline memory. The decision logic is made off-detector and the transmission time of nearly 2 μs must be included in the latency period, meaning a decision time of <2 μs is required [27]. Algorithms use raw data from the calorimeters and muon system, but not the Tracker, to make decisions based upon coarsely reconstructed data.

A schematic overview of the L1T is shown in Figure 1.10. The calorimeter trigger uses information from trigger towers, which consist of coarse regions in η-ϕ. Tower energy sums are formed for the ECAL, HCAL and HF, and are accompanied by information on transverse extent in the ECAL and the presence of MIP signals in the HCAL. The Global Calorimeter Trigger (GCT) searches for electron/photon candidates and jet candidates, and provides missing and transverse energy sums [27]. The muon trigger creates searches for useful events based on correlations between

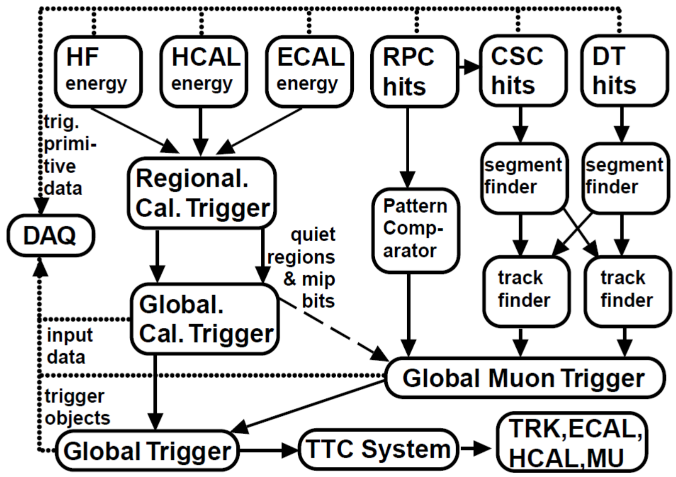

Figure 1.10: Schematic overview of the CMS Level-1 Trigger, including the global calorimeter and muon triggers, and global trigger [26].

muon sub-detectors and muon p_{T}. The Global Trigger (GT) synchronises trigger information from the calorimeter and muon triggers and generates a Level-1 Accept (L1A) signal if selected events pass certain pre-determined cuts. The L1A signal for any selected event is then forwarded to the TTC via the TTS. The TTC then forwards the signal to all sub-detector front-end electronics for the event to be read from the pipeline memory.

1.5.2 High-Level Trigger

The HLT is designed to reduce the trigger rate from the L1T down to the 100 Hz level at which events are written to permanent storage. The HLT consists of a farm of computer processors that perform finer reconstruction and data matching than that provided by the L1T, under a less stringent time constraint ($\sim$40 ms) [28].

Reconstruction and selection is arranged in algorithms of increasing complexity and CPU consumption, so that events can be rejected as soon as possible in order to reduce computing time. Initially just the information from the calorimeter and muon triggers is used, as with the L1T. Following this, algorithms make use of the full detector information, including that of the Tracker [29]. The remaining events of interest are then saved to mass storage for full offline analysis.

1.6 High-Luminosity LHC

In order to continue to improve the accuracy of Standard Model parameters and those of new physics, make further discoveries in high mass regions, and increase sensitivity to rare processes, further increases in luminosity are needed beyond the design luminosity of the LHC [30]. The High-Luminosity LHC (HL-LHC) is the proposed upgrade to the LHC, which will see major accelerator hardware modifications made, and the luminosity increased towards 5×10^{34} cm^{-2}s^{-1} with 300 fb^{-1} of integrated luminosity available per year. A phased approach is planned for the luminosity upgrade. Phase 1 began in March 2010, and will extend to beyond 2020. Phase 2 will follow, and will see a decade of running at the full HL-LHC luminosity. Upgrades to the machine will be made in three long shutdown periods [31].

2013-2014 sees Long Shutdown 1 (LS1), in which repairs, replacements and consolidations will be performed on the accelerator magnets and their interconnections. LS1 will allow the magnets to operate to their full design potential, and for the design centre of mass energy of 14 TeV to be reached by the end of 2014. Nominal design luminosity, L_{nom}, of 10^{34} cm^{-2}s^{-1} should be reached in 2015, allowing an integrated luminosity rate of $\sim$40 fb^{-1} per year [32]. Long Shutdown 2 (LS2) is scheduled for 2018, and will see upgrades to cryogenics and the LHC injector systems, with LINAC2 being replaced with LINAC4 [32, 33]. LS2 will allow luminosity to increase beyond L_{nom}, and it is hoped that it will reach $2L_{\text{nom}}$ by 2020 [32].

Beyond 2020, the statistical gain in running without considerable improvements in luminosity will become marginal, and to maintain strong progress the LHC will have to achieve a further significant increase in luminosity. Long Shutdown 3 (LS3) is planned to begin around 2022, during which time the final HL-LHC preparations will be made. Technical details have not been finalised, but will include further significant upgrades to LHC magnets, cryogenics and collimation systems, as well as upgrades to the pre-accelerators. Equation 1.2 shows that there are a number of approaches available in optimising the beam parameters for higher luminosity. The quadratic dependence of luminosity on number of protons per bunch, N, makes this a particularly useful beam parameter to vary. However, beam current varies linearly with N, and the number of bunches, n, and there are several factors that limit current, such as such as RF power, collimation and cryogenics [32]. One solution to the current limit would be to halve n to give an increased bunch crossing time of 50 ns, allowing N to be increased to exploit the quadratic dependence, while maintaining sufficiently low beam current. This increased bunch crossing time may also be required if heavy electron cloud effects are shown to limit performance at 25 ns [32]. The corresponding increased peak event rate would however come at the cost of increased pileup in detector systems.

The emittance, ϵ, has already been shown to be better than expected at the LHC, though maintaining this with an increased N will be a challenge. A reduction in β^* would involve the use of stronger and wider aperture triplet quadrupole magnets. Such modifications would be local to interaction points rather than across the whole machine and injector chain, and may impinge upon detectors and impact their performance [34]. A further downside of a small β^* is that the wider separation between the two beams imposes a larger crossing angle, which has the effect of reducing the reduction factor, F. It has been suggested that this could be avoided by either allowing the two beams to operate with a smaller separation, or by limiting the long range beam-beam effects by compensation with the electric field of a conducting wire [35].

Regardless of the exact set of beam parameters chosen, the luminosity upgrade will have significant implications for all detectors, due to increased pileup, occupancies, data and trigger rates, radiation damage and geometric requirements. If current detector performance is to be maintained, significant upgrades will be required. Section 1.7 describes the proposed upgrades to the CMS detector for operation at the HL-LHC.

1.7 Upgrades to CMS

The proposed luminosity upgrade for the HL-LHC will have a significant impact on the CMS detector, with several hundred interactions per bunch crossing [36].

The higher particle flux will lead to greater channel occupancies, trigger rates and radiation damage, and replacements and modifications will therefore be needed for all sub-detector systems. As luminosity is gradually increased, upgrades to CMS will also follow a phased approach.

1.7.1 Phase 1

The muon system will gain an outer ring in the fourth layer of endcap muon chambers ($|\eta| < 1.8$), including both CSCs and RPCs. This will give a much more robust muon trigger, and allow trigger rates and p_{T} thresholds to remain sufficiently low without compromising efficiency. An extra iron yoke layer will be added behind this new layer, which will provide shielding from neutron spray caused by upstream beam losses. Electronics for the inner endcap layers will be replaced, and Micropattern Gas Detectors (MPGDs) are being considered for the forward regions, which can provide precision tracking and fast trigger information, and can be designed with the fine segmentation required at high luminosities [31, 37].

Upgrades to the hadron calorimetry will be seen in LS2, with the aim of handling the higher luminosity with increased robustness and efficiency, and with improvements to the trigger capability [31]. The barrel and endcap hadron calorimeters will see Hybrid Photodiodes (HPDs) replaced with Silicon Photomultipliers (SiPMs). These have better quantum efficiency, higher gain and better immunity to magnetic fields. They also operate at lower bias voltages, meaning that they do not produce large pulses following voltage breakdown that may mimic energetic showers [38]. SiPMs also allow depth segmentation in the HCAL layers, which will reduce pileup at high luminosity operation, and improve clustering and geometric discrimination. Modifications will also be made to the front-end electronics, and to the back-end electronics to provide enhanced information to the RCT [31]. In the forward hadron calorimeters, photomultipliers will be replaced with improved ones that have higher quantum efficiency and four-way segmented anodes for greater rejection [31].

LS2 will also see the full replacement of the pixel detector with an identical system, supplemented with a fourth barrel layer and a third pair of endcap disks [31, 39].

This will allow the present tracking performance to be maintained, even in the higher occupancy environment later in Phase 1 [31]. The material budget will be reduced with the introduction of a CO_2 cooling system, ultra-lightweight mechanical support structures and the displacement of electronics out of the tracking volume. The pixel Readout Chip (ROC) will be modified to handle increased data rates at higher luminosity, and high bandwidth electronics and links will also be introduced, which will allow the reuse of existing fibres and cables [31].

Upgrades to the Level-1 Trigger are expected during Phase 1, which will be required to deliver the L1A signal within the same time period of a few μs. The overall trigger rate of 100 kHz is to be maintained, with DAQ readout bandwidth increasing in order to accommodate the greater data volume [31]. It is foreseen that the trigger system will move to a micro Telecommunications Architecture (μTCA) [40], to replace the current VME system, allowing greater maintainability and flexibility. Upgrades include rebuilding of the RCT to take advantage of the available granularity, and rebuilding of the CSC and RPC track finders to include the additional fourth layer of endcap muon detectors. A new TTC based on more advanced technology will also be implemented [31].

1.7.2 Phase 2

By 2020 it is anticipated that the LHC will be running with a luminosity of 2×10^{34} cm^{-2}s^{-1}, and CMS will have collected around 300 fb^{-1} of integrated luminosity. Further significant upgrades to CMS will be required during LS3 in preparation for Phase 2, where an anticipated integrated luminosity of 300 fb^{-1} will be seen each year.

In the muon system, the DT detector is expected to be able to cope with higher luminosity, but upgrades to its electronics are foreseen. The RPC and CSC detectors will also require modification to handle the greater particle fluxes, though the systems will remain largely unchanged [36]. Both hadron and electromagnetic calorimetry will require further modifications to maintain robustness in the high luminosity environment as a result of radiation damage, material activation and detector lifetimes, as well as software consequences for the trigger and event and pattern recognition [31]. It is foreseen that the Phase 2 upgrades will focus particularly on the barrel and endcap ECAL regions, and the forward regions of the HCAL [31].

Whereas most sub-detector systems will not need significant modification for the HL-LHC, the Tracker will have to undergo complete replacement due to radiation damage, and significant modifications must be made to meet requirements in the high luminosity environment. The Tracker must have a higher radiation tolerance, being able to handle radiation doses from an integrated luminosity of $\sim$3000 fb^{-1}. The higher particle flux will also mean a requirement for increased sensor granularity to keep occupancies sufficiently low. Simulations of heavy ion events, where track density is similar to that expected at the HL-LHC, in the present Tracker show encouraging results, indicating that efficient tracking is still possible with higher occupancies [41]. Advanced ASIC technology will be required to handle the high rates, particularly in the pixel layers, and to limit the power consumption with the required higher granularity. Sensors should be thinner and more radiation tolerant to avoid increased leakage current and excessive noise and power consumption levels.

Increased power consumption is anticipated in the Tracker as a result of the required increase in granularity. Plans to reuse existing cables will introduce large constraints, with deliverable current is limited by cable cross-sections. A DC-DC conversion power scheme has therefore been adopted, in which higher voltages are locally translated to lower voltage levels required by on-detector electronics [42], leading to a requirement for on-chip voltage conversion (Section 4.2.5) [43]. More efficient cooling methods, such as CO_2 cooling, will be required to remove the excess heat load, while also minimising material in the Tracker volume and being able to cope with the constraints of the existing pipes. High-speed data links will be required to handle the larger data rate generated by the increased granularity, and must also maintain compatibility with existing optical fibres [31].

Another key, and completely novel, requirement for the upgraded Tracker will be the ability to contribute to the Level-1 Trigger. The increase in luminosity will

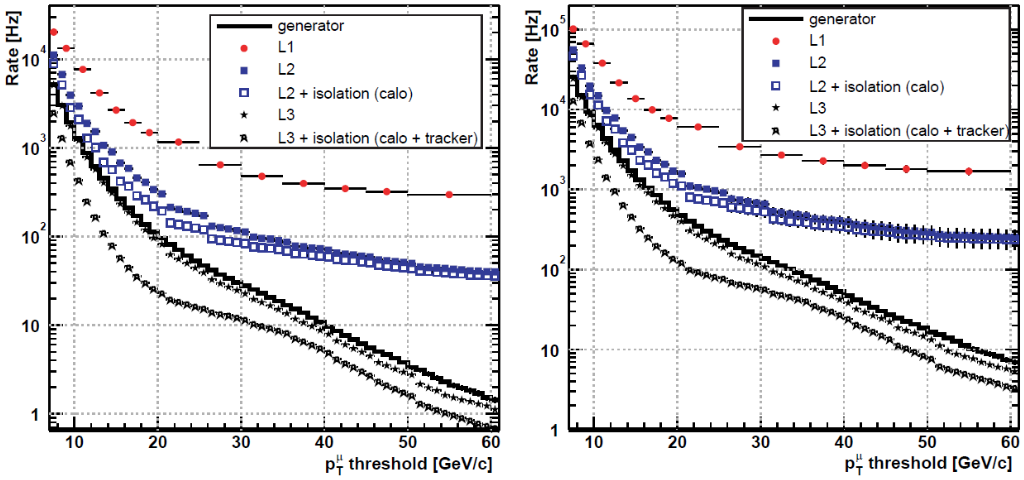

(a) (b)

Figure 1.11: Single muon rates vs threshold as a function of p_{T} for (a) low (2×10^{33} cm^{-2}s^{-1}) luminosity and (b) high (10^{34} cm^{-2}s^{-1}) luminosity [28].

mean an increase in trigger rate, if trigger thresholds are to remain the same. In the high luminosity environment, current trigger rates from the muon and calorimetry systems would vastly exceed the allowed 100 kHz rate, and cannot be reduced sufficiently by simply increasing p_{T} thresholds. Figure 1.11 shows the variation of single muon rates with p_{T} for various trigger levels. The inclusion of tracking information in Level-3 is shown to lead to increased elimination of fake candidates.

One major difficulty in implementing a tracking-trigger will be that much of the decision logic will have to be done on-detector, within the allowed latency period, and without cost to tracking performance. One proposal is to use modules that can provide on-chip p_{T} discrimination, by rejecting tracks that show large curvature in r-ϕ. This could be achieved by discriminating against wide clusters, or by correlating hits in two closely spaced sensors [31]. This concept has received much effort, and has involved the development of the CMS Binary Chip (CBC) [43]. The CBC is a prototype readout chip that uses binary, unsparsified architecture, for use with silicon strips in the upgraded CMS Tracker. Further prototypes will be capable of including on-chip logic that can contribute to the Level-1 Trigger. The CBC design is described in Chapter 4, along with early results. Plans for further iterations and modules for tracker-triggering will also be discussed.

1.8 Beam tests in the H8 beamline

The SPS North Area is an experimental site that sits just north of the SPS ring (see Figure 1.1). It was originally designed to house long-lasting experiments, but now provides a facility for short term beam tests that typically last a matter of weeks.

Beam particles are extracted from the SPS, and transported to the North Area, where beam splitters divide the primary beam into three parts, which are directed towards three primary targets: T2, T4 and T6. Each primary target scatters and attenuates the primary beam and generates secondary hadronic particles. Configurable dipole magnets are used to direct particles into a secondary beam, with characteristics according to the requirements of the user. Other secondary particles are dumped onto heavy absorbers. The North Area has seven secondary beams available, with beamlines housed in three separate experimental halls. Each beamline contains a number of longitudinally spaced experimental areas from which beam tests may take place. Beyond the experimental areas the beam is dumped onto heavy absorbers. Multiple tests can occur along a single beamline, with downstream tests operating parasitically off those upstream.

The H8 beamline is situated in the North Area, downstream of the T4 target. It can be used to extract a secondary beam with the T4 target in place, or the primary beam with the target removed. The beam has a spill structure, in which protons are extracted at a roughly constant rate for around 10 s, before a gap of around 35 s. Subsequent chapters present the results of beam tests conducted in the H8 beamline.

Chapter 2

Tracking telescope for crystal channeling measurements

A charged particle telescope has been constructed for the study of the crystal channeling of protons. Crystal channeling is one method that has been suggested for improved collimation at the LHC. This chapter starts with an overview of collimation at the LHC and the phenomenon of crystal channeling. The design of the telescope is then described, and beam test results from its use in the 400 GeV H8 proton beamline are presented.

2.1 Introduction

The UA9 collaboration [44] aims to demonstrate that the technique of crystal channeling could be used to improve collimation of proton and heavy ion beams at the LHC. For the purpose of studying the effect of crystal channeling of such particles, a tracking telescope is required. Tests are conducted in the 400 GeV proton beam in the external H8 beamline of the CERN SPS, in which a variety of silicon crystals are placed in the beam and rotated by a high precision goniometer into the correct channeling orientation. As the angular acceptance for crystal channeling is very low, around 10 μrad for 400 GeV protons, a telescope of good angular resolution of just a few μrad is required. This can be achieved through a combination of long baseline and good sensor spatial resolution.

Such a telescope has been constructed, primarily to test future detector modules for the upgraded CMS Tracker, but which is also highly suitable for crystal channeling studies. The telescope comprises five measurement planes, spaced along the beam-line, each of which gives a 2-dimensional position measurement normal to the beam, thus allowing a 3-dimensional trajectory to be measured [45].

Exploiting the time structure of the H8 beam involves taking several thousand events during a spill lasting around 10 s. During a crystal scan, the goniometer will typically rotate in the gap between spills, which lasts for around 35 s. As a goniometer step is typically just a couple of μrad, it is important to acquire as many data as possible during a spill in order to maintain a rapid scan rate without losing statistical precision. The CMS Tracker electronic readout chain is clearly well suited to fast readout, and the telescope is based heavily on this.

2.2 Beam collimation at the LHC

At 7 TeV each, the two beams at the LHC will store a total energy of around 350 MJ, with a transverse energy density approaching 1 GJ mm^{-2}; this makes the beams potentially highly destructive. Meanwhile at 7 TeV, the superconducting magnets would quench upon an energy deposition in the coils of around 30 mJ cm^{-3} [46]. Beam losses inevitably occur via a number of processes, in which protons are continuously lost from the nominal beam position, into the "primary beam halo". There are broadly two categories of beam loss: *normal* and *abnormal*. Normal beam losses include beam dynamics processes such as diffusion, scattering and beam instabilities, but also operational variations such as orbit, tune and chromaticity changes during ramp, squeeze or collision. Abnormal losses are due to failure or irregular behaviour of accelerator systems.

A collimation system is needed to minimise the effects of these beam losses and provide the following functionality [47]:

1. Cleaning of the beam halo to avoid quenching of the superconducting magnets.

2. Minimise the effect of halo-induced background in physics experiments.

3. Passive protection of machine aperture against abnormal beam loss, involving the generation of a beam dump trigger upon unusully high beam loss rates.

4. Scraping of beam tails for beam shaping and halo diagnostics.

5. Cleaning of the abort gap in order to avoid spurious quenches after normal beam dumps.

Furthermore, collimators must be robust in normal and abnormal operating conditions, and should not limit the luminosity through high impedance, which characterises the electromagnetic power exchange between the beam and its surroundings [48], or low cleaning efficiency, which characterises the fraction of beam particles that fall within a certain region of emittance phase space [47, 49].

The basic concept behind collimation at the LHC is a multi-stage system in which primary collimators first intercept the beam at around 6σ (where σ is the RMS of the beam profile). This causes scattering of halo particles, thus forming a secondary halo. Longer secondary collimators downstream then intercept the secondary halo at around 7σ, absorbing much of it, but also generating a tertiary halo. Depending on the position around the LHC ring, further collimators and absorbers at around 10σ protect the superconducting magnets and other machine components [50].

Due to the difficulties of providing a fully functioning and robust collimation system suitable for the nominal luminosity, it was decided to take a phased approach to collimation, whereby the system would evolve with the performance of the LHC [47]. A trade-off between collimator impedance and robustness was found to exist, whereby robust materials such as graphite tended to give high impedance, and a material that gave sufficiently low impedance such as copper would be heavily damaged [51]. The final choice for Phase 1 collimation was however a robust graphite based system. The luminosity was foreseen to be limited to 40% of its nominal value by the impedance and the cleaning inefficiency of the system [52]. Figure 2.1 shows a schematic layout of the Phase 1 collimation system.

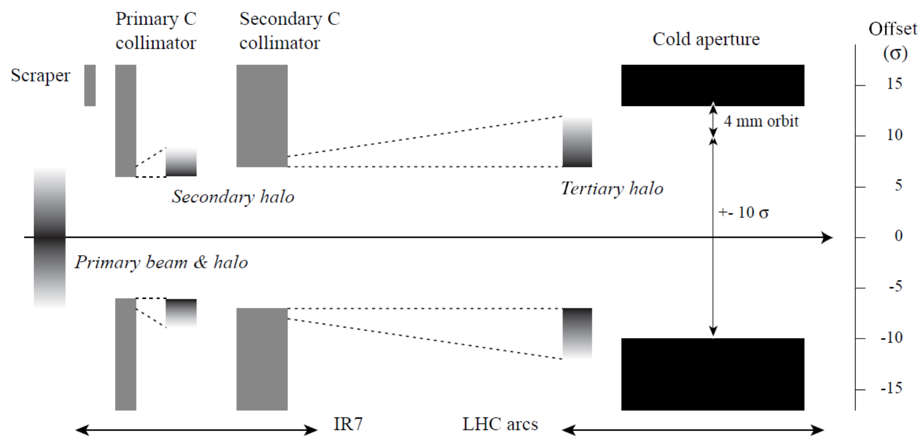

Figure 2.1: LHC collimation system (at injection energies). The graphite collimator jaws shown here are located at Interaction Region 7, upstream of the arc magnets. The collimators scatter partciles to give a more diffuse halo at each stage [47].

2.2.1 Motivation for collimation upgrade

The Phase 1 collimation system has proven to work very well up until LS1 [53]. However with impedance and cleaning efficiency limiting the luminosity, and the inevitable damage to collimator jaws, significant upgrades to the collimation system will be required. The strategy beyond LS1 will depend on the operational experience with energy close to 7 TeV, however upgrades anticipated for LS2 will see the collimation system require improved materials for increased robustness and improved impedance without compromising cleaning efficiency, integrated Beam Position Monitors, and the introduction of remote handling for high radiation environments.

With further advances in LHC performance it is foreseen that more significant upgrade strategies will be required for LS3, including further improved materials, and a complete redesign of collimation systems in the detector regions. The introduction of new, advanced collimation techniques is also a possibility. A key requirement at the HL-LHC is that the corresponding increased deposition of high energy particles in machine components does not pose a limit to the luminosity. Crystal channeling is one innovative technique that uses a bent silicon crystal to act as a primary collimator by deflecting halo particles coherently at a precise angle onto secondary absorbers, thus reducing scatter and radiation load on critical machine components.

Low impedance will also be an key requirement at the HL-LHC, and optimal crystals are also shorter than conventional primary collimators, meaning a smaller contribution to overall impedance [53, 54].

2.3 Crystal channeling

In conventional collimator systems, charged particles pass through amorphous materials, where they undergo many uncorrelated scattering interactions, emerging from the material at random, uncorrelated angles. If however a particle passes through a crystal structure and its trajectory is aligned with axes or planes of symmetry, coherent interactions can occur, in which protons emerge at predictable angles and can in principle be deviated from the beam in a controlled way.

When a particle's trajectory is aligned with a crystal plane, its interactions with atoms can instead be described by an interaction with the averaged electric potential of the crystal planes. The periodicity of the lattice structure creates a series of potential wells, and crystal channeling occurs when a charged particle becomes confined to such a potential well. If the crystal is mechanically bent, a sufficiently confined particle will follow the same curvature of the planes and emerge from the crystal at an angle that is equal to the bend angle. Crystal channeling as a means of steering charged particles was first proposed in 1976 by Tsyganov [55]. More recently efforts have focussed on the study of crystal channeling and its associated effects as a possible means of improved collimation systems. In this section a theoretical overview of crystal channeling and associated effects is given.

2.3.1 Straight crystals

For a particle to become channeled between crystal planes, its trajectory must be approximately parallel to the planes. Here we derive an expression for the critical angle between a trajectory and the crystal planes, below which channeling can occur. For the simple case of a straight (unbent) crystal, we consider the transverse motion of a proton confined to the electric potential between two crystal planes. The strong interplanar electric fields ($\sim 10^9$ Vm^{-1}) and the high proton mass means that energy levels within the potential are sufficiently close that they can be can be considered continuous, thus allowing a classical treatment [56].

We start by considering the relativistic Hamiltonian E, for a charged particle moving approximately in the z direction in a potential $U(x)$,

$$E = \sqrt{p^2c^2 + m^2c^4} + U(x). \tag{2.1}$$

By writing $p^2 = p_x^2 + p_z^2$, we can rewrite this as

$$E = \sqrt{p_z^2c^2 + m^2c^4}\sqrt{1 + \frac{p_x^2c^2}{p_zc^2 + m^2c^4}} + U(x). \tag{2.2}$$

As $U(x)$ is a function only of x, we can separate equation 2.2 above into transverse and longitudinal energies, both of which are separately conserved. By assuming that $p_z \sim p$ and expanding the second square root as a binomial with $p_x \ll p$, we obtain the following relation for the transverse energy,

$$E_x = \frac{p_x^2c^2}{2\sqrt{p^2c^2 + m^2c^4}} + U(x). \tag{2.3}$$

Substituting back in $E^2 = p^2c^2 + m^2c^4$ and using the relativistic relation $pc^2 = vE$, we can rewrite equation 2.3 as

$$E_x = \frac{vp}{2}\theta^2 + U(x), \tag{2.4}$$

where θ is the angle between the particle trajectory and the z-axis in the x-z plane, assumed to be p_x/p for small angles. For a particle to be confined to an interplanar potential, the transverse energy must be less than the height of the potential, U_0 (Figure 2.2). This leads to the following criterion for channeling,

$$\frac{vp}{2}\theta^2 + U(x) < U_0. \tag{2.5}$$

We can now set $U(0) = 0$, where $x = 0$ is the centre (minimum) of the potential. Assuming that for high energy $vp \sim E$, and rearranging for θ, we get the following expression for the critical angle, θ_C,

$$\theta_\mathrm{C} = \sqrt{\frac{2U_0}{E}}. \tag{2.6}$$

This is also known as the Lindhardt angle [57], and represents the maximum angle for which a particle of energy E will remain confined to a potential of height U_0. Intuitively, the critical angle decreases with particle energy and increases with height of the potential. For a silicon crystal with U_0 of ∼20 eV, and a 7 TeV proton beam, the critical angle is ∼2.4 μrad [50].

2.3.2 Bent crystals

For a crystal to capture and steer a particle in a certain direction it is necessary for the crystal to have a curved channel, and it is possible to achieve this by mechanical bending of the crystal. Channeling in bent crystals is similar in principle to that in straight crystals, however the curvature affects the periodic potential and analysis requires different treatment. For a proton to follow the curvature of the crystal planes, a centripetal force $-pv/R$ is required, where R is the bend radius of the crystal. It is now useful to define a new coordinate system such that the longitudinal coordinate, z, follows the curvature of the crystal. In this non-inertial reference frame a centrifugal force exists that is equal and opposite to the centripetal force required in the inertial frame. Equation 2.4 now becomes

$$E_x = \frac{vp}{2}\theta^2 + U_\mathrm{eff}(x) \tag{2.7}$$

where U_eff is the *effective planar potential*, and is the sum of the planar potential and the centrifugal potential,

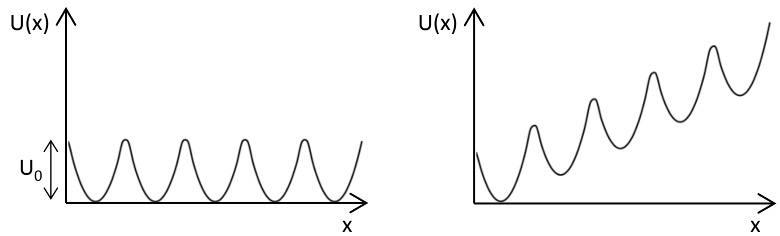

Figure 2.2: Left: periodic potential due to crystal planes for a straight crystal. Right: Effective periodic potential for a bent crystal (centre of crystal curvature is to the right of the figure).

$$U_{\text{eff}}(x) = U(x) + \frac{pv}{R}x. \tag{2.8}$$

The effect of the centrifugal term is an increase in potential with smaller radii, as seen in Figure 2.2.

2.3.3 Further crystal effects

The effective potential that forms in a bent crystal gives rise to a number of effects other than channeling. Figure 2.3 illustrates the various interactions by showing how the deflection angle varies with the incident angle of the particle on the crystal.

Firstly it is seen in regions 1 and 6 that the crystal is not sufficiently aligned for coherent interactions to occur, and so the crystal simply acts as an amorphous target, scattering particles in all directions with an average deflection angle of zero.

Crystal channeling occurs in region 2, where for a narrow channeling acceptance region of $\sim$0.05 mrad some particles are channeled by the crystal, and are deflected by the bend angle of approximately -0.16 mrad.

Volume reflection is seen in region 4. This corresponds to a small deflection (in this case $\sim$0.01 mrad) in the *opposite* direction from the channeling peak, and is due to a reflection of the particle from a crystal plane. This can be explained by looking again at the non-inertial reference frame and the effective potential in the bent crystal (Figure 2.2). As a particle has transverse motion in the positive x direction, it approaches crystal planes with progressively smaller radii. As a consequence it loses

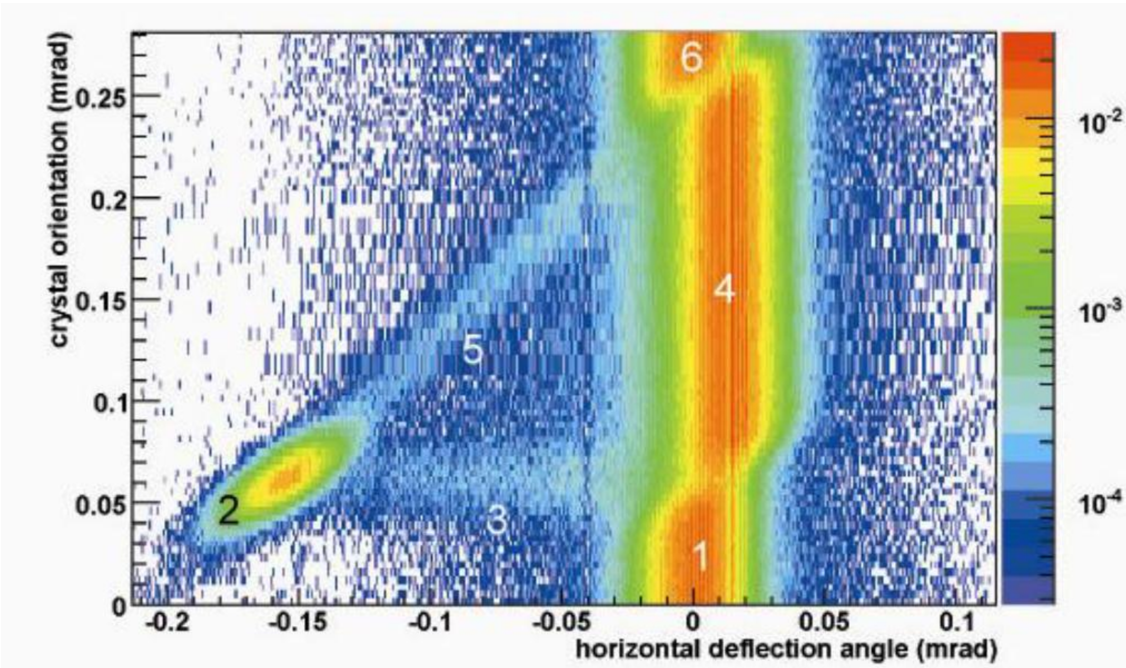

Figure 2.3: Plot of horizontal deflection as a function of impact angle on crystal orientation relative to incident trajectory. The crystal effects of channeling (2), volume reflection (4), dechanneling (3) and volume capture (5) are seen. Regions (1) and (6) show amorphous scatter. The data come from the H8RD22 collaboration [58].

transverse kinetic energy until it can no longer cross into the next interplanar region, and is thus reflected. Its longitudinal component of motion is again unchanged and the particle therefore undergoes a small deflection away from the curvature of the crystal planes. This can alternatively be thought of in the inertial reference frame, in which particles that approach crystal planes with progressively smaller radii will also approach planes at increasingly tangential angles. When the angle is sufficiently tangential it will no longer have the required transverse energy to pass the potential barrier and will be reflected.

Channeling and volume reflection are the two effects that could in principle be used to steer a charged particle in a certain direction, and can both be explained as elastic processes that conserve the total transverse energy. However, interactions may occur that change a particle's total energy or direction, and when transverse energy is no longer conserved this can give rise to inelastic effects which are also seen in Figure 2.3.

Dechanneling is one such inelastic effect, and is seen in region 3. This occurs when a particle, initially in channeling mode, undergoes a positive change in transverse energy during collisions with electrons [59]. With sufficiently large increase in transverse energy the particle will leave the channeling mode. This is seen in region 3, where a particle enters the channeling mode within the narrow channeling acceptance region, but becomes dechanneled at some point in the crystal. This causes it to leave with a deflection angle somewhere between zero and the crystal bend angle, depending on the position at which dechanneling occurs. It can be shown that the number of particles in channeling mode decreases exponentially with crystal length [56].

Volume capture is another such inelastic effect, and is seen in region 5. This occurs when a particle undergoes a negative change in transverse energy during collisions, which can cause it to become trapped in a potential well and become channeled. Region 5 shows that a particle with incident angle beyond the channeling acceptance region can become channeled for the remainder of the journey through the crystal. The particle will therefore leave the crystal with a deflection angle somewhere between zero and the crystal bend angle, depending on the position at which volume capture occurs. Figure 2.4 shows these four main crystal effects schematically.

2.3.4 Crystal material

An essential property for a crystal used for channeling is a high crystallographic quality, to ensure good channeling efficiency. Additionally, a high Z material has the advantage of increasing the potential height and thus the allowable bend angle, according to equation 2.8. Radiation tolerance and thermal conductivity of crystals are important for prolonged use in a high energy beam [60].

Through decades of development in the semiconductor industry, silicon has been shown to be a suitable material for reasons of cost, availability and production, and for its well understood performance for prolonged periods in a high radiation environment [61]. Studies have also been made with germanium [60, 62], which has a higher Z than silicon, and tungsten, which has a high Z and benefits from its robustness, but cannot be made with great lattice quality [60]. Diamond has

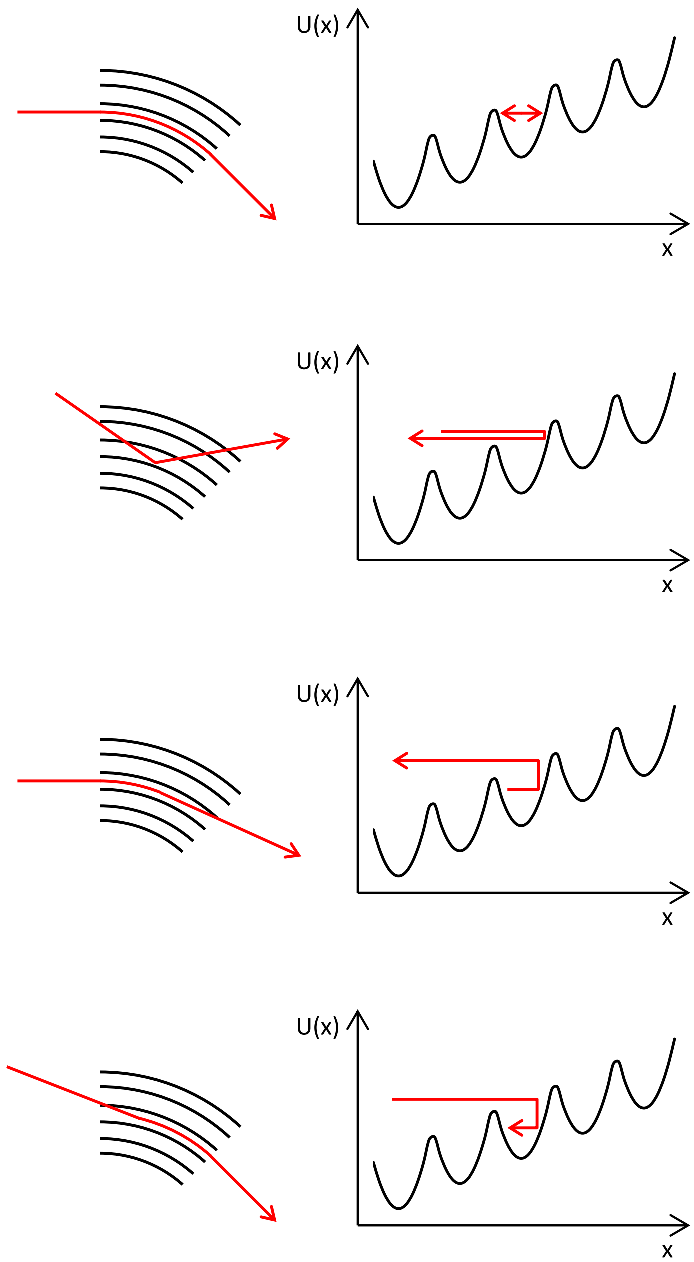

Figure 2.4: The four main coherent crystal effects that give rise to particle deflections, shown in terms of crystal geometry (left) and and effective potential (right). From top to bottom: channeling, volume reflection, dechanneling and volume capture.

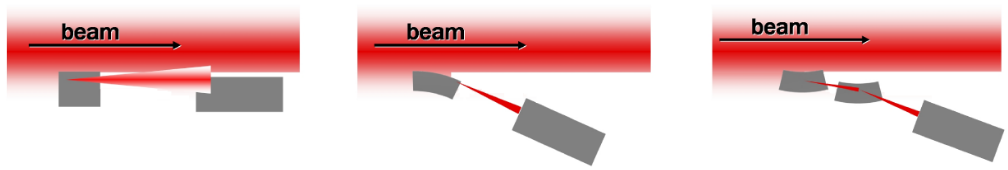

Figure 2.5: Left: Conventional primary collimation. Centre: Crystal channeling based primary collimation. Right: Volume reflection based primary collimation [50].

also been considered for channeling, and has the advantageous properties of a high robustness and high thermal conductivity. Its small Z does however mean that it could only be used where the critical angle is not a severe limiting factor [60]. Simulation studies have also shown that carbon nanotubes could efficiently channel protons, although this would be highly challenging practically [63].

Despite efforts focussed on other materials, as a consequence of its appropriate and well understood properties, and the lack of well understood alternative materials, silicon in general remains the material of choice for crystal channeling experiments.

2.3.5 Channeling for collimation

The use of bent crystals to steer charged particles is one possible novel technique for use in LHC collimator upgrades. The idea is based on the substitution of bent crystals for primary collimators, with crystals steering the primary halo into a narrow angular region where it can be absorbed. Crystal channeling and volume reflection are the two crystal effects that could be used to steer particles, as shown schematically in Figure 2.5.

When considering the practicality of bent crystals for this purpose, a number of factors must be considered.

- Efficiency: this can be defined simply for a particular process (eg channeling) as the probability for a halo particle to be deflected by the crystal as a result of that process. Clearly for any collimator based on channeling or volume reflection, the efficiency must be as high as possible to maximise beam cleaning performance.

- Angular acceptance: this represents the angular range over which particles incident on crystal planes can be deflected by a particular process. In order to maximise efficiency a crystal must be aligned precisely with the beam. A small angular acceptance can mean that a non-zero beam divergence can reduce efficiency. The angular acceptance can thus be included as a component of efficiency when the beam divergence is considered. It can be seen on Figure 2.3 that volume reflection generally has a much larger angular acceptance (equal to the crystal bend angle) than crystal channeling. This is beneficial as it requires less stringent alignment, and gives more stability to beam variations.

- Deflection angle: this is the angle through which beam particles are deflected by a particular process. Clearly a higher deflection angle is preferable as it allows secondary collimators or absorbers to have a higher impact parameter, or equivalently for a given impact parameter it allows a more longitudinally compact system. In the case of channeling, a large bending angle would increase the deflection angle, and could be achieved through either a longer crystal or a smaller bending radius. However, a longer crystal can reduce efficiency through increased probability of dechanneling, and a smaller bend radius can reduce efficiency through increased dechanneling and also through a reduced angular acceptance. The deflection angle from crystal channeling is generally much greater than that from volume reflection, as seen in Figure 2.3.

The use of crystal channeling in hadron colliders has been considered beneficial since the design stages of the new generation of synchrotron accelerators evolving in the 1980s; not just for collimation purposes, but also for beam extraction to feed external beam lines [64]. A comprehensive list of references to the developmental work can be found in Refs. [56, 65].

Much of the early experimental work on crystal channeling was pioneered by the Russians. Following the theoretical proposal of Tsyganov in 1976, the deflection of protons was first demonstrated in 1979 by a Soviet-American team in the external beamline at JINR in Dubna, using 8.4 GeV protons [66]. Crystal assisted extraction from an accelerator was first demonstrated in 1984 at JINR at energies of 4-8 GeV [67], and later at IHEP in the 70 GeV U-70 proton beam [68, 69]. Crystals were routinely used at IHEP to extract particles from the U-70 beam for experiments, though channeling efficiency was just a fraction of a percent [70].

In 1990 the RD22 experiment was launched for the CERN SPS [71], and in 1992 the E853 experiment in the Tevatron at the FNAL [72]. In RD22, an extraction efficiency of 10% was routinely observed [73], and the multi-pass effect in which protons are channeled after multiple traversals of a crystal was demonstrated [74]. Channeling was also observed with fully stripped Pb-ion beams in the SPS [75]. In 1994, E853 reported proton channeling at the highest ever energy [76], and in 1998 the first ever observation of channeling of halo particles produced from interactions in colliding beams [77].

Crystals initially used for RD22 and E853 were high quality, dislocation-free silicon crystals, with a length of a few cm in the direction of the beam, and bent by a few hundred urad by a multi-point mechanical holder. Figure 2.6 shows a typical setup for RD22 using a crystal, 3 cm in length, bent along its full length by the holder. One downside of this multi-point bending was that the local increase in crystal bending caused a reduction in the channeling efficiency [64]. The introduction of U-shaped crystals provided a potential solution to the problem of the multi-point bending by removing the clamps from the face normal to the beam (Figure 2.6), however tests in RD22 showed no measurable improvements in the channeling efficiency [78]. It was later found that O-shaped crystals (Figure 2.6) could provide a more regular crystal curvature and, although not available for RD22 and E853, were used at RHIC and later at the T980 experiment [64, 79]. Further tests on optimisation of crystals focussed on the use of crystals that were shorter in the beam direction (down to a few mm), for the purpose of increased channeling efficiency [80, 81]. The use of strip crystals and quasi-mosaic crystals, which are described in Section 2.4, became the preferred choice due to a more even curvature of crystal planes, thus reducing the dechanneling probability [64]. Further crystal developments involved the use of chemical etching on the crystal surface to remove the amorphous layer, thus allowing channeling as soon as particles hit the crystal [82].

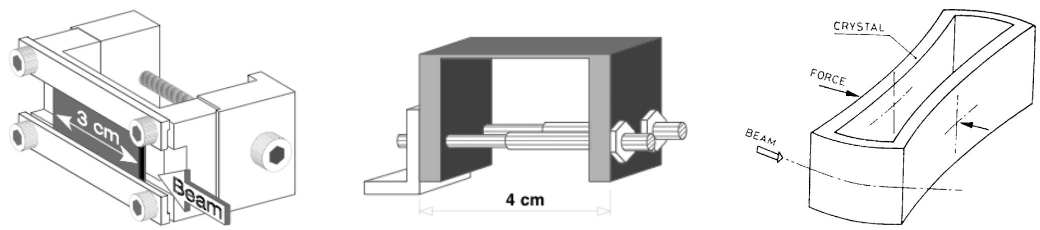

Figure 2.6: Left: Crystal bent with multi-point bending, as used in RD22. Middle: U-shaped crystal, as used in RD22. Right: O-shaped crystal, used in RHIC and T980 [64].

In 2006 the first observation of the volume reflection effect was reported in the 70 GeV proton beam at IHEP [83]. Meanwhile, efforts towards crystal channeling began in the H8 external beamline of the CERN SPS with the multinational H8-RD22 experiment [84]. Here, silicon strip sensors were used to measure the trajectories of single particles upstream and downstream of bent crystals. Using a 9 mm long crystal with bend angle of 150 μrad, efficiencies of around 50% for channeling and 97% for volume reflection were seen. The plot of deflection as a function of incident angle is shown in Figure 2.3 [58]. The positive efficiency results from volume reflection highlighted its potential for sophisticated beam manipulations. The use of short crystals with a bend angle of 50.5 μrad allowed the dechanneling length due to nuclear scatter to be measured at about 1.5 mm, as well as the observation of a maximum channeling efficiency of 83.4% [85]. Short crystals were also used to investigate the optimal curvature for volume reflection, and found it to be approximately 10 times greater than the critical curvature for channeling [86]. The effect of multiple volume reflection was investigated, whereby a series of five crystals aligned longitudinally along the beam impart a larger total deflection angle. A total deflection angle of 67 μrad was seen, with an efficiency of around 84% [87]. Also studied was the phenomenon of axial channeling, in which crystals are constrained not only to the bent crystal planes, but to an additional lattice plane [88]. For this to be possible, an additional rotational degree of freedom is required for the crystal so that both channeling planes can be simultaneously aligned to the beam.

Various efforts have been made to incorporate crystal channeling in to collimation systems. In 2005 O-shaped crystals were used at RHIC, where an angular scan was performed in attempt to reduce experimental background with the crystal in the optimal channeling orientation. Results however were not positive, with an increase in background seen compared with that of an conventional amorphous target, despite channeling efficiency routinely exceeding 30% [89]. Further attempts were subsequently abandoned. The apparatus used in RHIC was however reinstalled in the Tevatron, and the experimental background was reduced by a factor of two in the CDF detector, and a channeling efficiency of over 50% was seen, in agreement with simulations [90]. Simulation studies of crystal channeling collimation systems at the LHC have indicated a cleaning efficiency improvement of a factor of 10-15 over the conventional Phase 1 collimation system [59].

2.4 The UA9 experiment

The aim of the UA9 experiment is to test crystal assisted collimation as an alternative to conventional collimation of protons and lead ions at the LHC [44, 91]. The final goal is to demonstrate that a crystal based system has higher cleaning efficiency than a conventional system. UA9 was approved in September 2008 and has been operational from June 2009. In order to achieve its goals, UA9 must accurately track individual particles as they pass through bent crystals in order to identify the effects of channeling and volume reflection, and thus measure the cleaning efficiency. Experiments are carried out in the SPS, where particles pass a crystal multiple times; and also in the H8 external beamline of the SPS North Area, where particles only make a single pass through a crystal before being dumped onto downstream absorbers. This work focusses on the efforts in the H8 beamline.

2.4.1 General experimental procedure

A crystal channeling experiment can be divided into three broad areas; the manufacture and preparation of a suitable bent crystal, a high precision goniometer on which a crystal can be mounted and positioned, and a tracking system to measure particle trajectories upstream and downstream of the crystal. The convention of a left-handed coordinate system is chosen, with the positive z-axis describing the beam direction, and x and y the horizontal and vertical displacements respectively. The origin is chosen as the crystal position, and crystals are generally aligned such that the channeling deflection is in the horizontal plane, with angular scans thus being about the vertical axis.

Crystal bending

Silicon crystals are used to bend particle trajectories. Crystals are fabricated from high quality silicon wafers, with an extremely low miscut angle (angle between the lattice nominal direction and the crystal surface direction) [92]. The lattice planes used for channeling are generally curved about the y-axis, leading to the deflections of interest to be seen in the x-z plane. The bending of crystals involves a primary mechanical bending which imparts a secondary bend about an orthogonal axis. It is the secondary bend that is used in channeling experiments, and there are two ways of achieving this.

- Strip crystals: strips are fabricated from silicon wafers, and typically have a width of 2-3 mm and thickness <1 mm. They are positioned vertically with the wide face normal to the x direction. A primary mechanical bend about the z-axis imparts a secondary anticlastic bend about the y-axis. This effect is shown in Figure 2.7, along with a strip crystal mounted in a mechanical holder.

- Quasi-mosaic crystals: plates of silicon are fabricated from silicon wafers, with thickness typically a few mm. Plates are made and positioned such that the large face is normal to z and the (111) planes are normal to x. Due to the anisotropy of the elastic stress tensor, a primary mechanical bend of the crystal about the x-axis imparts a secondary bend of the (111) planes about the y-axis. This effect is shown in Figure 2.8, along with a quasi-mosaic crystal mounted in a mechanical holder.

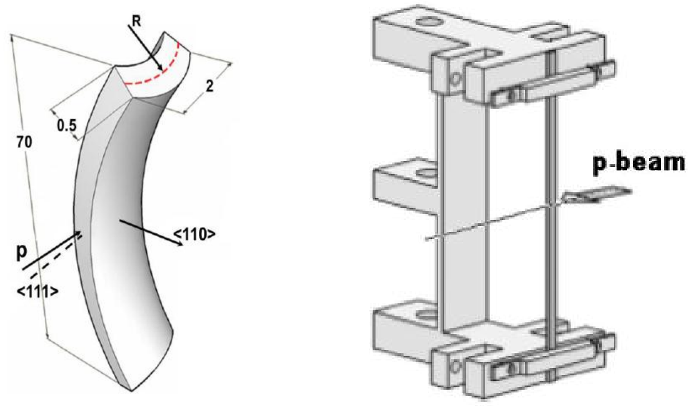

Figure 2.7: Left: A primary bend to a strip crystal gives rise to a secondary bend through the anticlastic effect [93]. Right: A holder imparts a primary bend to a strip crystal. Crystals used are typically a few mm in the beam direction [94].

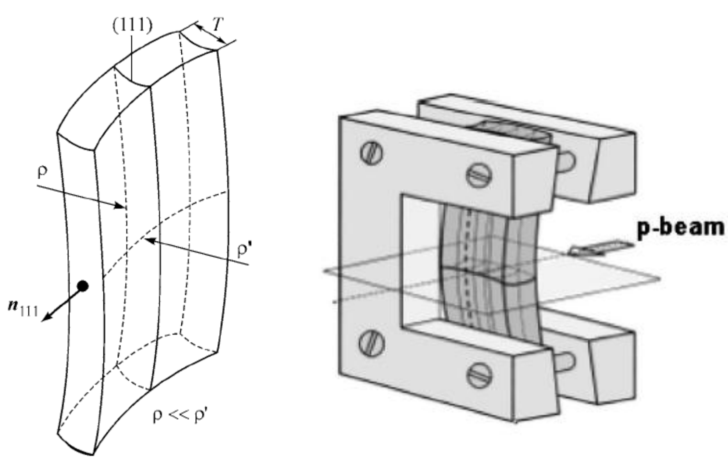

Figure 2.8: Left: A primary bend to a quasi-mosaic crystal gives rise to a secondary bend due to the anisotropy of the lattice [95]. Right: A holder imparts a primary bend to a crystal. Crystals used typically have a thickness in the beam direction in the range of 1-10 mm [94].

Goniometer

A goniometer is required to adjust and record its position. Various goniometers have been used, all of which have certain common features. Typically they have three degrees of freedom; a rotation about y for alignment of channeling planes with the beam, a rotation about x, and a translation in x for horizontal alignment of crystals with the beam (particularly important with strip crystals). The study of channeling phenomena requires a certain precision in the y rotation; with a beam divergence of several μrad and a critical angle for 400 GeV protons of around 10 μrad, the accuracy and precision of the alignment process must be of the order of μrad [92, 94].

Tracking

In order to track particles through the crystal, a high precision telescope has been designed and constructed by Imperial College, suitable for high rate data taking in the H8 beamline [45]. The telescope and its performance is the subject of the following sections.

2.5 Telescope hardware

Figure 2.9 shows the basic layout of the telescope. At the centre of the apparatus is the bent silicon crystal that is under test, mounted on a goniometer. The upstream arm of the telescope consists of two XY planes, each consisting of a pair of orthogonal silicon strip sensors, which together give an x-y measurement. The downstream arm comprises three measurement planes; two XY planes, and one UV plane. The UV plane is identical to the XY planes, but is rotated by 45° about the z-axis, which allows it to suppress ghost hits during multi-hit events. Finally a scintillator that provides the telescope with a trigger is shown just downstream of the last measurement plane.

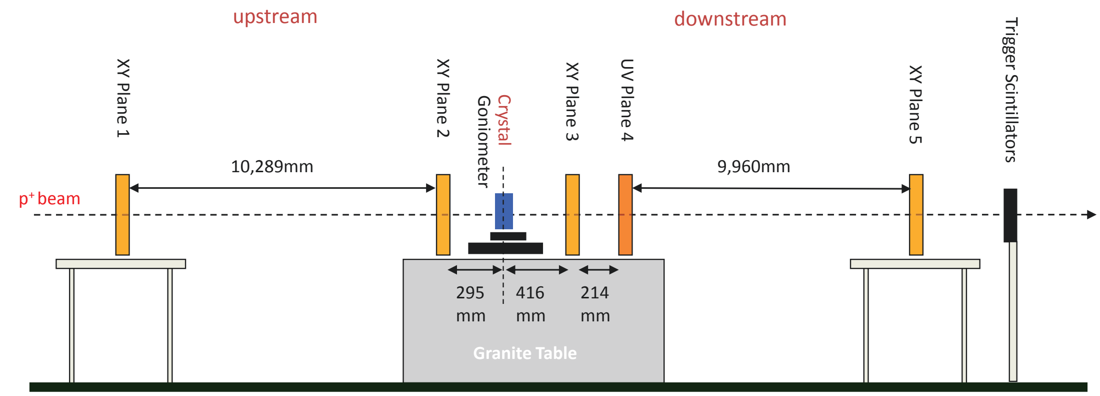

Figure 2.9: Layout of the tracking telescope, showing the five measurement planes, scintillator trigger and the crystal mounted in the goniometer.

2.5.1 Sensors

The sensors used in each XY plane were fabricated by Hamamatsu Photonics (HPK), originally procured for the D0 experiment at the Tevatron [45]. They are single sided silicon strip sensors on a high float-zone material. They are AC coupled, nominally 320 μm thick, and have 639 strips (98 mm long) with a readout pitch of 60 μm, including a floating intermediate strip. Typically total leakage current is 100-200 nA over a voltage range up to 500 V, and full depletion is at 100 V. Good uniformity over all sensors was seen, and assembled modules showed no dead strips or excessive noise [45].

2.5.2 Hybrids

Sensors are read out by APV25 chips, which are mounted on hybrids that were developed for use in the Inner Barrel of the CMS Tracker. The operational mode of each APV25 chip, as well as bias settings, are programmable via I^2C interface. For this application, chips were configured in peak mode, whereby a single sample per channel is retrieved from the pipeline following a trigger (see Section 1.4.2). This produces a data frame containing analogue samples from all 128 channels. The analogue memory is accessed by write and trigger pointers that have a programable latency between them. This latency is configured such that when a trigger is applied,

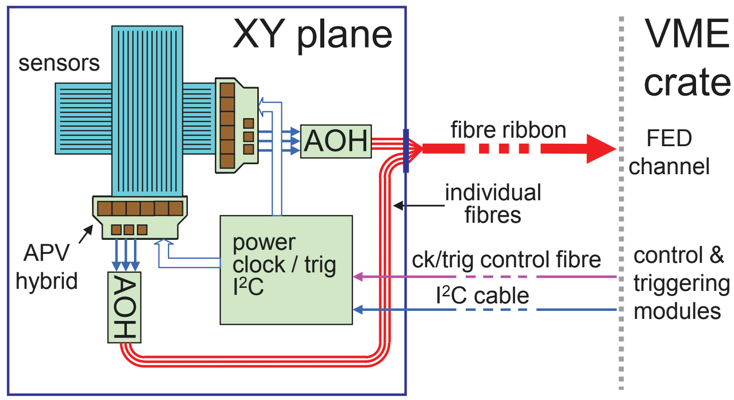

Figure 2.10: Schematic diagram of an XY plane [45].

the data sample retrieved is the one that was stored a latency period earlier. The latency period can account for all delays, such as signal propagation, particle time of flight and decision making. Each hybrid has six APV25 chips, five of which are used to read out the 639 strips (with one unbonded channel), and one chip remaining unused. Additionally there are three ancillary chips on each hybrid; a Detector Control Unit chip (DCU), a Phase-Locked Loop chip (PLL) and an APV25 Multiplexer chip (APVMUX). The DCU monitors the currents, voltages and temperatures on each hybrid. The PLL recovers the 40 MHz clock and trigger signals from a single sequence, in which a trigger is encoded as a missing clock pulse, and transmits these to the APV25 chips. The APVMUX multiplexes the outputs of two APV25 chips onto a single line, with each hybrid thus providing three output lines to transmit the data from the six APV25 chips corresponding to each sensor.

2.5.3 Optical Links

The use of optical transmission from telescope to FED avoids the mass associated with electrical cables, and has the advantage of immunity to electrical interference. For each front-end hybrid an AOH converts electrical signals from each multiplexed APV25 pair into optical signals, using a Fabry-Perot edge emitting semiconductor laser at 1310 nm wavelength. Each XY plane thus has six optical fibre connectors, which are combined into a single fibre ribbon suitable for long distance transfer of signals. Figure 2.10 shows a functional block diagram of an XY plane.

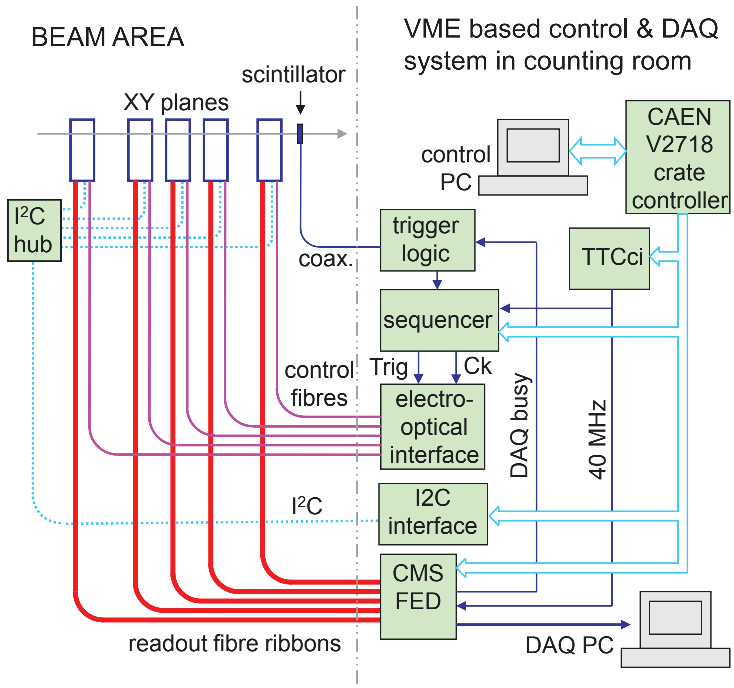

Figure 2.11: Schematic diagram of the telescope including readout and control systems [45].

2.5.4 Readout and control

Figure 2.11 shows a functional block diagram of the telescope, including the control, readout and DAQ systems. Shown on each XY plane is the analogue optical fibre output, the digital control fibre and the I^{2}C input for slow control and monitoring. The VME based control and DAQ system is housed in the counting room, where the operational state of the DAQ and front-end is controlled by a PC via a CAEN V2718 crate controller.

The trigger is provided by a scintillator-photomultiplier system. The trigger signal is transmitted to the trigger logic module in the VME crate, which then passes the signal onto the sequencer module, provided that the DAQ busy veto input is not active. Upon a trigger, the sequencer module waits for the programable delay before issuing a 25 ns trigger pulse to the electro-optical interface module. This delay, of 25 ns resolution, is adjusted in conjunction with the programmed latency in the APV25 chip, such that the trigger arriving at the front-end is timed to the pulse peak. The electro-optical interface module encodes the trigger signal as a missing pulse in the 40 MHz clock, which is then fanned out and converted to optical signals which are transmitted to the XY planes. Upon receipt of the trigger signal, the XY planes then generate a data frame which is transmitted optically to the FED, where signals are converted back to electrical, and digitised.

High speed readout is offered by the zero suppression operational mode on the FED, which involves pedestal and common mode subtraction as well as hit finding. For the purposes of commissioning and troubleshooting, the FED can provide raw data. If internal buffers are nearly full, the FED can send a DAQ busy signal to the trigger module to stop accepting triggers. This depends on the trigger data rate, data volume and the speed at which the DAQ PC can accept data.

The CMS-specific TTC module provides the master 40 MHz clock reference to the sequencer module and the DAQ system on the FED. This clock determines the sampling time in the APV25 chips. The beam arrival time is asynchronous which means that sampling at the peak of the amplifier pulse shape is not generally possible. However due to the reasonably long pulse shape, there will always be a sample sufficiently close to the peak.

A VME to I^2C interface module provides the slow control for the I^2C registers in the APV25, DCU, PLL, APVMUX and laser driver chips in the front-end hybrids, and AOH modules in each XY plane. The I^2C bus speed is limited to 10 kHz for reliability over long distances involved. An I^2C hub, which is located in the beam area, fans out the single I^2C bus to each XY plane, and an I^2C transaction selects the particular XY plane bus to be activated. Each of these I^2C buses is opto-isolated at the I^2C hub, and again at the XY planes [45].

2.5.5 XY plane construction

Each XY plane is housed in a $25 \times 25 \times 100$ cm^3 off-the-shelf diecast box. Internal components are arranged according to Figure 2.10. Each sensor and hybrid is mounted on an aluminium alloy plate, which is cooled by a Peltier element, and each Peltier element is cooled by a small fan. The Peltier current is adjusted to maintain a stable temperature of 20°C. Figure 2.12 shows two XY planes, with one

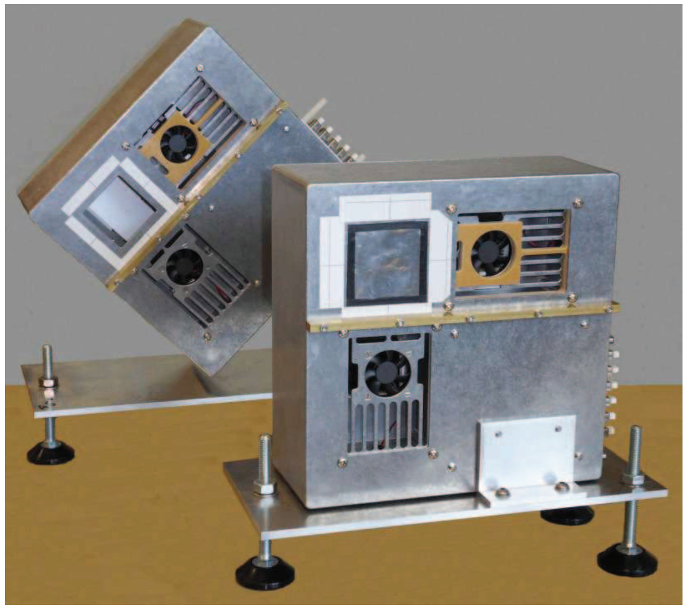

Figure 2.12: Photograph of two XY planes [45]. The plane in the background is rotated 45° to transform it into UV plane.

rotated 45° to transform it into a UV plane. The plane in the foreground shows a 30 μm aluminium foil window over the sensor overlap region, and there is a similar window on the reverse side of the box. The background plane is shown without the aluminium foil, and one of the sensor planes can be seen. The ventilation grills from the cooling fans can also been seen adjacent to the windows.

2.6 Data acquisition

A data acquisition (DAQ) system is required to do three things: receive data from the telescope front-end, format the data for storage, and provide online monitoring so that the quality of the data can be maintained. For the purpose of studying crystal channeling, angular scans are required in order to allow the correct orientation of the crystal to be found. For an automated scan procedure, the DAQ must interface with the goniometer for control and the recording of position data. The peak trigger rate is limited to 40 kHz within the sequencer in order to prevent buffer overflows in the front-end APV25 chips. There are several important factors that must be considered when designing such a high rate DAQ: event size, potential bandwidth bottlenecks, the structure and period of the particle spill, the memory and buffer sizes, and the computational power that is available, as well as the speed at which data can be written to disk. The existing CMS Tracker DAQ hardware is capable of providing such a DAQ system [26], and the telescope DAQ is heavily based on this.

2.6.1 Hardware architecture

The DAQ hardware is based on the CMS Tracker FED. The FED captures, digitises, processes and packages the analogue optical signals from the front-end APV25 chips, and ships out event fragments over VME or S-Link64. The telescope has only $\sim$0.1% of the channels of the CMS Tracker, and only a single FED is required to keep the same basic functionality. The S-Link64 interface is chosen to transfer data off the FED, due to superior readout rate over VME.

A DAQ PC receives the S-Link data from the FED via a FEDKit [96] PCI card, bypassing the requirement for the gigabit optical network fabric and associated modules used in CMS [23]. A large memory is reserved on the DAQ PC to allow buffering of data while it is directly accessed by the online software. To avoid overflows in the S-Link buffer, back pressure is automatically exerted on the FED until the FED buffers are occupied. If the FED buffers become occupied, the DAQ busy veto signal is asserted and any further trigger is blocked at the trigger logic module. This veto signal is applied until all buffer occupancies in the readout chain fall below a nominal threshold.

2.6.2 Software and run control

The software framework is based on the XDAQ distributed architecture [97]. Software is generally written in C++ Object Oriented Classes, however some supporting applications, such as the run control interface, are written in Java.

The DAQ online software configures and controls the run parameters, monitors requests to the FED and other applications, provides communication of trigger signals, and manages memory the storing of data to disk. Raw data can be unpacked, formatted and repacked, ready for analysis online or offline. Further details of the DAQ online software can be found in Ref. [45].

The DAQ user interface is provided by the standard implementation of the CMS XDAQ Run Control. Via a webpage interface, the user can select from a list the specific configuration needed for a particular run. Dynamic web pages provide important information for monitoring, such as the number of events collected, the data rate through the DAQ, and the total amount of data saved to disk. Other monitoring pages can display configurable histograms showing beam profiles and plots of showing for example efficiency and cluster widths, and prompt analysis can also include calculations of particle deflections due to scattering or channeling [45].

2.6.3 Data throughput

There are a number of factors that can limit the DAQ rate, such as the maximum APV25 trigger rate of 140 kHz, the FED output transmission rate of 640 $\mathrm{MB\,s^{-1}}$ (with S-Link64), and the FEDKit event rate of $\sim$500 $\mathrm{MB\,s^{-1}}$. Also limiting the rate is the number of DAQ PC cores available to perform event processing and analysis, and the rate at which events can be written to disk ($\sim$30 $\mathrm{MB\,s^{-1}}$) per disk controller and SM application. For the telescope, with a single FED, the bottlenecks come from the number of cores available for event processing, and the storage rate to disk. For an event size of 1 kB, the maximum rate to disk is around 30 kHz. EP cores run at 4-7 ms per event for each processor core. With a 10 s spill across a 45 s spill period, the use of eight processor cores allows an instantaneous trigger rate of $\sim$7 kHz.

2.6.4 Data storage and formatting

Only two of the four FED readout modes are used in the telescope operation; virgin raw and zero suppressed. Virgin raw, which outputs complete raw digitised analogue APV25 frames, is used in commissioning for pedestals and noise on each strip. Zero suppression, which compresses data by outputting only data for hits above a certain charge threshold, is used for general operation. Zero suppressed mode leads to a FED data output of no more than 50 B per event, which compares to 2.5 kB in virgin raw mode. However this data reduction is made somewhat more modest due to the inclusion of ~1 kB of header information to each event [45].

Data are processed and formatted within the XDAQ online framework [97]. Events are stored in in CMS data format and can thus be processed online and offline using the CMS Software environment (CMSSW) [9]. The CMSSW framework is flexible and modular, and standard strip tracker reconstruction packages are used in conjunction with reconstruction packages specifically written for use with the telescope. The system is sufficiently configurable that the entire offline reconstruction can be run online.

2.7 Reconstruction

Reconstruction of 3-dimensional particle trajectories throughout the telescope requires first the 2-dimensional reconstruction of hits on each telescope plane. Following this, tracks are fitted to the hits in the x-z and y-z planes separately.

2.7.1 Hit reconstruction

Hit reconstruction is a two stage process, involving online analysis by the FED, and offline analysis during the event reconstruction stage. During a zero suppression run, the FED first subtracts pedestals and common mode effects. The FED then selects only strips with $S_{\mathrm{S}}/N_{\mathrm{S}} > 2$, where S_{S} is the signal amplitude of the strip, and and N_{S} is the RMS noise on the associated channel. Adjacent strips are then grouped together into cluster candidates. If a strip is isolated however, a stricter criterion of $S_{\mathrm{S}}/N_{\mathrm{S}} > 5$ is required for it to be selected.

Cluster candidates are redefined offline during the event reconstruction. Candidates are chosen around seed strips with $S_{\mathrm{S}}/N_{\mathrm{S}} > 3$. Strips adjacent to a seed strip are included in the cluster if $S_{\rm S}/N_{\rm S} > 2$. Finally, the cluster candidate is accepted if $S_{\rm C}/N_{\rm C} > 5$ where $S_{\rm C}$ is the total cluster signal, $\Sigma S_{\rm S}$, and $N_{\rm C}$ is the RMS cluster noise, given by

$$N_{\rm C} = \sqrt{\sum \frac{N_{\rm S}^2}{n}} \tag{2.9}$$

where n is the number of strips in the cluster. The hit position is estimated by interpolating the charge deposited on strips. For each cluster candidate, the pair of adjacent strips that has the greatest signal is selected, and the variable η is defined as

$$\eta = \frac{S_{\rm R}}{S_{\rm L} + S_{\rm R}} \tag{2.10}$$

where $S_{\rm L}$ and $S_{\rm R}$ are the signals on the left and right strips of the selected pair respectively. The hit position relative to the left hand strip is then given by $p\eta$ where p is the readout pitch. For single strip clusters $\eta = 0$. A hit is defined as a cluster with width of four strips or fewer. This is done for both x and y sensors, to give a hit in the x-y plane.

So far hits are defined relative to the sensor in which they are seen. To ensure that hits on different sensors are defined relative to the global coordinate system, translational and rotational corrections must be made to hits on all sensors as part of the offline reconstruction. This alignment procedure is described in Section 2.8.2.

2.7.2 Position error correlations

The performance of a tracking telescope depends not only on the hardware and hit reconstruction used, but also on the specific details of the track reconstruction. Track reconstruction must make full use of the hit position information on each plane, and the optimal method will proceed in a way that depends on the specific track measurement required. The general approach used is that given in Ref. [98].

There are two contributions to uncertainty in track fitting: the position resolution of each sensor, and the uncertainty due to Multiple Coulomb Scattering (MCS) of charged particles traversing each plane.

The position resolution is a characteristic of the sensor hardware and hit reconstruction method used, and gives uncorrelated position errors on each telescope plane. MCS however clearly leads to correlated errors with each plane, as a deflection from one plane will affect hit positions on all subsequent planes. Molière's theory of MCS shows that a charged particle traversing a thin layer of detector material will undergo successive small-angle deflections, symmetrically distributed about the incident direction [99]. The Central Limit Theorem says that, for a large number of independent scattering events, the distribution of the overall scattering angle is approximately Gaussian. The expected overall scattering angle, $\langle\phi\rangle$, comes from the width of this Gaussian and is given by equation 2.11 [100].

$$\langle\phi\rangle = \frac{13.6\ \mathrm{MeV}}{p\beta c}\, z_{\mathrm{c}} \sqrt{\frac{s}{X_0}} \left[1 + 0.038\ \ln\left(\frac{s}{X_0}\right)\right] \tag{2.11}$$

where p, β, and z_{c} are the momentum, velocity and charge number of the incident particle, and s and X_0 are the thickness and radiation length of the scattering medium, respectively. Assuming that each telescope plane has 640 μm silicon and 60 μm aluminium contributing to scattering, for 400 GeV protons we obtain an expected scatter angle of 2.39 μrad. ϕ_x and ϕ_y correspond to the scatter in the x-z and y-z planes, and are independent, so the overall polar scattering angle, ϕ_{xy}, is given by

$$\phi_{xy}^2 = \phi_x^2 + \phi_y^2. \tag{2.12}$$

The correlated MCS errors propagate out away the region of the track that is to be parameterised. For example, if it were required to reconstruct the particle track in the region immediately upstream of the telescope, as incident on plane 1, it would be necessary to consider the MCS errors as increasing with each successive downstream

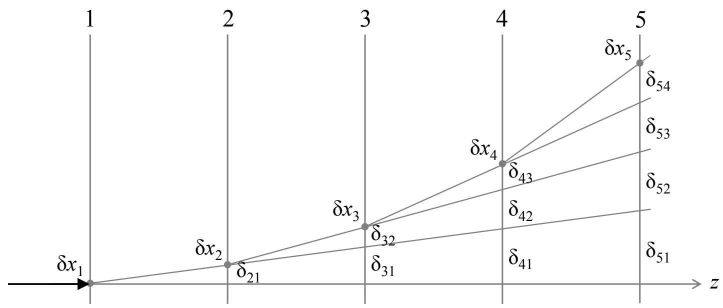

Figure 2.13: MCS error correlations for reconstructing a straight track as incident on plane 1. δ_{ij} is the scatter uncertainty on plane i from plane j. It is seen that uncertainties from scattering accumulate with each successive plane from the region of interest. All scatterings are shown as positive for simplicity.

plane, as illustrated in Figure 2.13. As an example, we consider the reconstruction of a track immediately upstream of the telescope, as incident on plane 1. Here it would be necessary to consider the MCS errors as increasing with each successive downstream plane, as illustrated in Figure 2.13.

From Figure 2.13 it is seen that $\delta_{j+1,j}$ is the expected scatter contribution from plane j to plane $j+1$. This is independent of any previous scatterings and, assuming small scatter angles, is given by

$$\delta_{j+1,j} = \langle\phi\rangle(z_{j+1} - z_j). \tag{2.13}$$

The scatter contribution to any plane i from plane j, where $i \geqslant j$, is then given by

$$\delta_{ij} = \delta_{j+1,j}\,\frac{z_i - z_j}{z_{j+1} - z_j}. \tag{2.14}$$

The total deviation due to scatter on plane i can then be expressed only in terms of the independent scatterings, $\delta_{j+1,j}$, and the plane geometry,

$$\delta x_i = \sum_{j=1}^{i-1} \delta_{j+1,j}\,\frac{z_i - z_j}{z_{j+1} - z_j}. \tag{2.15}$$

The covariance matrix describing position errors due to scatter, V_{ij}^{scat}, is defined as the expected product of the deviations on planes i and j,

$$V_{ij}^{\text{scat}} = \langle \delta x_i \delta x_j \rangle = \langle (\delta_{i1} + \delta_{i2} + \ldots \delta_{i,i-1})(\delta_{j1} + \delta_{j2} + \ldots \delta_{j,j-1}) \rangle \tag{2.16}$$

with $V_{ji}^{\text{scat}} = V_{ij}^{\text{scat}}$. Using equation 2.13 and the fact that the independent scatterings are uncorrelated (ie $\delta_{ij}\delta_{kl} = 0$ for $j \neq l$), equation 2.16 reduces to

$$V_{ij}^{\text{scat}} = \langle \phi \rangle^2 [(z_i - z_1)(z_j - z_1) + (z_i - z_2)(z_j - z_2) + \ldots (z_i - z_{i-1})(z_j - z_{i-1})]. \tag{2.17}$$

For a five plane telescope, V_{ij}^{scat} is a 5×5 matrix. The uncorrelated position errors must now be included in this matrix. The contribution from sensor resolution is the diagonal matrix given by

$$V_{ij}^{\text{res}} = \delta_{ij}^{\text{Kron}} \sigma_i \sigma_j \tag{2.18}$$

where $\delta_{ij}^{\text{Kron}}$ is the Kronecker delta function and σ_i is the spatial resolution of plane i. The overall covariance matrix, including both correlated multiple scatter and uncorrelated position errors is then given by

$$V_{ij} = V_{ij}^{\text{scat}} + V_{ij}^{\text{res}}. \tag{2.19}$$

The specific approach outlined is appropriate for reconstructing tracks incident on the first plane, however the approach can be generalised for the reconstruction of tracks in any region of the telescope, with each region corresponding to a different V_{ij}^{scat}. For example, if tracks incident on plane 4 were to be reconstructed, the MCS uncertainties would increase with distance from this region, as illustrated in Figure 2.14.

It can be seen from Figure 2.14 that the only correlation that exists is between planes 1 and 2, and that there is no scatter error on planes 3 and 4. This gives

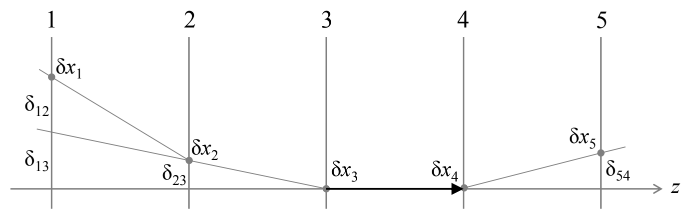

Figure 2.14: MCS error correlations for reconstructing a straight track incident on plane 4. All scatterings are shown as positive for simplicity.

a covariance matrix, V_{ij}^{scat}, that is zero everywhere except for an upper left 2×2 submatrix, and the lower right element. To this matrix, the uncorrelated position error matrix, V_{ij}^{res}, is now added as before.

2.7.3 Straight track reconstruction

The straight line tracks can be fitted in x and y independently. Considering just the fit in x, as before, we assume that the path has the following linear relationship

$$x = x_0 + \theta z \tag{2.20}$$

where x_0 is the intercept at $z = 0$ and θ is the gradient, $\frac{\mathrm{d}x}{\mathrm{d}z}$. We can use the coordinate data (z_i, x_i), along with the overall covariance matrix, V_{ij}, to express χ^2 in matrix form according to the following relation

$$\chi^2 = (X - HA)^{\mathrm{T}} V^{-1} (X - HA) \tag{2.21}$$

where

$$X = \begin{pmatrix} x_1 \\ x_2 \\ x_3 \\ x_4 \\ x_5 \end{pmatrix} \quad ; \quad H = \begin{pmatrix} 1 & z_1 \\ 1 & z_2 \\ 1 & z_3 \\ 1 & z_4 \\ 1 & z_5 \end{pmatrix} \quad ; \quad A = \begin{pmatrix} x_0 \\ \theta \end{pmatrix}. \tag{2.22}$$

To find the fit parameters, A, such that χ^2 is minimised, we impose the least squares condition,

$$\frac{\partial \chi^2}{\partial A} = 0. \tag{2.23}$$

This must be solved for A to give the fit parameters. Differentiating χ^2 with respect to A we obtain

$$\frac{\partial \chi^2}{\partial A} = -2H^{\mathrm{T}}V^{-1}(X - HA). \tag{2.24}$$

The non trivial solution to equation 2.23 is then

$$A = (H^{\mathrm{T}}V^{-1}H)^{-1}(H^{\mathrm{T}}V^{-1}X) \tag{2.25}$$

which provides the two fit parameters. The errors of the parameters are given by

$$E_{A_x} = \langle \delta A \delta A^T \rangle = (H^T V^{-1} H)^{-1} = \begin{pmatrix} \sigma^2_{x_0} & \mathrm{cov}(x_0, \theta) \\ \mathrm{cov}(x_0, \theta) & \sigma^2_{\theta} \end{pmatrix}. \tag{2.26}$$

The same procedure is followed for the fit in y, and it is assumed that there is no error in the z coordinates of each sensor. This approach gives the four fit parameters required for straight line tracks, along with their errors.

Sometimes it may be necessary to ignore a plane from the fit, if for example a plane has errors. This can be done by setting the resolution of the plane to a large value (ie set V^{res}_{ii} large to ignore plane i). This has the effect of giving the plane no weight in the fit, without losing the contribution of the plane to multiple scatter. Multiple planes can be ignored from the fit in this way.

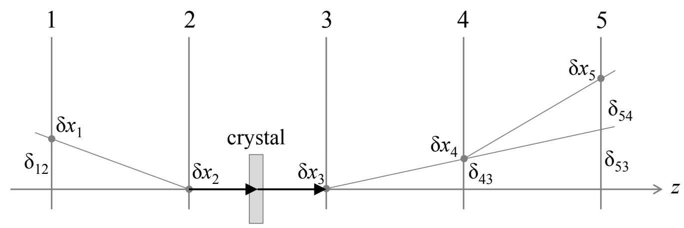

Figure 2.15: MCS error correlations for reconstructing a bent track in the presence of a crystal. All scatterings are shown as positive for simplicity.

2.7.4 Bent track reconstruction

Using the telescope for the purpose of measuring crystal channeling, where a bent crystal causes the proton path to bend, the straight line fit outlined previously is not appropriate. As the crystal is small compared to the telescope baseline, a proton path may be modelled as two straight tracks which meet at the crystal ($z = 0$). Reconstruction should therefore generate a path described by three parameters: an incident angle, an outgoing angle, and an impact parameter at the crystal (intercept at $z = 0$). As with the straight line fit, this fitting process can be done independently for x and y. The generation of the covariance matrix, V_{ij}, proceeds in a similar way to that of the straight track fit. Figure 2.15 shows the error correlations required.

Once again considering just the fit in x, we assume that the path is given by the following linear relationship,

$$x = \begin{cases} x_0 + \theta_1 z, & z < 0 \\ x_0 + \theta_2 z, & z > 0 \end{cases} \tag{2.27}$$

where the incident and outgoing paths have angles θ_1 and θ_2 respectively, and share a common intercept, x_0, at the crystal. χ^2 is again defined by equation 2.21, but for the three parameter fit H and A are given by

$$H = \begin{pmatrix} 1 & z_1 & 0 \\ 1 & z_2 & 0 \\ 1 & 0 & z_3 \\ 1 & 0 & z_4 \\ 1 & 0 & z_5 \end{pmatrix} \quad ; \quad A = \begin{pmatrix} x_0 \\ \theta_1 \\ \theta_2 \end{pmatrix}. \tag{2.28}$$

As with the straight track fit, the fit parameters, A, are given by equation 2.25, thus providing incident angle, outgoing angle, and impact parameter in the presence of a crystal. Equation 2.26 again provides the matrix of errors and covariances between the parameters,

$$E_{A_x} = (H^T V^{-1} H)^{-1} = \begin{pmatrix} \sigma^2_{x_0} & \mathrm{cov}(\sigma_{x_0}, \theta_1) & \mathrm{cov}(\sigma_{x_0}, \theta_2) \\ \mathrm{cov}(\theta_1, \sigma_{x_0}) & \sigma^2_{\theta_1} & \mathrm{cov}(\theta_1, \theta_2) \\ \mathrm{cov}(\theta_2, \sigma_{x_0}) & \mathrm{cov}(\theta_2, \theta_1) & \sigma^2_{\theta_2} \end{pmatrix}. \tag{2.29}$$

2.8 Telescope performance

The telescope has provided a tracking system for various UA9 beam tests, in the 400 GeV proton H8 beamline. Beam tests have been performed from September 2010 to October 2012. This section describes the performance of the telescope using data collected in the September 2010 and September 2011 runs.

2.8.1 Detector performance

As part of commissioning it was necessary to determine the pedestal values for each strip in every sensor. This was done during a dedicated pedestal run, in which the trigger logic module was used to provide fake triggers, and with the FED operating in virgin raw mode. Figure 2.16 shows a set of pedestals for one sensor, with the value at a strip determined using the mean of the signal distribution for that strip. Figure 2.16 also shows a typical noise distribution for one particular APV25 chip, where noise is defined as the RMS spread of the signal distribution for each strip, and shows a mean value of ∼1.9 ADC counts. The distribution varies between APV25 chips depending on the relative gain from the optical links and the chip itself, but

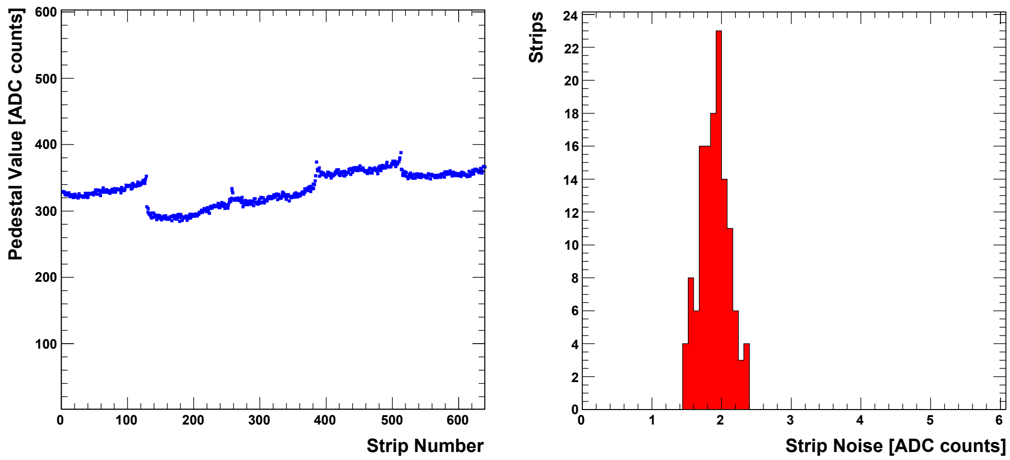

(a) (b)

Figure 2.16: (a) An example of pedestal values per strip for one particular sensor (plane 1, horizontal). (b) A typical noise distribution for all strips corresponding to a single APV25 in the same sensor.

Table 2.1: Signal to noise measurements for each sensor, averaged over all APV25s.

Plane	Sensor	S/N
1	x	26.2
1	y	26.3
2	x	35.0
2	y	36.0
3	x	34.6
3	y	34.5
4	x	34.9
4	y	35.4
5	x	32.1
5	y	32.4

the average strip noise over the telescope was measured to be ∼2.5 ADC counts. The mean S/N values for each of the ten sensors is shown in Table 2.1, where N is defined in equation 2.9. The average S/N value of ∼32 is consistent with that measured in CMS modules with similar strip lengths [2].

It is important that the APV25 pulse shape is sampled as close to the peak as possible. This is achieved by correctly timing the sequencer delay to correspond to the peak of the pulse in the APV25 pipeline. The programmable delay is implemented in the sequencer module, with 25 ns resolution. With an asynchronous beam, it is not possible to sample the pulse at the same position of the pulse each time. How-

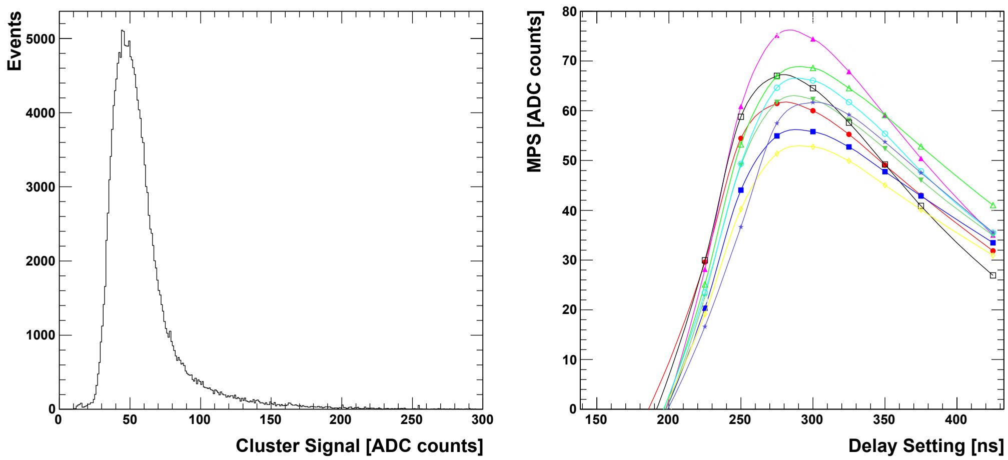

(a) (b)

Figure 2.17: (a) Cluster signal distribution for a single APV25, showing the characteristic Landau form. The distribution has a most probable signal (MPS) of 63 ADC counts. (b) MPS as a function of delay setting for all 10 sensors. The scan allows the APV25 pulse shape to be reconstructed.

ever, due to the flatness of the pulse near the peak, any sampling within 25 ns of the peak will be sufficiently close to leave a small error in the pulse height (up to a few %). Figure 2.17a shows the cluster signal distribution for a particular APV25 at a certain delay setting. By using a Landau fit to the data to estimate the most probable cluster signal, and repeating over a range of delay settings, it is possible to reconstruct the APV25 pulse shape. This is shown in Figure 2.17b for all sensors. The optimal delay was found to be 300 ns for the three central planes, with a further +25 ns and −25 ns added for the first and last planes respectively, to account for particle time-of-flight.

Figure 2.18 shows the cluster width distribution for all sensors. It might be expected that a single strip is the most likely size of a cluster, due to the sensors being normal to the beam. However, the presence of an intermediate floating strip enhances the effect of charge sharing between strips, and hence only ∼37% of clusters are one strip wide. This leads to an improvement in position resolution, as the cluster width can lend some information on the position of the hit (Section 2.8.3).

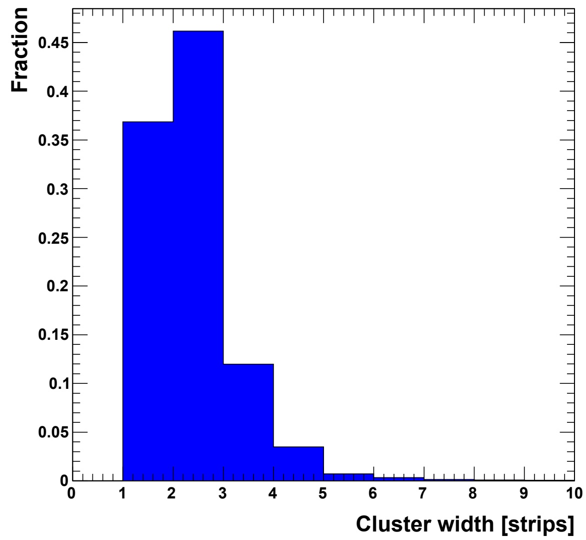

Figure 2.18: Cluster width distribution for all sensors combined.

2.8.2 Sensor alignment

In order to reconstruct particle trajectories using the telescope planes, it is necessary to ensure that planes are correctly aligned. A track based software alignment procedure is used to calculate any misalignments between sensors, from which hit positions can be corrected such that they are defined relative to the global coordinate system. After each intervention in the beam area it is necessary to perform a dedicated alignment run, in which a sample of $\sim 10^5$ tracks is collected. Alignment parameters are then extracted from the data offline. The alignment procedure involves taking the first and last telescope planes as a reference, and interpolating straight line tracks through the intermediate planes. An offset is applied to the last plane such that the average track angle is zero. Residuals in x and y are measured for each intermediate plane, and translational corrections to hit positions are applied iteratively until each residual distribution is centred on zero. Hits on plane 4 are first rotated by $-45°$ about z.

Rotational misalignments of sensors about z must also be considered, as any misalignment introduces a dependence of estimated hit position on the impact position along a strip. Figure 2.19 shows such a correlation between hit residual in x, and the impact position in y for a particular sensor. The rotational misalignment of the

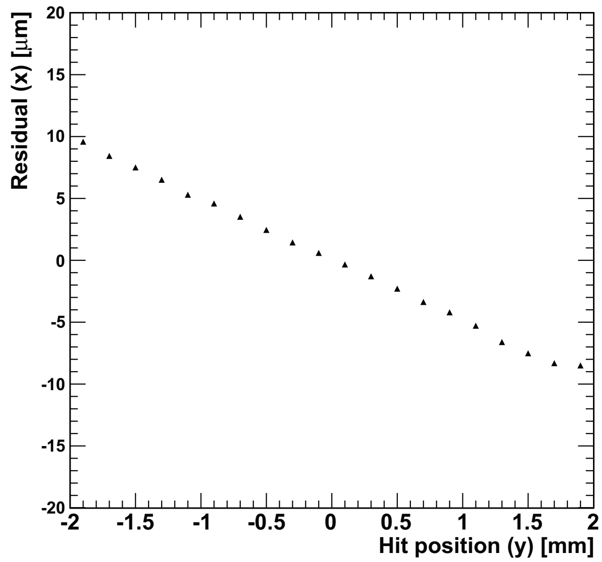

Figure 2.19: Mean hit residual in x for plane 3 as a function of estimated y position on the sensor. The gradient allows the rotational misalignment to be estimated at $\sim$9.8 mrad.

sensor can be estimated from the gradient of this distribution. Rotational corrections are applied iteratively to each sensor until such dependence is eliminated. The rotational misalignments of sensors was measured to vary between 0.1-8 mrad. Any rotational misalignment about x or y is considered negligible.

The z position of each plane is measured using a laser rangefinder, and the corresponding uncertainty is considered negligible in track reconstruction, due to the small angles that particle trajectories make to the nominal beam angle. The alignment procedure allows a precision of <1 μm for translational offsets and <0.1 mrad for rotational misalignments. The high rate DAQ means that a data set sufficient for alignments can be collected in just a few minutes.

2.8.3 Spatial resolution

The spatial resolution of each telescope plane is a key parameter in understanding both the impact parameter resolution and the angular resolution of a particle trajectory, and is measured by studying the distribution of residuals on each plane. Tracks are fitted on the plane in question using the straight track fit procedure (Section

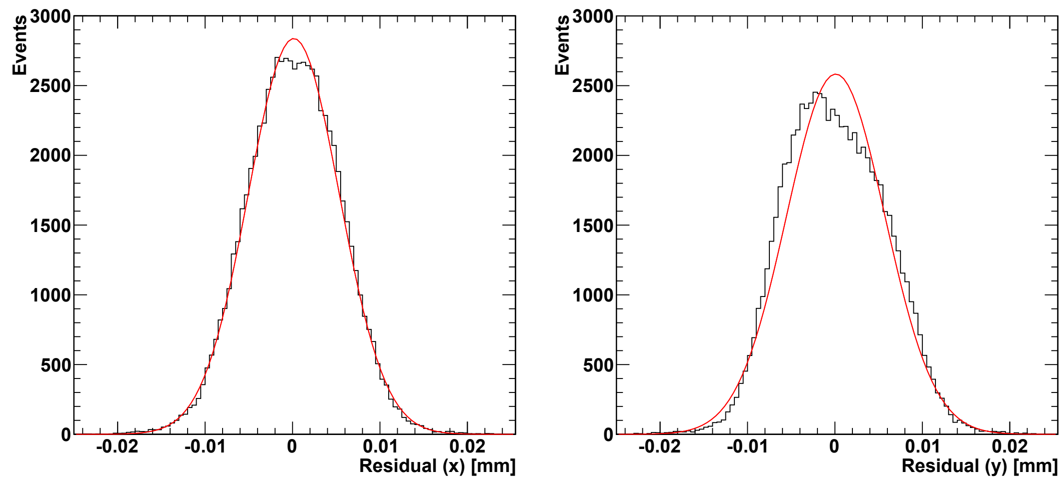

(a) (b)

Figure 2.20: Residual distributions for plane 3. (a) x sensor, (b) y sensor. The fitted hit position, f, comes from a fit to all five planes. A Gaussian fit is overlaid.

2.7.3), using data collected from an alignment run in which no crystal was present and straight tracks were expected. The residual, r, is defined as the difference between the measured hit position on a plane, d, and the fitted hit position at that plane, f,

$$r = d - f. \tag{2.30}$$

Figure 2.20 shows the residual distributions for plane 3 in both x and y. Both distributions are approximately Gaussian, with fitted widths of 5.21 μm and 5.63 μm respectively. The distribution in the y sensor shows slight asymmetry, most likely due to imperfect postion rotational alignment parameters on another plane. Using equation 2.30, the spread in the residuals is given by

$$\sigma_r^2 = \sigma_d^2 + \sigma_f^2 - 2\,\mathrm{cov}(d, f). \tag{2.31}$$

The position resolution is given by the uncertainty in d, σ_d. There are two approaches to calculating σ_d; the simplest way is by excluding the plane in question from the fit, which gives a covariance term of zero. Alternatively the plane in question is included in the fit and the covariance term, which comes from the χ^2 formalism, becomes σ_f^2 [101]. The latter method is slightly more precise due to the smaller fit error arising from using an extra plane in the fit, and is therefore used here; however both methods showed consistency. Equation 2.31 now becomes

$$\sigma_r^2 = \sigma_d^2 - \sigma_f^2. \tag{2.32}$$

The fit error comes from the differential of equation 2.20, and is given by

$$\sigma_f^2 = \sigma_{x_0}^2 + z^2\sigma_\theta^2 + 2\,z\,\mathrm{cov}(x_0,\theta) \tag{2.33}$$

where σ_{x_0}, σ_θ and $\mathrm{cov}(x_0,\theta)$ are the uncertainty and covariance of the fit parameters, and come from equation 2.26. The residual distribution gives a measurement of σ_r, allowing σ_d to be calculated from equation 2.32. However, as f is itself a function of σ_d, the input values of the sensor resolutions are varied iteratively until equation 2.32 is approximately satisfied. Near the true resolution, the relation between σ_f and σ_d is approximately linear, and can be easily parameterised by calculation. We can then say that

$$\sigma_f = \frac{\partial\sigma_f}{\partial\sigma_d}\sigma_d + \mathrm{constant} \tag{2.34}$$

Substitution of this into equation 2.32 gives a quadratic relation between σ_r^2 and σ_d, which can be solved for σ_d.

This method has been used to estimate the spatial resolution in x and y for each of the five planes. Table 2.2 gives the estimated sensor spatial resolutions for all ten sensors. This approach yields an average sensor resolution of 6.92 ± 0.05 μm, which is significantly better than the binary resolution of pitch/$\sqrt{12} = 17.3$ μm. This can be largely accounted for by the intermediate floating strip, which effectively halves the readout pitch of 60 μm.

Table 2.2: Plane spatial resolutions.

Plane	Sensor	σ_f [μm]	σ_r [μm]	σ_d [μm]
1	x	6.90	1.42	7.05
1	y	6.90	1.41	7.05
2	x	4.01	5.57	6.86
2	y	4.01	5.71	6.97
3	x	4.01	5.21	6.58
3	y	4.01	5.63	6.91
4	x	4.01	5.76	7.02
4	y	4.01	5.35	6.69
5	x	6.91	1.39	7.05
5	y	6.91	1.37	7.04

An estimate of the resolution of x_0, σ_{x_0}, for the bent track fit comes from equation 2.26. The value of σ_{x_0} obtained for 400 GeV protons is 4.2 μm (assuming that all sensors have spatial resolution 6.92 μm). As expected, this is better than the spatial resolution of an individual plane, and is sufficiently small to make good position cuts for tracks incident on a strip crystal, and to see any edge effects that may occur as a result of particles impacting the edge of a crystal.

2.8.4 Angular resolution

There are two angular measurements that are useful for crystal channeling studies when using the bent track fit. Firstly the resolution of the deflection angle, $\Delta\theta = \theta_2 - \theta_1$, is of interest, as the angular deflection allows identification of channeled particles. Secondly the resolution of the incident angle, θ_1, is important as cuts on the incident angle allow the selection of only tracks incident on a crystal within the channeling acceptance angle to be made during analysis.

In order to estimate the deflection resolution, $\sigma_{\Delta\theta}$, it was necessary to look at the distribution of measured deflections, using the bent track fit, of tracks that were known to be straight due to the absence of a crystal in the beam. Figure 2.21 shows the distribution of measured deflections for such straight tracks in x and y. The distributions are approximately Gaussian with standard deviation of 5.2 μrad in both x and y, which provides an estimate for the deflection resolution. This

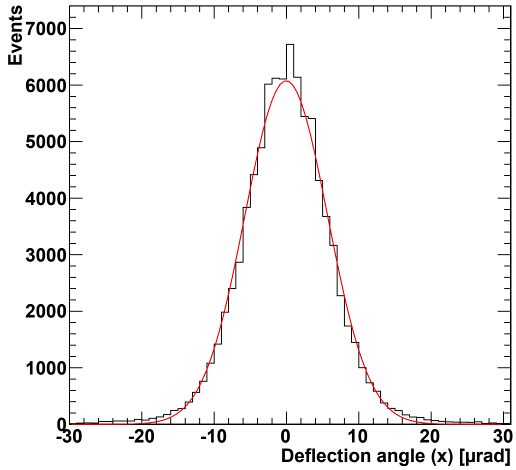

(a)

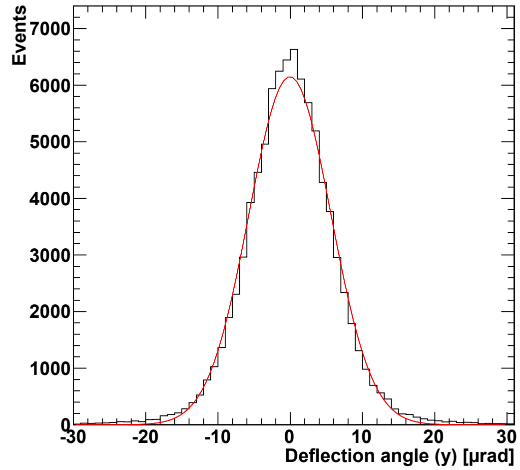

(b)

Figure 2.21: Distribution of measured proton deflection angles for straight tracks ($\Delta\theta = \theta_2 - \theta_1$) using the bent track fit, for deflections in (a) x and (b) y.

is sufficiently small to observe the effects of a bent crystal, such as channeling and volume reflection, which occur at deflections of $\sim$100 μrad and $\sim$10 μrad respectively (see Figure 2.3).

The uncertainty in the deflection measurement is also provided by the covariance matrix (equation 2.29). Assuming sensor resolutions of 6.9 μm and 400 GeV protons the uncertainty in deflection is 4.3 μrad, which is reasonably consistent with the measured deflection resolution of 5.2 μrad. The discrepancy could be explained by an underestimation of the expected scatter angle.

It is not possible to measure the resolution of the incident angle as the true angle of a track cannot be known for a beam of non-zero divergence. An estimate of the incident angular resolution, σ_{θ_1}, of 2.5 μrad is however obtained from equation 2.29. This value is smaller than the expected channeling acceptance angle for 400 GeV protons of 10 μrad, indicating that the telescope is capable of providing useful selection cuts on incident angle.

2.8.5 Impact parameter distribution

The impact parameter at the crystal position is an important parameter for analyses as it allows the selection of only those events in which tracks are incident on the crystal. It also allows any spatial variation in channeling characteristics such as efficiency and deflection angle to be observed. The reconstructed impact parameter resolution is heavily dominated by the planes adjacent to the crystal, and is smallest when these planes are closest to the crystal. With planes at typical distances from the crystal, the reconstructed impact parameter resolution is estimated from equation 2.29 to be 4.19 μm; better than the 6.91 μm seen with the individual sensors.

One might expect a hit distribution to be a smooth function, and roughly uniform across a narrow section of the beam. However there is a periodicity observed in reconstructed hit distributions, and due to the close proximity of the sensors to the crystal this periodicity also appears in the reconstructed impact parameter distributions. Figure 2.22a shows a typical distribution of impact positions, and this periodicity is clearly seen. The periodicity coincides with the strip readout pitch of 60 μm, and is due to the inadequacy of the linear interpolation used. In estimating the hit position of a multistrip cluster, the η parameter is defined according to equation 2.10. As a hit distribution would be expected to be uniform across the pitch of a strip, the η distribution should therefore also be uniform. Figure 2.22b shows the η distribution, and a clear non-uniformity is seen. The peaks at 0 and 1 show that charge is not distributed linearly between strips according to equation 2.10, but preferentially to the closest strip. The central peak is due to the effect of the intermediate floating strip, which shares charge evenly between the adjacent readout strips.

The problem of the non-uniform η distribution can be overcome by using a non-linear interpolation function, which comes from the cumulative η distribution. Figure 2.23 shows this cumulative η distribution, which leads to a smoother impact parameter distribution. Use of this non-linear interpolation does however increase sensor spatial resolution to $\sim$8.8 μm due to non-Gaussian tails in the residual distributions. This

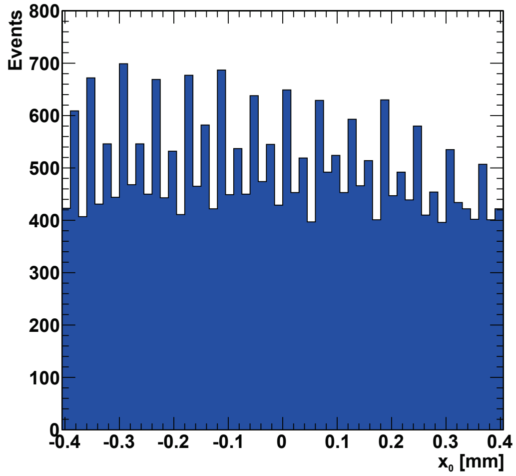

(a)

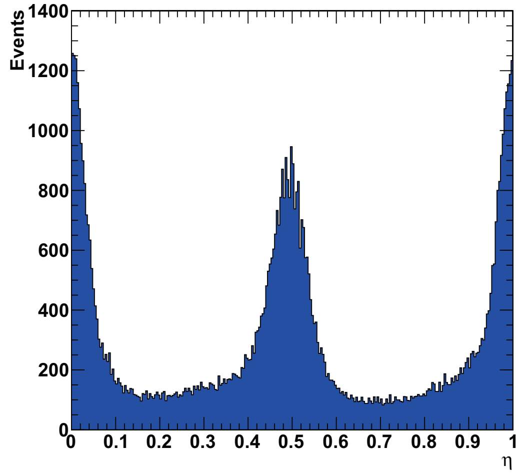

(b)

Figure 2.22: (a) Distribution of reconstructed impact parameter. A clear 60 μm periodic pattern is seen. (b) η distribution showing the non-linearity of charge sharing.

subsequently increases the reconstructed impact position resolution to 11.4 μm. The method also adds an extra stage to commissioning, as the cumulative η function needs to be obtained for each sensor, or ideally each APV25 chip.

The periodicity could also be reduced by ignoring events with single strip clusters on planes adjacent to the crystal, though this would be at the cost of tracking efficiency. Tilting sensors about the y-axis would increase the proportion of multistrip clusters by effectively reducing the pitch, although the periodicity would still remain as a result of the non-uniform η distribution. This would again require further commissioning steps as the effective pitch would need to be accurately deduced, and if planes were tilted about both x and y then strips would no longer be orthogonal in the x-y plane which would lead to further complications in commissioning.

2.9 Crystal channeling studies

Many crystals were tested over the course of the beam tests, with varied success. There were a number of problems that routinely occurred during the tests, which made channeling observations extremely challenging. Problems included frequent long periods without beam, goniometer malfunction or commissioning complications,

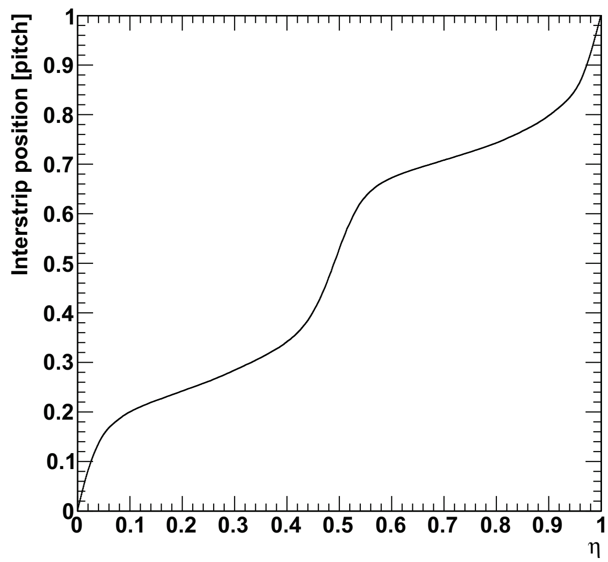

Figure 2.23: Cumulative η distribution, from which improved interpolation can be achieved.

and errors in the DAQ system and online analysis. After each intervention in the beam area the telescope needed its alignment parameters adjusted, and if not done properly by those on shift would lead to very low tracking efficiency. In addition to the problems associated with the experimental apparatus, problems with the crystals under test were frequently evident. Crystal imperfections such as miscut errors on the front face or lattice imperfections often meant that efficiency was low and no signs of channeling could be observed during online monitoring of angular scans. Due to the associated problems and time constraints, good channeling observations were rare. In general better channeling observations were made with strip crystals over quasi-mosaic crystals, and this section presents the analysis of two strip crystals from the September 2011 run: STF48 and STF49. The aim of this section is not to typify the results, but to demonstrate what observations are capable of being achieved with the telescope, and the methodology involved.

2.9.1 General method for finding crystal channeling

After any intervention in the beam area it is necessary to perform an alignment run in which any crystal is removed from the beam line and $\sim 10^5$ events are collected.

This allows the telescope planes to be realigned following any disturbances, using the software alignment procedure (Section 2.8.2).

Strips are aligned in the beam vertically by convention, such that any channeling effects are seen as horizontal deflections. As a strip is typically of width ~1 mm it must be positioned carefully in the beam so as to maximise the number of incident particles. A strip is translated in x by the goniometer until it reaches a suitable position in the beam. The position of the strip can be inferred from increased angular deflection due to amorphous scattering over a range in x that is equivalent to the strip width.

Once the strip is in a suitable x position it is rotated about y during an angular scan run, at a rate typically 10^5-10^6 events/μrad. Online analysis of the angular scan allows the correct channeling orientation to be found, indicated by a large horizontal deflection in x that corresponds to the crystal bend radius, typically ~100 μrad. A high statistic run can then be performed with the crystal in the correct orientation for channeling.

The telescope can then be used in offline analysis to make selection cuts on position and incident angle in order to select only tracks incident on the crystal and at the desired angle.

2.9.2 Channeling observations

A high statistic run was performed on strip crystal STF49, with ~4.3 million events collected. Following the translational and rotational positioning of the crystal in the beam, it was possible to observe crystal channeling. Figure 2.24 shows the horizontal deflection of tracks as a function of horizontal impact position. A large deflection is seen in the region -0.2 mm $< x <$ 0.4 mm, corresponding to the position of the crystal. The deflection angle is -250 μrad, corresponding to the crystal bend angle.

For crystal channeling studies, only events in which particles are incident on the crystal are of interest. Selection cuts can be made offline to ignore all events that fall outside this region. Figure 2.25 shows the deflection angle as a function of

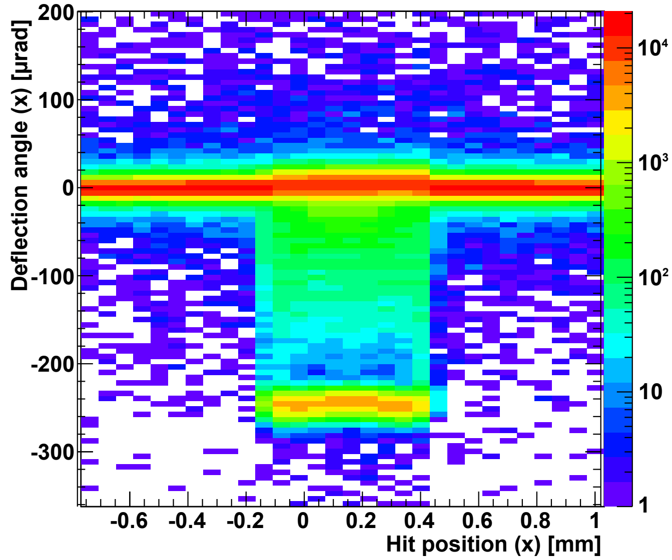

Figure 2.24: Deflection in x as a function of impact position in x.

the horizontal incident angle, where only tracks incident in the region -0.2 mm $< x < 0.4$ mm are selected. The incident angle used is the angle at which a track is incident relative to the crystal planes. Torsion in the strip means that the alignment of crystal planes will in general not be constant in y, so a correction must be applied to all incident angles. This torsion correction is the subject of Section 2.9.3.

It can be seen in Figure 2.25 that the deflection angle follows the general form expected from a crystal channeling scan (compare with Figure 2.3). For $\theta_1 < 0$, small deflections about zero are measured, corresponding to the combined effects of amorphous scattering and the non-zero angular resolution. For $\theta_1 > 0$ a region of volume reflection is seen, where particles undergo a small positive deflection of $\sim$10 μrad. The channeling peak for deflections of $\sim$250 μrad is visible at $\theta_1 = 0$ μrad. A region of dechanneling is also visible at $\theta_1 = 0$ μrad, between the channeling peak and amorphous region, corresponding to particles that were channeled only initially, before emerging from the crystal with some intermediate deflection. A wider scan would highlight the volume capture and amorphous scatter regions for $\theta_1 \neq 0$ μrad.

In order to quantify the channeling efficiency of a crystal, it is necessary to make further selection cuts on the incident angle, so as to ignore all tracks incident at large angles relative to the crystal planes. Figure 2.26 shows histograms of deflection

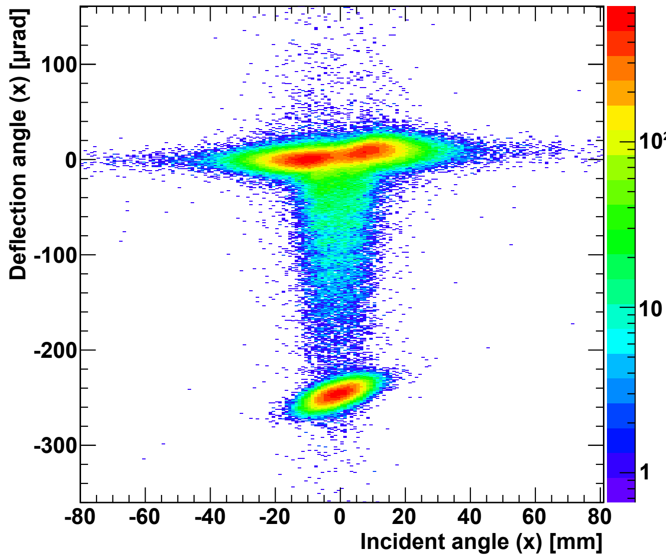

Figure 2.25: Deflection in x as a function of x incident angle (after torsion correction). Data are following an x position cut for particles incident on the crystal.

angle for particles incident on the crystal within angular ranges of $|\theta_1| < 10$ μrad and $|\theta_1| < 5$ μrad. In both cases the channeling peak is again visible at -250 μrad. The channeling efficiency is estimated as the proportion of all events subject to the position and angular cuts, that fall within the channeling peak (assumed to be -300 μrad $< \Delta\theta < -200$ μrad). Efficiency is seen to be 36.8$\pm$0.1% and 48.8$\pm$0.2% for $\pm$10 μrad and $\pm$5 μrad cuts respectively (errors are statistical). A further cut of $\pm$2.5 μrad increases the efficiency by only $\sim$2% but reduces the data available by $\sim$50%.

2.9.3 Observation of torsion

Torsion in a strip crystal results in crystal planes being aligned at angles varying in y. This would lead to a variation in channeling efficiency for tracks of a certain incident angle with vertical position y. In order to correct for this effect the telescope must be used to measure the torsion in the strip.

A high statistic run was performed on strip crystal STF48, which showed relatively high torsion, with $\sim$6.1 million events collected. Figure 2.27a shows the channeling

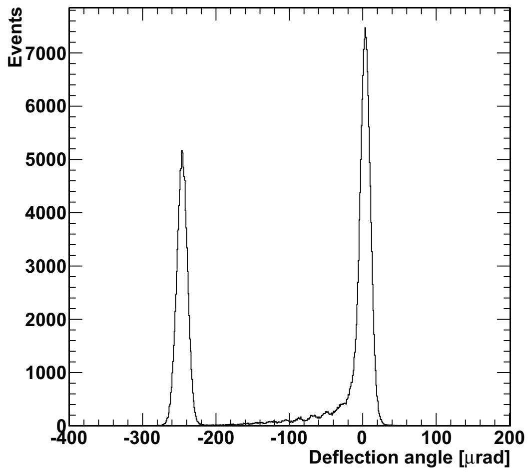

(a)

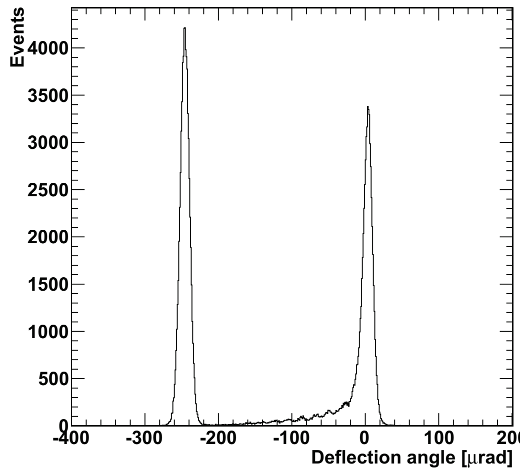

(b)

Figure 2.26: Deflection in x for all particles incident on the crystal, within an incident angle acceptance of (a) ± 10 μrad and (b) ± 5 μrad. The channeling peak is visible at ~ -250 μrad.

efficiency as a function of vertical impact position, y, and incident angle, θ_1. It is clear that the optimum angle for channeling occurs at different incident angles for different vertical positions, indicating torsion. Figure 2.27b shows the same data plotted in a profile histogram, with the mean and RMS used for the values and their errors. A linear relation is seen, and a best fit between $y = \pm 2$ mm gives a torsion value of 6.99 μrad mm^{-1}. An offset of 6.16 μrad is also seen.

This effect is corrected for as part of the offline analysis. The adjusted incident angle, θ_1', is given by the following relation

$$\theta_1' = \theta_1 - ay - b \tag{2.35}$$

where a is the measured torsion and b is the offset that must be applied to make the optimum incident angle for channeling 0 μrad. Figure 2.28 plots the same data as Figure 2.27 after the torsion correction. The distribution is clearly more constant with y, indicating that any cuts on incident angle would reject fewer tracks that are incident on the crystal planes at suitable channeling angles.

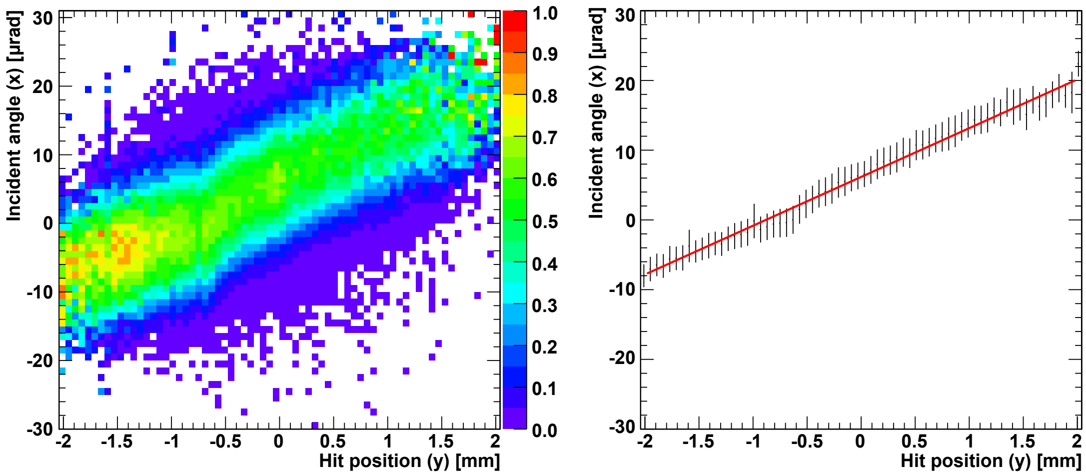

(a) (b)

Figure 2.27: (a) Channeling efficiency as a function of y hit position and x incident angle *before* torsion correction. Data are following an x position cut on particles incident on the crystal. (b) Incident angle of peak efficiency as a function of hit position.

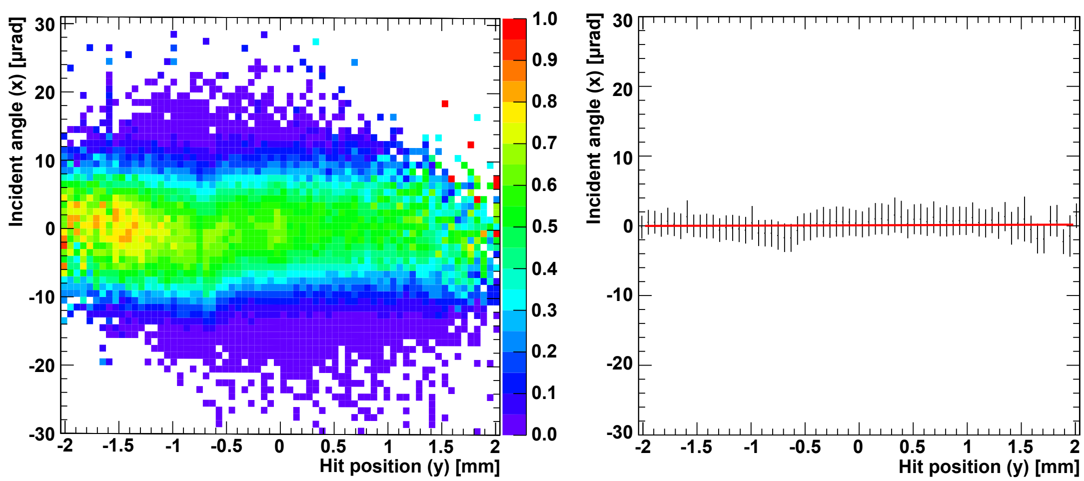

(a) (b)

Figure 2.28: (a) Channeling efficiency as a function of y hit position and x incident angle *after* torsion correction. Data are following an x position cut on particles incident on the crystal. (b) Incident angle of peak efficiency as a function of hit position. The distribution is clearly more constant in y than before the correction (see Figure 2.27).

2.10 Summary

A tracking telescope has been designed and constructed for high rate measurements of charged particle trajectories, with the specific objective of measuring the deflection of protons through bent silicon crystals as part of the UA9 collaboration. The telescope comprises five planes of orthogonal 60 μm pitch silicon strip sensors, and a readout and data acquisition system based heavily on that of the CMS detector.

Two methods were used for reconstruction of tracks. Firstly, in the absence of a crystal, straight tracks are expected. Correlated scatter position errors propagate out from the region of the telescope in which reconstruction is required, and a straight line, two parameter fit in both x and y is provided. Secondly, where a crystal is present in the beam, a three parameter fit is made, providing incident and outgoing angles and a common intercept at the crystal, in both x and y.

The telescope was shown to perform well. Sensors showed good signal to noise performance, and provided an average spatial resolution of 6.92 ± 0.05 μm. Resolution on the crystal deflection angle was measured to be 5.2 μrad, which is sufficient for observation of channeling phenomena. Resolution on the incident angle was estimated to be 2.6 μrad, which is sufficiently small to make selection cuts on incident angle in order to isolate certain crystal phenomena.

The telescope was used to measure the trajectories of protons through a bent crystal. The effect of crystal channeling was observed, with channeling efficiencies of up to 50% measured. The crystal effects of volume reflection and dechanneling were also observed. Torsion in strip crystals was also seen, through the variation of channeling efficiency and incident angle along the length of a strip.

Chapter 3

Telescope performance with a heavy ion beam

The charged particle telescope described in Chapter 2 has been tested in a heavy ion beam. The operation of the telescope in a heavy ion beam is significantly different from that in a proton beam due to the much larger signals produced in the sensors. This chapter outlines the issues related to the use of the telescope in the ion beam, and presents results from its use under such conditions.

3.1 Introduction

The LHC heavy ion program began in 2010 with Pb-Pb collisions at centre of mass energy $\sqrt{s} = 2.76$ TeV per nucleon; more than an order of magnitude greater than that available at the RHIC [10]. This is set to rise eventually to its maximum design energy of $\sqrt{s} = 5.5$ TeV. Design luminosity is relatively low at $\sim 10^{27}$ cm^{-2}s^{-1} (per A^2), limited by copious electromagnetic interactions in peripheral collisions that would otherwise cause quenching of the superconducting magnets [102]. As with p-p collisions, improved collimation is needed to allow the luminosity to be increased.

UA9 aims to demonstrate the feasibility of using crystal channeling as a method of collimation. As well as demonstrating the feasibility of channeling protons, UA9 aims to show that the same effect can be employed with heavy ions. Equation 2.6

gives the critical angle below which channeling of protons can occur. For an ion of charge and mass numbers Z and A respectively, the critical angle becomes

$$\theta_{\mathrm{C}} = \sqrt{\frac{2U_0}{E}\frac{Z}{A}}. \tag{3.1}$$

This shows that for a 2.25 TeV per nucleon beam of fully stripped lead ions the critical angle is $\sim$2.6 μrad. This is only slightly larger than the $\sim$2.4 μrad associated with a 7 TeV proton beam, indicating that the critical angle poses no further limit on the feasibility of crystal channeling of heavy ions.

Crystal channeling of fully stripped gold ions has been observed at RHIC, where a PIN diode was used to measure the beam count rate, 9.8 m downstream of a crystal with bend angle 440 μrad [10]. The channeling efficiency was measured by scanning the crystal through a range of $\sim$2 mrad and observing the count rate at the PIN diode. Channeling and volume reflection orientations were identified by a reduction in count rate over a range of $\sim$100 μrad, and the channeling efficiency could be estimated. Though channeling was seen, efficiencies were low, in part due to the relatively large beam divergence, meaning that even with the crystal at the optimum angle relative to the nominal beam direction, many particle trajectories would not fall within the channeling acceptance.

In order to characterise channeling phenomena more precisely, a tracking system would be required. The telescope described in Chapter 2 allows 3-dimensional reconstruction of particle trajectories, providing measurements of deflection angle and incident angle, as well as the impact position on a crystal. This allows selection cuts on these parameters to be made in order to fully characterise the crystal effects under consideration.

The transfer of the telescope from use with protons to heavy ions is not trivial. The module electronics were designed to read out small signals, such as the MIP signals associated with the 400 GeV proton beam, and it was not clear whether they would function as required in the new environment. Furthermore, even if the modules were able to operate, charge sharing may distribute the large signals too much, at the cost of spatial resolution, and a subsequent worsening of angular resolution.

3.2 The APV25 response to highly ionising events

The APV25 readout chip was designed to read out signals of a few MIPs (1 MIP $\sim$ 25000 electrons in 300 μm silicon). The chip's digital header is designed to occupy a range equivalent to an 8 MIP signal, with good linearity seen up to a few MIPs [25]. However, inelastic interactions within the SST can generate a high local density of ionised charge within the bulk material through the production of heavily ionising particles (HIPs), such as recoiling nuclei or nuclear fragments. Simulations have shown that such HIPs can have energies of the order $\sim$10 MeV [103], and can result in signals equivalent to up to $\sim$1000 MIPs [104].

HIP events are simple to identify due to the characteristic response of the APV25 chip to the large energy deposition. Such events were first observed in the CERN X5 beamline in 2001 [105], where six modules, each consisting of a 500 μm sensor instrumented by four APV25 chips, were exposed to a 120 GeV pion beam. Further measurements were made in 2002 in the PSI facility and again at the X5 facility [106]. Figure 3.1 shows a typical HIP event, plotting the raw data (post pedestal subtraction) for all 512 channels of the affected sensor [106]. Large signals are observed on a few channels of APV 2, corresponding to a large energy deposition from a HIP event. However, the outputs of all other channels on that chip are driven down to a level well below their normal pedestal values. The saturation of the chip has been shown to persist for several hundred nanoseconds, during which the baseline recovers to its normal value. This effect can lead to temporary inefficiencies in all channels of the chip, resulting in deadtime in the detector [103].

The probability of such events occurring in the SST is low; estimates for the production of a HIP event from a 300 MeV pion traversing 320 μm silicon are at the 10^{-3} level [103]. The measurements of the HIP event probability and the mean inefficiency induced by HIP events have been combined with Monte Carlo estimates of particle fluxes in CMS, to give an estimate of the overall track reconstruction inefficiency due to the effect of HIPs in the SST. This induced inefficiencies were seen to be at the percent level, and to have negligible impact on the physics performance of the SST [103].

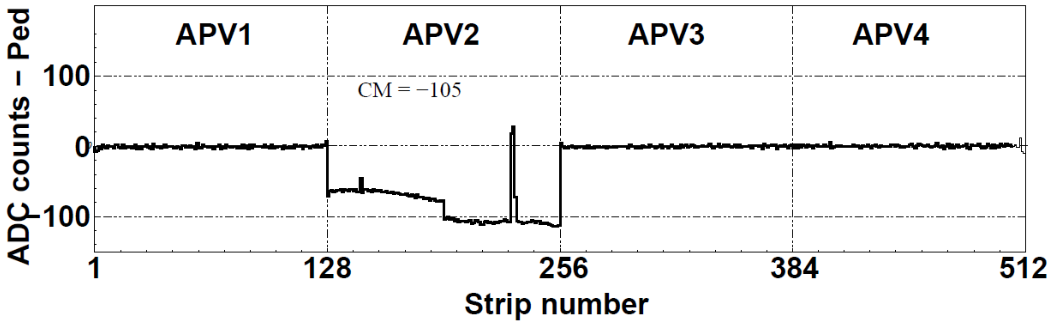

Figure 3.1: Raw data (pedestals subtracted) from the four APV25 chips in a TOB module. A HIP event is identified in the second chip by the cluster of saturated strips and the large negative common mode value [106].

The saturation of the APV25 chip can be attributed to crosstalk effects caused by large signals, enhanced by the powering scheme of the APV25 front-end. The large signals generated in HIP events saturate only a few channels in the APV25, however the design of the biasing at the inverter stage results in all 128 channels being affected. Figure 3.2 shows a circuit diagram of the front-end amplifying stages of a single APV25 channel. The inverter stage is powered by a 2.5 V supply rail, via an external resistor, R_{inv}, which is common to all 128 channels. With this scheme any common mode signal, V_{CM}, is not seen on internal inverter output nodes, but on the external resistor ($V_{\mathrm{R}} \approx V_{\mathrm{CM}}$). This was considered at the design stage to be advantageous during normal operation, due to the beneficial feature of providing on-chip common mode subtraction, giving a very stable baseline. However, a very large signal, such as that from a HIP, at one or more of the inverter input nodes, V_{in}, will drive down V_{R}. As V_{R} is common to all channels, this has the consequence of driving down the inverter output of all other channels in the chip, and is seen as a shift in the analogue levels of these channels. Each channel will remain insensitive to normal signals until the signal dissipates sufficiently for the chip to recover to its normal value, leading to deadtime [103, 105].

3.3 Experimental setup

In November and December of 2011 the telescope described in Chapter 2 was used to provide tracking of heavy ions in the H8 beamline for the UA9 collaboration.

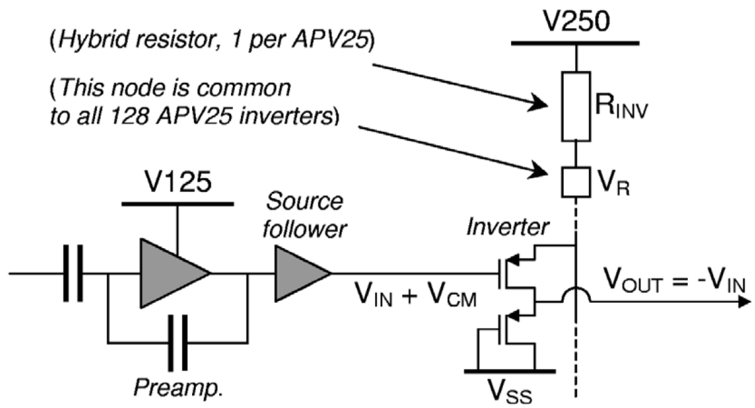

Figure 3.2: Front-end amplifying stages of a single APV25 channel [105].

The following sections describe the experimental setup and the performance of the telescope throughout the beam test.

3.3.1 Heavy ion beam

A primary beam of Pb^{82+} can be extracted from the SPS. The primary beam generally remains clean, unless part of beam hits the aperture and produces fragments from nuclear interactions. A maximum intensity of $\sim 10^9$ ions per spill is achievable. It is possible to generate a fragmented beam by inserting the T4 target into the beamline, upstream of the H8. Nuclear interactions generate a secondary beam of fragments across the full spectrum of isotopes, allowing the study of different species without having to change the ion source or re-tune the whole accelerator chain. All ions, including primary Pb^{82+} and fragmented nuclei, are selected by mass spectrometry based on their rigidity, R. We define rigidity here as

$$R = \frac{A}{Z}\, p \tag{3.2}$$

where p is the momentum per nucleon. Clearly for a proton beam the rigidity is simply the momentum. For an ion beam the rigidity is the "proton equivalent" momentum, ie the momentum that a proton beam would have if it behaved in the same way as the ion beam in an electromagnetic field. Selected fragments would have the same Z/A as the primary beam species, however Fermi motion within the target causes a spread in the momentum of a few percent, leading to a corresponding spread in the Z/A of the secondary beam. For this reason, Z/A will be close, but not necessarily equal, to the Z/A of the primary beam.

During the November 2011 beam test, the primary beam available from the SPS was Pb^{82+} ($A = 208$), which corresponds to $Z/A = 0.394$. Beam conditions during the test were in general suboptimal. There were extended periods without beam, and when beam was available it was rarely clear whether it was a primary or secondary beam, and which beam species were present. For this reason a thorough and precise analysis of the data was impossible, however certain conclusions about the general performance of the telescope in the presence of an ion beam can still be made. The maximum beam rigidity available was 160 GeV/c, which corresponds to a momentum per nucleon of 63.1 GeV/c for all particles of $Z/A = 0.394$.

3.3.2 Telescope setup

The use of the telescope in the heavy ion beam was expected to differ from use in the proton beam due to the response of the APV25 to the large signals expected. The Bethe-Bloch formula [100] can be used to estimate the energy loss in each telescope sensor. For a 63.1 GeV per nucleon Pb^{82+} ion the expected energy loss in 320 μm of silicon is 379 MeV, corresponding to $\sim$4200 MIPs. Such signals are far beyond those at which the APV25 saturation begins, so it was foreseen that the telescope would need to operate despite chip saturation.

The telescope hardware was set up exactly the same as that described in Section 2.5, however the trigger was moved upstream of the telescope in order to avoid discriminating against events in which nuclear interactions occurred within a crystal. When using the telescope to measure proton trajectories it is possible to operate the FED in zero suppressed mode, in which data are digitised, reordered and zero suppressed, and pedestal and common mode noise subtraction are performed. Due to the chip saturation effect from of large signals expected in the ion beam, the conventional zero suppression algorithm was no longer appropriate for use in hit finding. For this reason data were collected with the FED operating in processed raw mode, with further processing to be done offline.

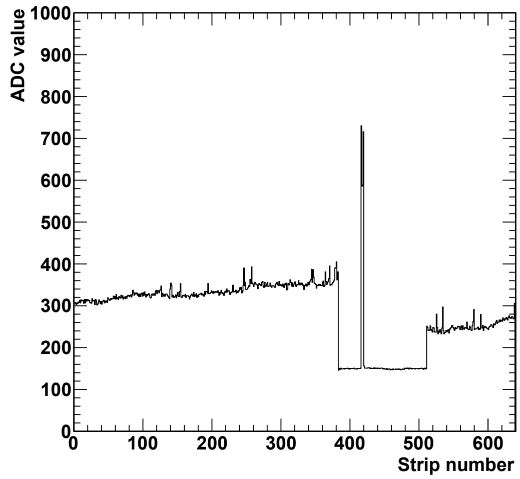

(a)

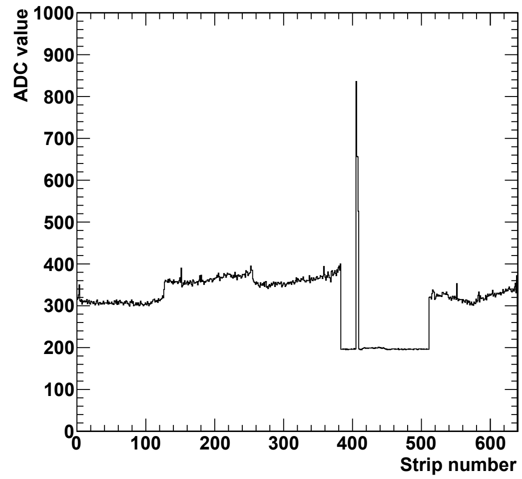

(b)

Figure 3.3: An example HIP event for plane 5. Processed raw data are shown. (a) x sensor, (b) y sensor.

3.4 Preliminary tests

Before the full telescope was installed preliminary measurements were made with a single plane (plane 5) in order to assess its performance. The telescope planes were operated with a reduced bias voltage in order to suppress the large signals expected by reducing the size of the depletion region. Figure 3.3 shows an example of the raw digi data for plane 5 (both x and y) for a single event, when operated with a reverse bias of 3 V (compared with 150 V when operated with the proton beam). The data frames show the same characteristic chip saturation as seen previously, with a hit causing saturation in the fourth APV25 of both x and y sensors. In order to generate hits from such digis, a suitable clustering algorithm was required.

3.4.1 HIP-suppression algorithm

As the zero suppression operational mode of the FED is not appropriate for use with heavy ions, raw data must be processed in the offline software. In order to create hits and tracks from the raw digis, it was necessary to implement a new "HIP-suppression" algorithm to use in place of the conventional zero suppression algorithm. This could then be used to process the raw digis into HIP-suppressed digis, equivalent to the conventional zero suppressed digis, so that the standard reconstruction chain of clustering and track finding could then be used in the usual way.

The HIP-suppression algorithm relies upon identifying strips in which the ADC value is much greater than the baseline level of the particular APV25, as expected with a HIP event such as those displayed in Figure 3.3. Identification of such strips is done by requiring that the ADC value for a strip is greater than 200 ADC counts over the median ADC value of the relevant APV25 chip. The threshold of 200 is used as it is sufficiently high to discriminate HIP events from background MIP events, but sufficiently low not to exclude the HIP events. Using the median value for each chip accounts for the variation in baseline between chips, and ensures that a sufficiently low baseline is assumed. Such identified strips are then selected and all others associated with the relevant APV25 are suppressed. The ADC value assigned in the HIP-suppressed digis is limited to 255 for consistency with the 8-bit digitisation of the standard zero suppression mode. In the example data frames shown in Figure 3.3 the median ADC values of the saturated chips are 150 and 197 for x and y respectively. Taking a threshold of 200 ADC counts above these values leaves clusters of four strips remaining in both x and y.

3.4.2 Cluster width distribution

The cluster width is a consideration for spatial resolution, and it was important to determine how this varies with bias voltage. Figure 3.4a shows the cluster width distribution for both sensors of plane 5, with a reverse bias voltage of 3 V applied. The mean widths are 3.02 and 3.23 strips in x and y respectively, and the standard deviations in the distributions are 1.07 and 1.08 strips. Figure 3.4b shows the average cluster width as a function of reverse bias voltage (including data collected with forward bias). Error bars represent the standard deviation of the distributions.

Cluster widths depend not only on the size of the signal, but also on the transverse distribution of the charge that occurs due to diffusion during charge collection. Whereas increased bias voltage gives larger signals by increasing the size of

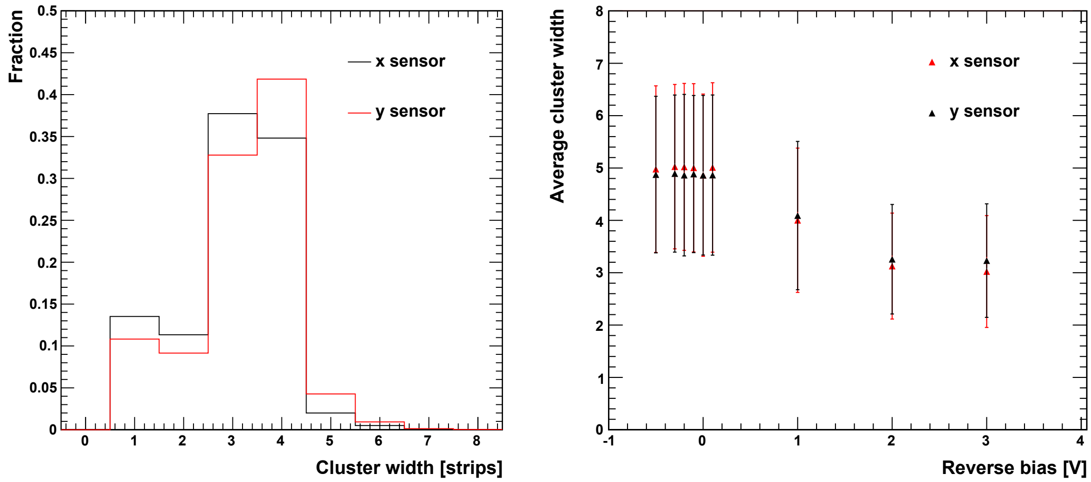

(a) (b)

Figure 3.4: (a) Cluster width distribution for both x and y sensors of plane 5, operated with reverse bias of 3 V. (b) Variation of cluster width with reverse bias.

the depletion region, it also reduces the charge collection time and hence the transverse diffusion, thus giving rise to the smaller clusters seen in Figure 3.4b. For all subsequent analyses, the reverse bias voltage was set to 0.5 V.

3.5 Reconstruction

Data analysed in the following three sections are from runs in which the ion beam had the maximum available rigidity of 160 GeV/c, corresponding to a momentum of 63.1 GeV/c per nucleon.

3.5.1 Hit reconstruction

The conventional method of reconstructing hits from zero suppressed digis is described in Section 2.7.1, and involves taking the barycentre of the cluster by interpolating the charge on the pair of adjacent strips with the greatest total signal. This method is not appropriate in the case of HIP-suppressed digis; the charge deposition on each strip is not a good indicator of the position of the incident particle or the amplitude of the charge deposited. Furthermore, where hits are divided across

Table 3.1: Plane efficiencies.

Plane	Efficiency(%)
1	99.99
2	99.61
3	99.69
4	99.83
5	98.77

APV25 boundaries, different median baseline values are used in the HIP-suppression algorithm and the subsequent ADC values of adjacent strips in the digis would in general be discontinuous.

A simpler clustering algorithm involves simply taking the mid-point of clusters in the HIP-suppressed digis, irrespective of the ADC value of each strip. This is effectively using the APV25 as a binary chip, but with the threshold discrimination being done off-chip. The mid-point clustering method is used to generate hits, from which straight and bent tracks can be generated in the same way as described in Section 2.7.

The hit finding efficiency of a particular plane can be estimated by selecting straight tracks in which a single hit is reconstructed in all other planes, and then considering the plane efficient if one or more hits are reconstructed. Table 3.1 shows the efficiency of each plane. Very good efficiency is seen in all planes with an average of 99.6%, equivalent to 99.8% per single sensor.

Figure 3.5 shows the multiplicity of hits on plane 3, again with a selection of straight tracks with a single hit on all other planes. It can be seen that single cluster events dominate, with a small number of events leading to multiple hits. Note that four hit events are generally the result of there being two hits in each of the two sensors of a plane. Inspection of the raw data frames for multiplicities of 0 and >1 indicate the reasons for such features. Figure 3.6 shows typical data frames from which 0 and 2 hits have been reconstructed (only the APV corresponding to the hit position is shown). In the case that no hits are reconstructed (Figure 3.6a), the baseline has not dropped fully and the larger signals are not sufficiently high above the median signal for a cluster to be reconstructed. Inspection of other planes from the same event shows that no other APV25s become saturated, but that the HIP-suppression

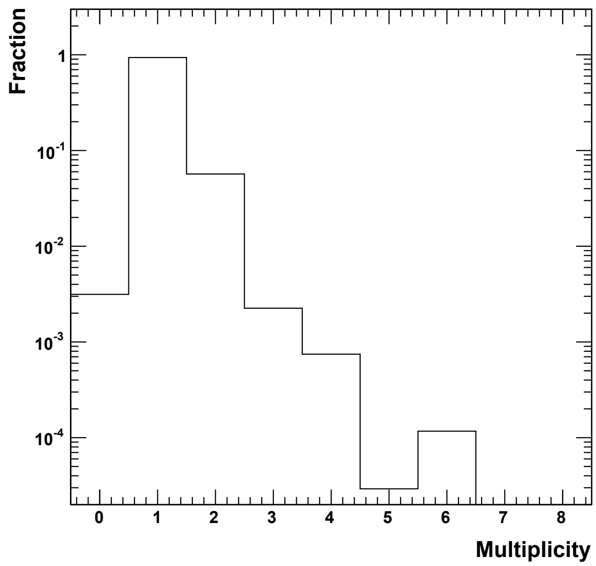

Figure 3.5: Multiplicity on plane 3, for tracks in which a single hit has been seen on all other planes.

algorithm still reconstructs a hit. Such signals are therefore consistent with MIPs, and such inefficiencies tend not to be from failing to reconstruct a HIP event, but from reconstructing a MIP event in all other sensors. Figure 3.6b shows a typical event in which two clusters are reconstructed from a single track. It is clear that this is actually one cluster that has been divided due to a drop in the signal to below the threshold, within the cluster. Such clusters tend to occur mostly at chip boundaries, where discontinuities can arise in the signals seen in strips in the raw data.

Figure 3.7a, shows the cluster width distribution for plane 5 obtained from the 63.1 A GeV beam, with mean cluster widths of 5.24 and 5.02 strips in x and y respectively. Figure 3.7b displays both distributions plotted in a 2-dimensional histogram, and shows a correlation between cluster width on x and y planes. In any given event both x and y sensors clearly see the same particle, so the consistency in cluster width between the two sensors indicates a clear relation between cluster width and energy deposition.

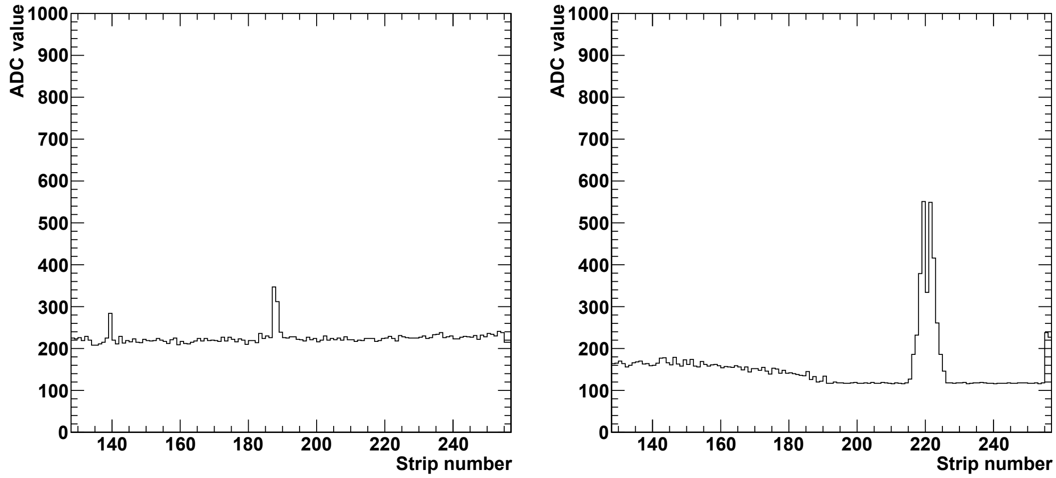

(a) (b)

Figure 3.6: Example HIP events for plane 3 x, APV 2. (a) Hit reconstruction algorithm is inefficient. (b) Hit reconstruction algorithm leads to two hits.

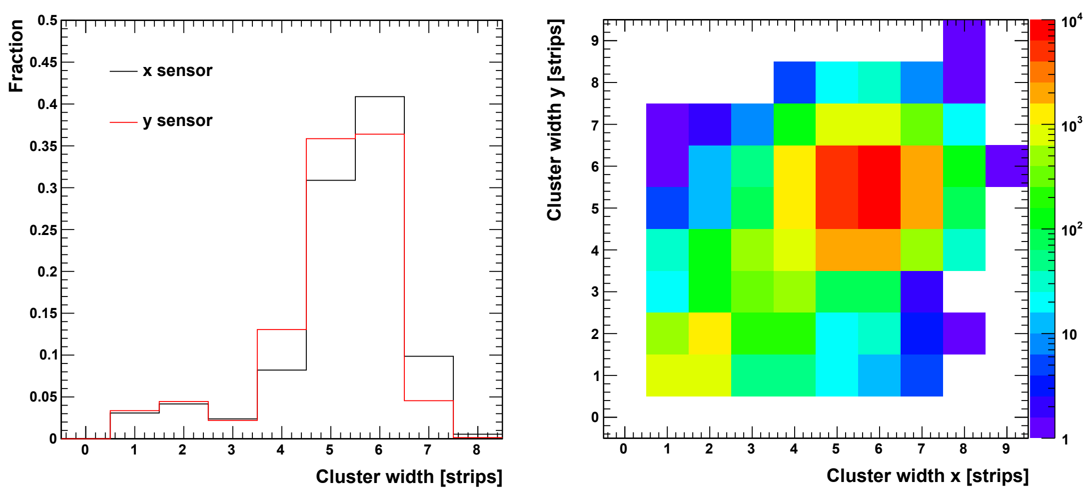

(a) (b)

Figure 3.7: (a) Cluster width distribution for both x and y sensors of plane 5, operated with reverse bias of 3 V. (b) Cluster width distribution in both x and y, with consistency shown between sensors.

3.5.2 Track reconstruction

Track reconstruction proceeds in the same way as with use in the proton beam (Section 2.7). Single track reconstruction can be used to reconstruct straight tracks at any position in the telescope, and is used for events in which no crystal is in the beamline, and for assessing the performance of the telescope planes. Bent tracks provide both incident and outgoing tracks that meet at the crystal, and are used for channeling studies. The reconstructed track uncertainty is dependent on plane spatial resolution and the multiple scatter from the sensor material. Plane resolutions are discussed in Section 3.6. The expected scatter angle leads to error correlations between planes, and is estimated from equation 2.11. For ions of $Z/A = 0.394$ and momentum $63.1A$ GeV/c, this is 5.74 μrad (assuming 640 μm silicon and 60 μm aluminium per plane).

3.6 Telescope performance

3.6.1 Spatial resolution

Determination of sensor spatial resolutions proceeded in the same way as in Section 2.8.3. Residuals were made for each plane by selecting single track events in which a single hit is seen on every plane. A straight track incident on the plane in question was fitted, with the plane in question included in the fit. Figure 3.8 shows the residual distributions for plane 3. All residual distributions were seen to be approximately Gaussian.

As discussed in Section 2.8.3, when the plane in question is included in the fit the spread in the residual distribution, σ_r, is given by

$$\sigma_r^2 = \sigma_d^2 - \sigma_f^2 \tag{3.3}$$

where σ_d is the spatial resolution of a plane and σ_f is the uncertainty in the fit position at the plane. Input values for sensor resolutions (all planes assumed equal) were

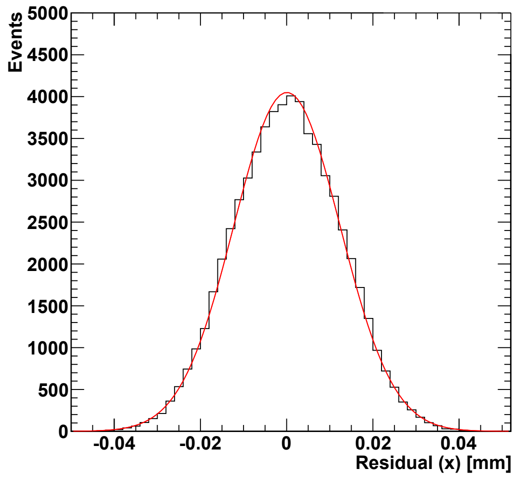

(a)

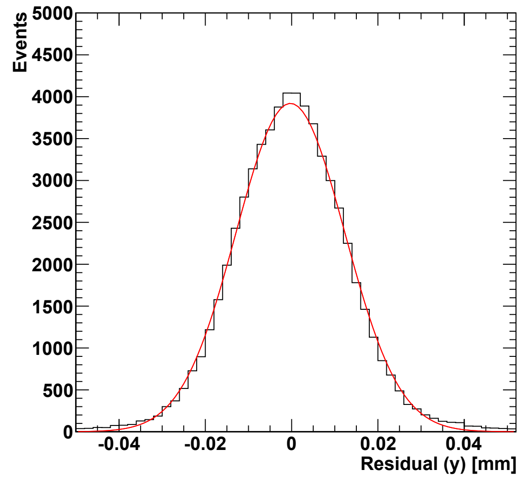

(b)

Figure 3.8: Residual distributions for heavy ions on plane 3. (a) x sensor and (b) y sensor. The fitted hit position, f, comes from a fit to all five planes. A Gaussian fit is overlaid.

Table 3.2: Plane spatial resolutions with heavy ions.

Plane	Sensor	σ_f [μm]	σ_r [μm]	σ_d [μm]
1	x	12.58	1.42	12.66
1	y	12.58	1.40	12.66
2	x	8.20	12.51	14.96
2	y	8.20	12.68	15.10
3	x	8.51	12.04	14.74
3	y	8.51	12.96	15.50
4	x	8.57	12.90	15.49
4	y	8.57	12.28	14.97
5	x	10.13	1.35	10.22
5	y	10.13	1.36	10.22

varied iteratively until the width of the residual distribution satisfied equation 3.3 (as in Section 2.8.3).

Table 3.2 gives fit uncertainties, residual distribution widths and calculated resolutions for all 5 planes. The mean resolution for all sensors is 13.65 ± 0.66 μm. This is significantly worse than the resolution with protons of 6.91 μm, and can be largely attributed to the loss of charge interpolation over neighbouring strips. It is however slightly better than the $p/\sqrt{12} = 17.3$ μm that might have been expected from an effectively binary readout chip. This can be attributed to the fact that odd and even strip clusters are roughly equally probable, meaning that cluster positions are

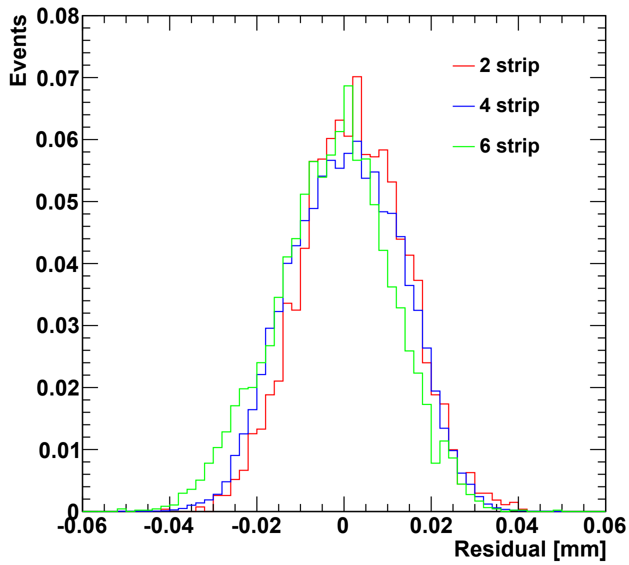

Figure 3.9: Normalised residual distributions for 2, 4, and 6 strip clusters (plane 3, x).

in fact discretised by $p/2 = 30\ \mu$m.

The large cluster widths seen in Figure 3.7 appear not to degrade the spatial resolution, suggesting that the large signals are spread evenly either side of the true hit position so that the cluster mid-point remains a good estimate of the true hit position. Figure 3.9 gives normalised residual distributions for cluster widths of 2, 4 and 6 strips, and shows that each distribution is of approximately the same width.

Asymmetries in the residual distributions are due to the proximity of the beam on the sensor chip boundaries, where truncations of clusters can occur. Small non-Gaussian tails are often seen on residual distributions, such as in Figure 3.8b. Figure 3.10 shows the same distributions plotted as a function of impact position on plane 3. At certain positions the residual distribution is seen to be shifted positively or negatively. These positions correspond to chip boundaries where clusters do not always propagate over a boundary, thus causing a shift in the mid-point of the cluster. With particles incident to the left of a boundary, residuals are negatively shifted, and vice versa. This can be seen in Figure 3.10b, where chip boundaries are at -3.0 mm and $+4.7$ mm (separated by $128 \times 60\ \mu$m). Furthermore, intermediate regions of such behaviour are seen as a result of the same effect in other planes. For example plane

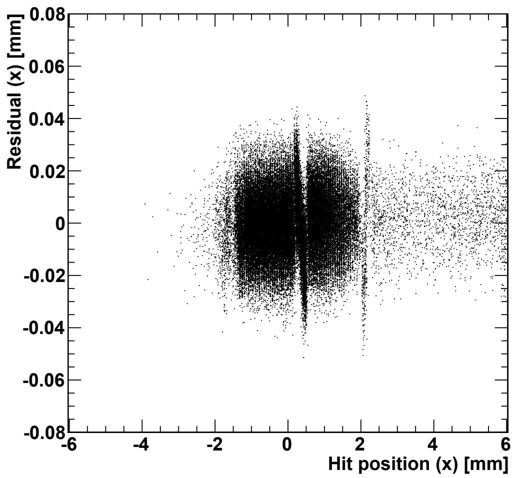

(a)

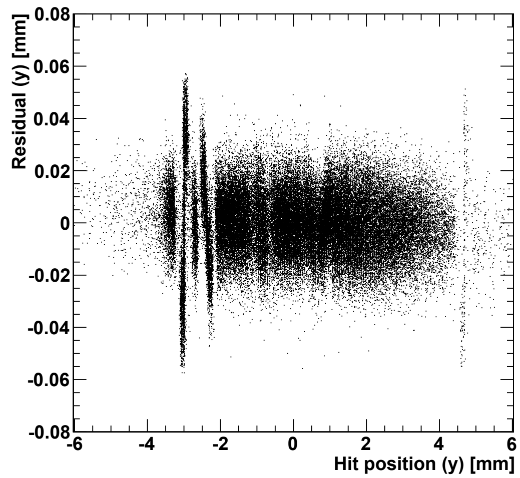

(b)

Figure 3.10: Plane 3 residual distributions as a function of plane 3 hit position. (a) x sensor and (b) y sensor.

2 has a chip boundary at $y = -2.4$ mm. This affects the fit position at plane 3, rather than the hit position, so the sign of the shift in residuals is reversed.

3.6.2 Angular resolution

The resolution of the measurement of deflection angle is calculated in the same way as in Section 2.8.4. With straight tracks where no crystal is present, the deflection angle is known to be zero. The bent track fit is used to determine the spread in measured deflection angles around zero, thus giving the resolution of a deflection measurement. Figure 3.11 shows the distribution of bent tracks for both x and y. The distributions are approximately Gaussian, with standard deviations of 6.75 μrad and 6.67 μrad, in x and y respectively. This compares with 10.2 μrad, predicted by the bent track covariance matrix. The overestimation from the covariance matrix is likely to result from an overestimation in the scattering angle; assuming perfect resolution and optimum spacing of telescope planes (ie very close to the crystal with long arm length), the angular resolution would be limited to $\sqrt{2}\langle\theta_{\text{scat}}\rangle = 8.11$ μrad. The measured values compare with 5.2 μrad in x and y as measured by the telescope when used with 400 GeV protons.

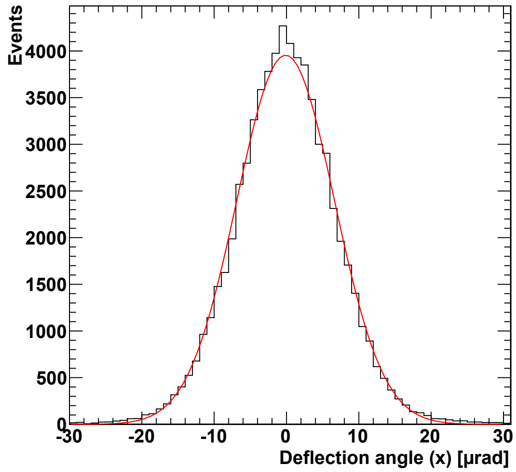

(a)

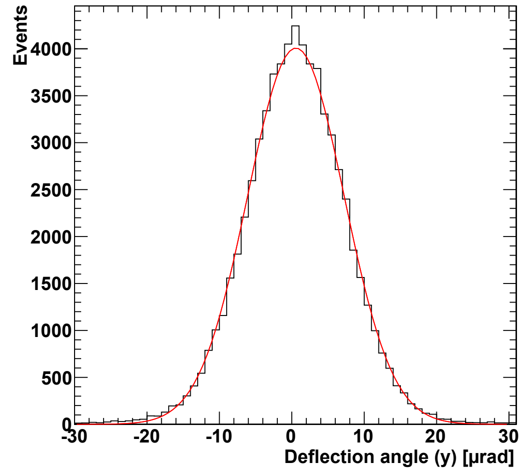

(b)

Figure 3.11: Distribution of measured ion deflection angles ($\Delta\theta = \theta_2 - \theta_1$) for straight tracks using the bent track fit, in (a) x and (b) y.

Table 3.3: Comparison of telescope deflection resolution, $\sigma_{\Delta\theta}$, incident angle resolution, σ_{θ_1}, expected scatter angle, $\langle\theta_{\mathrm{scat}}\rangle$, and channeling critical angle, θ_{crit} for protons and lead ions.

		400 GeV p	63.1 A GeV Pb^{82+}
$\sigma_{\Delta\theta}$	[μrad]	5.2	6.7
σ_{θ_1}	[μrad]	2.5	5.8
$\langle\theta_{\mathrm{scat}}\rangle$	[μrad]	2.4	5.7
θ_{crit}	[μrad]	10.0	10.0

The measurement of the incident angle is required for selection cuts of particles incident within the channeling acceptance angular range Without knowing the true incident angle, the resolution of its measurement can only be estimated from the covariance matrix (equation 2.29). Assuming sensor spatial resolutions of 13.7 μm and a scatter angle of 5.74 μrad, this approach gives a resolution on the incident angle of 5.8 μrad, which compares with 2.5 μrad for 400 GeV protons. The critical channeling angle for 63.1A GeV ions of $Z/A \sim 0.394$ in silicon crystals is $\sim$10.0 μrad (from equation 3.1), and for smaller nuclei with $Z/A \sim 0.5$, such as carbon, the critical angle is $\sim$11.1 μrad. This shows that the telescope has sufficient deflection resolution and incident angle resolution to be able to measure crystal channeling in a 63.1A GeV heavy ion beam, and provides adequate selection cuts on incident particle angles. Table 3.3 compares the relevant values for proton and ion beams.

3.7 Telescope observations

3.7.1 Beam characteristics

The telescope can be used to determine beam parameters such as the width and the angular divergence, using data from runs in which no crystal is present in the beamline. Tracks are reconstructed in the crystal region, incident on plane 3, using the straight track fitting procedure described in Section 2.7.3.

Figure 3.12 shows beam profiles as reconstructed from plane 3, for both x and y. The RMS beam width in x, excluding tails is $\sim$1 mm. The constant background tail that is seen for positive x is a common feature, and corresponds to the upstream beam scrapers not being in place. The beam is wider in y, with an RMS width of $\sim$2 mm. Discontinuities are seen at $y = -3.0$ mm and $y = 4.7$ mm, consistent with that seen in Figure 3.10. The beam in x is concentrated largely in a region of the sensor corresponding to a single APV25 chip, and only a small discontinuity is seen in x, at 2.2 mm. Beam profiles from all five planes are consistent. The beam is large compared to the width of a strip crystal, meaning that a large number of events would be rejected from any offline selection cuts that require a particle to be incident on the crystal. For a strip crystal of width 1 mm in the centre of the beam spot in x, 31% of events would be accepted. Clearly for vertical strip crystals it is more beneficial to statistics to have a beam that is narrow in x than in y.

Figure 3.13 shows the angular distribution of straight tracks in x and y. The RMS of both distributions between ± 100 μrad is $\sim$31 μrad, and provides a measure of the beam divergence. The angular resolution for straight tracks in the crystal region (incident on plane 3) is estimated from 2.26 to be 4.58 μrad, which when subtracted in quadrature from the RMS of each distribution leaves a beam divergence of $\sim$31 μrad in both x and y. This is large compared to the channeling acceptance angle of $\sim$10 μrad, meaning that a high proportion of particles incident on a well aligned crystal would not be channeled. Selection cuts on the incident angle would effectively reduce the divergence, though this would be at the cost of statistics. In the examples in Figure 3.13, a selection cut of ± 10 μrad would reject 78% and 76%

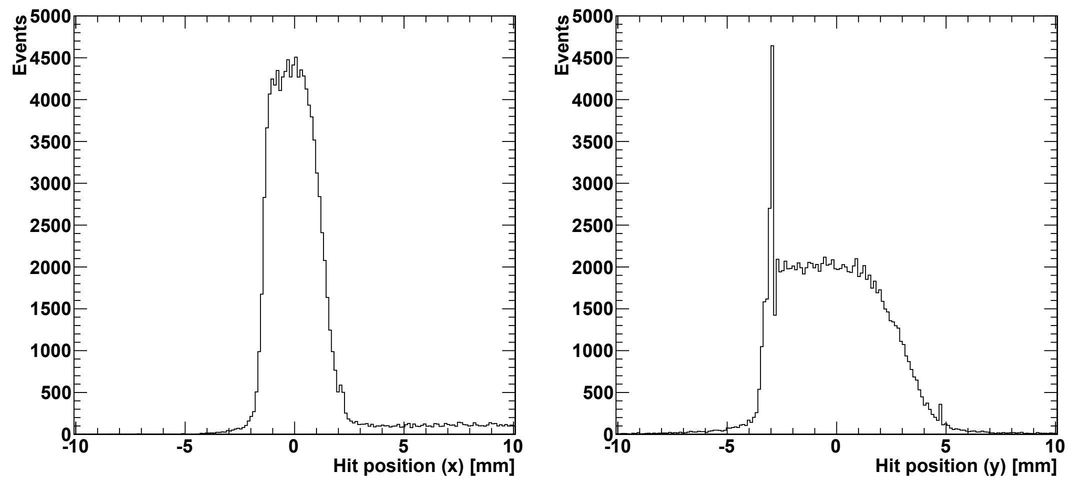

(a) (b)

Figure 3.12: Beam profiles as measured by Plane 3. (a) x and (b) y.

of all events, in x and y respectively. For this reason a low divergence beam is of great advantage.

3.7.2 Quadrupole magnet

During an early run in the test beam it was noted that the measured deflection angle, $\Delta\theta$, for straight tracks had a much wider spread than expected. Values of $\sigma_{\Delta\theta} = 65\ \mu$rad and $\sigma_{\Delta\theta} = 78\ \mu$rad were seen in x and y respectively; an order of magnitude greater than expected (see Section 3.6.2). Figure 3.14 shows the deflection angle as a function of the x-y position of the incoming particle, and shows a strong linear dependence. This dependence would not be expected with straight tracks through the telescope, so an explanation was needed. Various hardware and software issues were excluded, suggesting that the effect may be a real physical effect. Figure 3.14 shows that particles are deflected in x such as to focus them, and in y such as to defocus them; an effect consistent with that of a focussing quadrupole magnet. Such a magnet (Q14 quadrupole) was in place in between planes 1 and 2, and was supposed not to be operating throughout the experiment. It was found that the quadrupole magnet had in fact been operating during this run, thus explaining the large angular deflection measurements. The magnet was subsequently disabled for the remaining duration of the test beam.

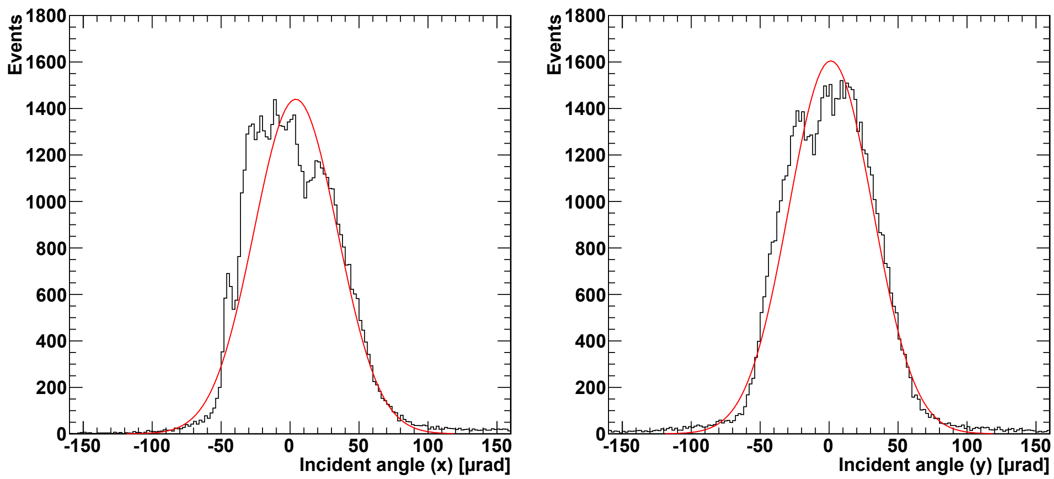

(a) (b)

Figure 3.13: Distribution of angles of straight tracks, reconstructed as incident on plane 3, for (a) x and (b) y. The spread of the distributions provides a measure of the beam divergence.

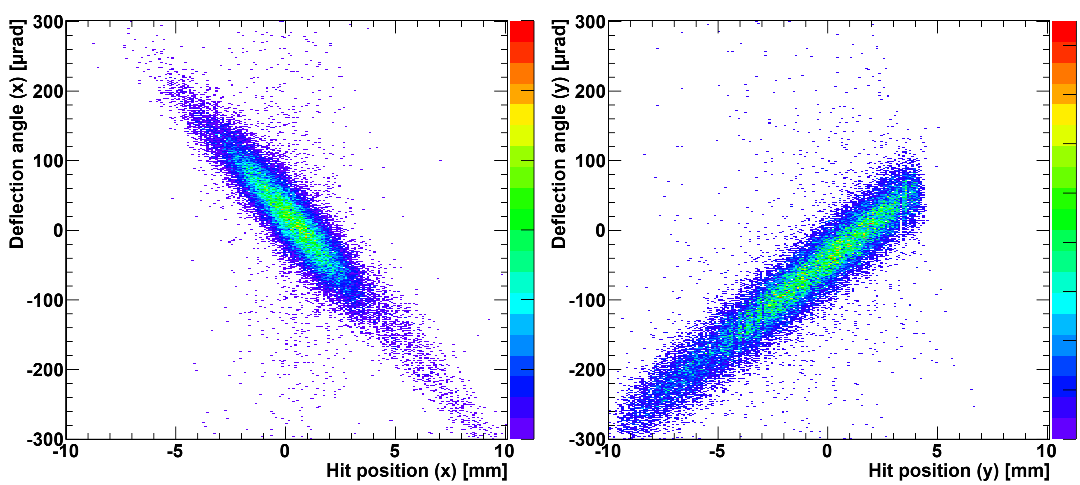

(a) (b)

Figure 3.14: Number of events versus deflection angle, $\Delta\theta = \theta_2 - \theta_1$, and reconstructed impact parameter at $z = 0$. (a) x and (b) y.

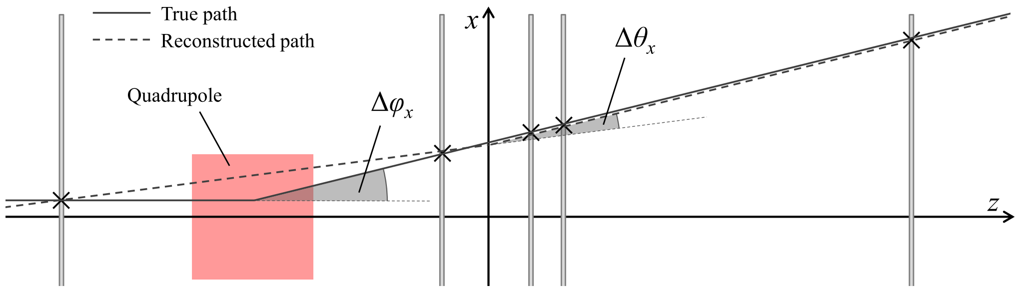

Figure 3.15: Measurement of deflection from the quadrupole magnet. With the magnet approximately half way between planes 1 and 2, the reconstructed deflection angle, $\Delta\theta_x$, is roughly half of the true deflection angle, $\Delta\phi_x$.

Figure 3.14 can be used to estimate the field gradient within the quadrupole magnet. By equating the Lorentz force with the required centripetal force, for a quadrupole of length l, the deflection in x due to the quadrupole, $\Delta\phi_x$, is given by

$$\Delta\phi_x = B_y\, l\, \frac{Z|e|}{Ap} \tag{3.4}$$

where B_y is the vertical magnetic field at a certain position within the quadrupole, and $Z|e|$ and Ap are the charge and momentum of the incoming particle respectively. The Q14 quadrupole is approximately half way between planes 1 and 2, and simple geometric considerations show that $\Delta\phi_x \approx 2\Delta\theta_x$, as seen in Figure 3.15. Substituting these relations into equation 3.4 and rearranging we obtain the following expression,

$$\frac{B_y}{x} = 2\,\frac{\Delta\theta_x}{x}\,\frac{Ap}{Z|e|l}. \tag{3.5}$$

From Figure 3.14 it is seen that the measured deflection in x, $\Delta\theta_x$, varies with x according to $\Delta\theta_x/x = -36\ \mu\text{rad mm}^{-1}$. Assuming that $l = 3$ m, $p = 63.1$ GeV/c per nucleon and $Z/A = 0.394$, we obtain a field gradient of $\frac{\mathrm{d}B_y}{\mathrm{d}x} = -12.8\ \mathrm{T\,m^{-1}}$. Similarly for y we obtain, $\frac{\mathrm{d}B_y}{\mathrm{d}x} = 12.8\ \mathrm{T\,m^{-1}}$. This estimate is within with the nominal peak gradient of 24 $\mathrm{T\,m^{-1}}$ available from the Q14 quadrupole [107]. In order not to interfere with subsequent runs, care was taken to ensure that the quadrupole was disabled for the remaining duration of the test beam. The observation of the quadrupole magnetic field illustrates the importance of a well understood and monitored telescope. The telescope is not only important for desired measurements such as channeling, but also for verification of the experimental conditions.

Due to complications with crystals and the ion beam it was not possible to make crystal channeling measurements. The measurements that were made did however demonstrate that channeling measurements would be possible with heavy ion beams in the future.

3.8 Summary

The tracking telescope was exposed to $31.5A$ GeV/c and $63.1A$ GeV/c ion beams of various species of $Z/A = 0.394$. The telescope modules each exhibited the characteristic raw data output associated with the saturation of the APV25 chip under exposure to HIP events.

It was possible to reconstruct hits from each module, by effectively using the APV25 as a binary chip; any strips with signals above a certain threshold over the chip's median value were included in a cluster. Hit finding efficiency was high, averaging 99.8% per plane. The hit reconstruction algorithm did have the disadvantage of not registering MIP events that may occur as a result of nuclear interactions between an ion and the crystal. The study of nuclear interactions would require the algorithm to be modified such that events containing both HIPs and MIPs could be reconstructed.

The mean spatial resolution for all planes was found to be 13.65 ± 0.66 μm; worse than that when used with a 400 GeV proton beam, but better than expected from pitch/$\sqrt{12}$. Discontinuities in the hit position were seen, as a result of poor clustering at interchip boundaries resulting from only one of the adjacent chips saturating, and only around half of the corresponding cluster being reconstructed. One way of suppressing these discontinuities would be by iteratively positioning each module such that the beam is focussed on a region of the strip corresponding to a single

APV25, restricting the discontinuities to the low statistic tails of the beam. Alternatively a positional shift in all clusters near to a chip boundary could be performed as part of the reconstruction software.

The angular resolution was shown to be 6.7 μrad for the deflection, and 5.8 μrad for the incident angle. This is slightly worse than that seen with 400 GeV protons, but sufficiently good to study crystal channeling of heavy ions, for which a critical angle of 10.0 μrad is seen for 63.1 A GeV lead ions.

The ion beam was observed to have an RMS width of $\sim$1 mm and $\sim$2 mm in x and y respectively, and to have a divergence of 31 μrad x and y. These are large compared to a typical crystal width of $\sim$1 mm and angular acceptance for channeling of 10 μrad. Under these conditions a cut on x position for a 1 mm crystal, and on incident angle of $\pm$10 μrad would discard $\sim$93% of the collected data. The measurement of a quadrupole magnetic field within the telescope demonstrated the capability of the telescope to monitor beam conditions as well as making the desired measurements of channeling phenomena.

No channeling measurements were made due to technical problems with crystals and the ion beam, as well as time constraints. However the performance of the telescope showed that good measurements of channeling phenomena would be possible in the future.

Chapter 4

Design and performance of the CMS Binary Chip

The CMS Binary Chip is the proposed readout chip for silicon microstrips in the CMS Tracker at the HL-LHC. The chip has been tested in the 400 GeV H8 proton beamline with the telescope described in Chapter 2. This chapter first discusses the motivation for the chip, and provides an overview of its design. The performance of the chip in the proton beam is then discussed.

4.1 Introduction

The order of magnitude increase in luminosity at the HL-LHC has the principal aim of increasing statistics in order to extend the physics reach of the LHC. In order to keep occupancies sufficiently low in the high luminosity environment, the replacement Tracker must have higher granularity. A greater number of strips will therefore be required in the Tracker, leading to a risk of increased power consumption, and hence cooling requirements and material. In addition, the Level-1 Trigger rate must remain below 100 kHz in order to maintain compatibility with existing systems, and will for the first time require information from the Tracker.

The current readout of silicon strips, performed by the APV25, involves analogue pulse height information being available off-detector. Manageable data rates mean that a simple unsparsified architecture can be used, which keeps the data rate constant and allows the Tracker to remain fully synchronised. The current system has performed well, but cannot be translated to the HL-LHC. Off-detector digital links will be used, which would require digitisation of front-end pulse height information and a very complicated chip with increased power consumption. Furthermore, sparsification would be required in order to keep data volumes manageable.

The implementation of a binary, unsparsified readout architecture has therefore been proposed, which will maintain chip and system simplicity, at the cost of pulse height information. The CMS Binary Chip (CBC) is a prototype of such a readout chip, and is the subject of this chapter.

Further iterations of the CBC are planned, which will make use of simple on-chip logic to identify high p_{T} candidates, known as stubs, as part of the Level-1 Trigger [108]. One way of discriminating between high and low p_{T} tracks uses the fact that high p_{T} tracks have less curvature in the r-ϕ plane and would thus pass barrel sensor layers at larger incidence angles, leading to smaller clusters. Cluster width would therefore provide some discrimination between high and low p_{T} tracks. Another way of identifying stubs is the stacked module approach, involving the use of two closely separated sensor layers on a single chip, where on-chip logic isolates tracks in which there is coincidence between hits on each of the sensor layers. The extra features of the next iteration of the chip, the CBC2, will be discussed later in Section 4.5.

4.2 Design and measured performance

4.2.1 Overview and specification

The CBC is a 128 channel wire-bonded chip fabricated in 130 nm CMOS. The front-end input pads are staggered in two rows, with an effective pitch of 50 μm. All peripheral pads are on a pitch of 150 μm. The inputs feed the front-end amplifier and comparator stages, and the comparator outputs are sampled into a pipeline memory at 40 MHz. The pipeline has a programmable pipeline depth of 256, corresponding to a trigger latency of up to 6.4 μs. Upon a trigger, the 128 bits of data stored in the pipeline a latency period earlier are retrieved and stored in the readout buffer, which can accommodate up to 32 events. This is sufficiently large to cope with the random arrival of trigger signals.

Radiation tolerance is a significant concern, and critical control blocks have been designed for SEU tolerance. Fast interface signals are used for the 40 MHz clock, output data and trigger inputs, and are implemented using the Scaleable Low Voltage Signalling (SLVS) standard [109]. Slow control interfaces are used to configure the currents and voltages required by the front-end stages, and are programmed via I^2C.

The use of existing cables at the HL-LHC will impose limits on the deliverable current, and so power consumption is a major consideration. A target of $<500\ \mu$W per channel has been imposed, compared with 2.6 mW for the APV25 (with long strips). A noise target of <1000 RMS electrons has also been imposed.

Each input pad is wire-bonded to a sensor strip and charge collected in the strip is read out by a preamplifier. Charge is integrated onto a feedback capacitor and discharged by a resistive feedback network, which is configurable for either polarity. The pulse is amplified by a capacitive gain post amplifier. A comparator then detects signals over a globally configurable threshold, and produces a digital output accordingly. Figure 4.1 shows the CBC layout.

4.2.2 Front-end circuitry

The CBC front-end circuit consists of the preamplifier, postamplifier and comparator. Figure 4.2 shows a schematic diagram of the front-end circuitry of each CBC channel.

The preamplifier includes a 100 fF feedback capacitor and a resistive feedback network, and is designed to be coupled to sensors of either polarity. The resistive feedback depends on the polarity of the sensors; with n-in-p type sensors, electrons flow into the preamplifier and the switch network selects electrons mode in which only the 200 kΩ feedback resistor is used. With p-in-n type sensors, holes flow and

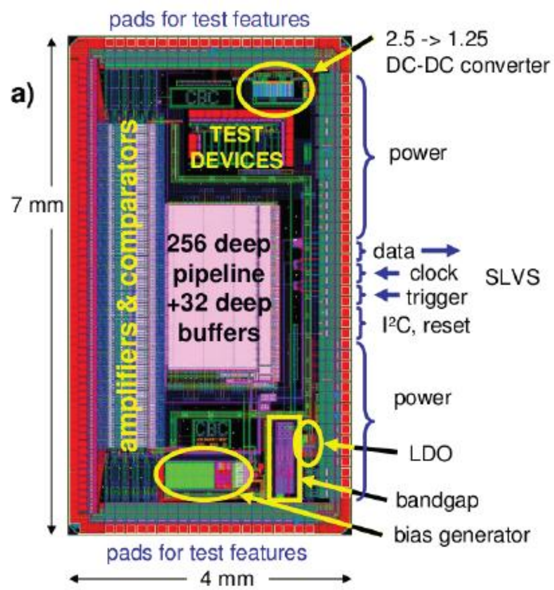

Figure 4.1: CBC layout with main interfaces labelled [43].

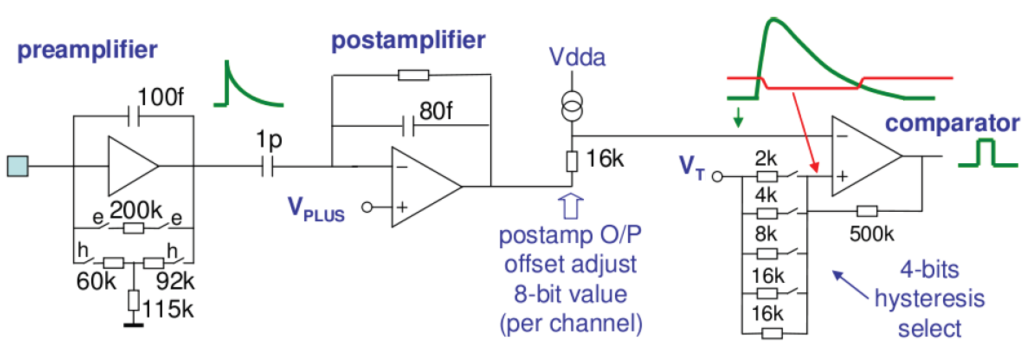

Figure 4.2: CBC front-end circuitry. Shown are the preamplifier and postamplifier which provide the pulse shaping, and the comparator which provides the binary output [43]. Additionally, there is a polarity select circuit at the output of the comparator, which ensures that an output signal is logic 1 regardless of whether operation is in electrons or holes mode.

the resistive T-network is used. For both electrons and holes mode the signal at the preamplifier output has a decay time of approximately 20 ns, which is sufficiently small to help avoid pileup [43].

The postamplifier is implemented by an operational amplifier, and is AC coupled to the output of the preamplifier in order to remove any DC component due to leakage current. The bias voltage, V_{PLUS}, is common to all channels on the chip. The postamplifier output pulse shape has a peaking time of approximately 20 ns [43].

The comparator comprises a 2-stage differential architecture, with the differential and logic stages powered from the analogue and digital domains respectively. The polarity of the output is configurable depending on whether electrons or holes are being read out, such that the output is always a logic 1 for a signal. A global programable threshold, V_{T}, is fed to all comparators. Each channel has an 8-bit programmable current source which produces a DC offset at the comparator input, allowing correction for any variation in V_{T} between channels. The comparators include a globally programmable resistive hysteresis network, controlled by a 4-bit register. This lowers V_{T} while the comparator output is at logic 1, thereby preventing rapid oscillation in the comparator output due to noise fluctuations in the input signal.

The comparator has a different response time depending on the size of the input signal, and this is mostly dependent on the rise time of the input signal and the gain of the amplifier. The timewalk is defined as the difference in timing of the comparator output for signals of 1.25 fC and 10 fC, with a comparator threshold of 1 fC (see Figure 4.5). It is required that the timewalk be less than 16 ns in order to ensure that hits are associated with the correct bunch crossing (based on the ATLAS ABCD3T specification [110]).

4.2.3 Digital logic

Figure 4.3 shows the flow of data through the CBC. The output from each comparator is processed by the *Hit Detection Logic*, and the *Pipeline Control Logic* controls

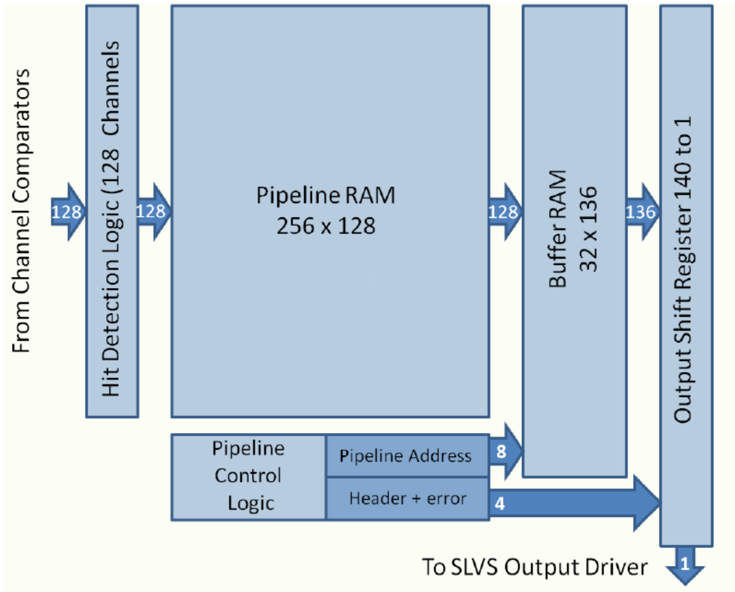

Figure 4.3: Data flow through the CBC [111].

which events are written to the Buffer RAM. Data are finally serialised by the *Output Shift Register* before being transmitted off the chip.

The hit detection logic is required to synchronise the raw comparator output to the clock. There are two operational modes that can be selected; *variable* and *single*. Variable mode produces a synchronised version of the comparator output, whereby the output signal that is sampled to the pipeline is 1 for as long as the comparator output is 1. Single mode samples a signal to the pipeline that lasts just one clock cycle by detecting the rising edge of the comparator signal, regardless of the length of the comparator signal. Variable mode has the advantage over single mode of a variable output pulse length, which could in principle be used to give information on pulse size. The extended pulse could however lead to overlapping of the output signals of consecutive pulses at high trigger rates. Additionally, efficiency with variable mode could suffer if an input pulse does not exceed V_{T} for enough time to be synchronised to the clock, causing the hit to be missed.

The Pipeline Control Logic is responsible for sequencing the writing of data from the Hit Detection circuit into the Pipeline RAM, and the transfer of data from the Pipeline RAM to the Buffer RAM following a trigger signal. The pipeline has a depth of 256 bits, corresponding to 6.4 μs latency at 40 MHz. The buffer has a

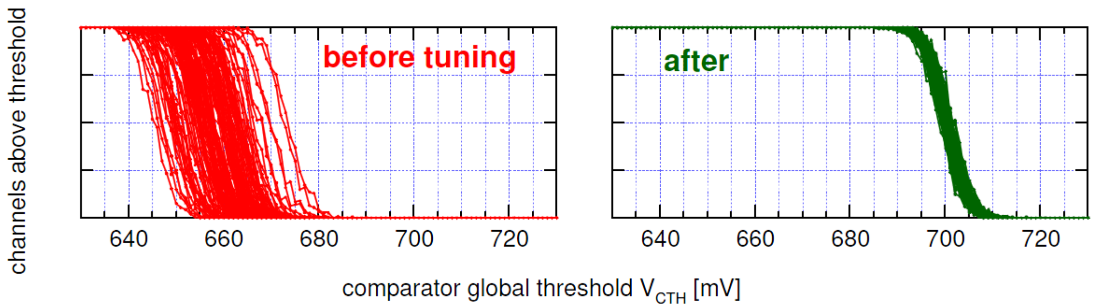

Figure 4.4: Comparator threshold uniformity, before and after individual channel tuning.

depth of 32 bits, and a width of 136 bits to accommodate 128 channel bits and an 8-bit pipeline address. Data are stored in the buffer, awaiting readout into the Output Shift Register. Finally 140 bits are transferred off-chip, which include a 2-bit header and a 2-bit error. The error bits are used to indicate two possible operational problems; one error bit indicates a discrepancy in the latency between the pipeline read and trigger pointers, and the other indicates that the buffer is full [111].

Fast control is provided via the trigger input. Slow control is provided via I^2C architecture, and is the interface between the external system and the control register that configures the CBC for operation.

4.2.4 Front-end performance

Figure 4.4 shows S-curves measurements for all 128 channels on a chip and illustrates the variation in comparator thresholds across channels, before and after the individual channel tuning process. Before channel tuning the full spread is approximately 30 mV, whereas following tuning it is at the mV level. For a front-end gain of 50 mV/fC, a 1 mV residual dispersion in the offset after tuning corresponds to around 125 electrons, which is small compared to the noise target of 1000 electrons. The tuning is limited by the resolution on the digital-to-analogue conversion that sets the comparator threshold level.

Figure 4.5 shows the comparator response time measurements as a function of charge injection. This was done for a variety of preamplifier input capacitances, to simulate

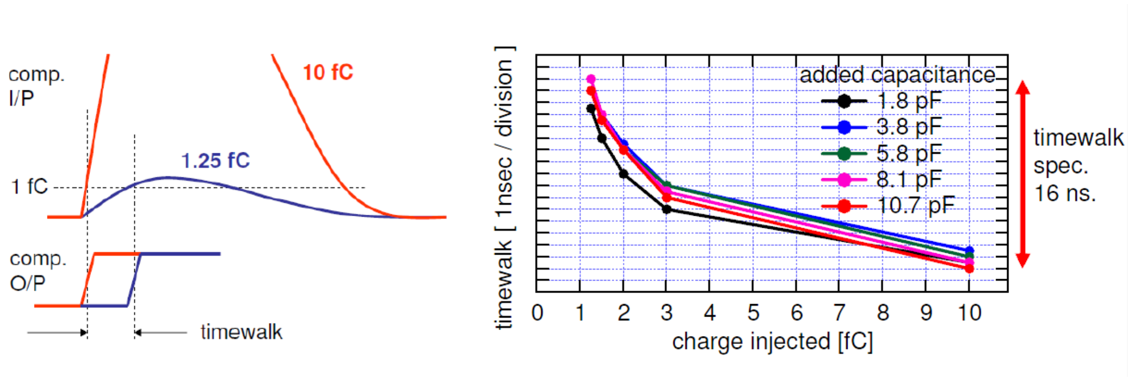

Figure 4.5: Left: Definition of comparator timewalk. Right: Timewalk measurements.

the effect of different strip sensors. The pulse rise time is proportional to the input capacitance and inversely proportional to the current in the input transistor, so to maintain the puse shape rise time it was necessary to complement any increase in input capacitance with a corresponding decrease in the input transistor current. This allows a measure of the timewalk, which is seen to be just within the specification of 16 ns, and shows no significant degredation with input capacitance. This confirms that the timewalk can be kept constant by varying the urrent in the input transistor appropriately.

The gain of the analogue electronics can be determined by measuring the output voltage as a function of injected charge. Output voltage for a given amount of injected charge is estimated from S-curves, generated by sweeping the comparator threshold from a region where the comparator always fires to a region where it never fires. Figure 4.6 shows an example set of S-curves measured for all 128 channels at three injected signals in the 1.5-3.1 fC range. The CBC was operated in electrons polarity mode, but the response is similar for holes mode. Data are fitted with a complementary Gaussian error function, and the mid-point of each S-curve provides a measurement of the output voltage. The gain represents the linear relation between the S-curve mid-point and the injected charge. Also shown in Figure 4.6 is the S-curve mid-point level for all 128 channels. The extrapolated pedestal value is estimated as 488.9 mV, and the gain is estimated to be 46.9 mV fC^{-1}. The response has been shown to be linear up to around 8 fC, but the linearity is important only in the region of operation of the comparator, with a threshold of around 1 fC.

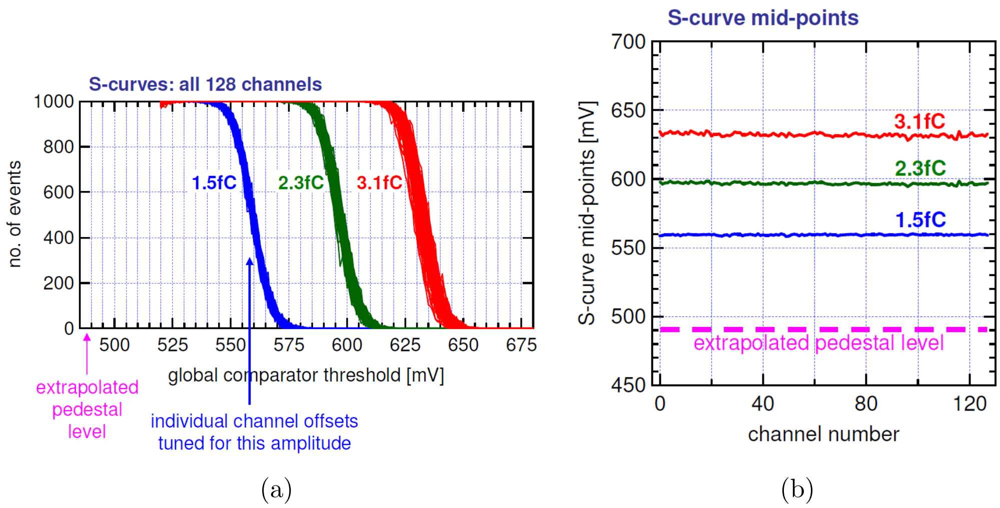

Figure 4.6: (a) S-curves for all channels after tuning, for various charge injections. (b) S-curve mid-points for all channels at the various charge injections. From this the pedestal value and gain can be estimated.

4.2.5 Power and noise

A DC-DC power scheme has been adopted, where higher voltages are translated to the lower voltages required for the on-detector electronics. An on-board switched-capacitor DC-DC converter is included on each CBC, and converts the 2.5 V supply to the 1.25 V supply required by the core circuitry. A low dropout (LDO) voltage regulator is included on the CBC, which takes the 1.25 V supply as the input and provides a stable output for the analogue circuitry. The increase in preamplifier output rise time with increased external capacitance is compensated for by increasing the current in the input device. For this reason the analogue power increases with capacitance, as seen in Figure 4.7. The analogue power measurements are seen to be close to simulation expectations, and consistent for both electrons and holes modes. The analogue power per channel (μW) can be approximated by $120 + 21\,C/\text{pF}$, and the digital power per channel has been measured to be less than 50 μW. So for a mid-range sensor strip capacitance of 5 pF, a power consumption of less than 300 μW per channel is achievable; well under the 500 μW target [43].

Electronic noise also has a dependence on the external capacitance added at the preamplifier input, and is also seen in Figure 4.7. Noise is determined from S-curve measurements, as the standard deviation of the S-curve error function. Again, the

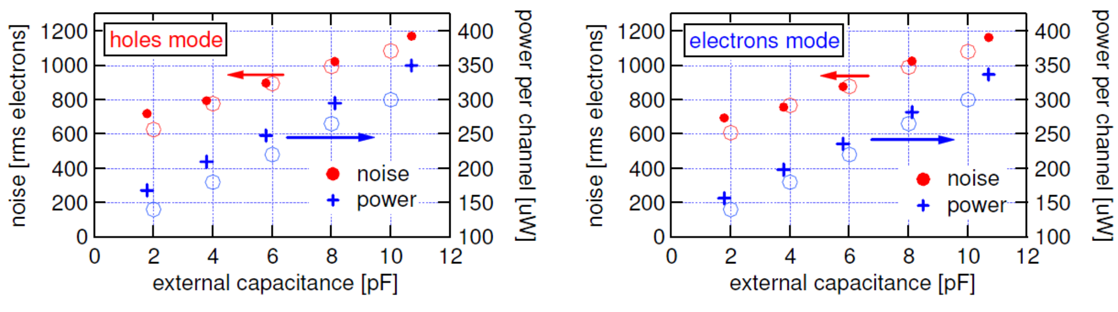

Figure 4.7: Noise and analogue power for holes and electrons mode (circles are simulations). There is no significant difference between electrons and holes mode [43].

performance is approximately the same for electrons and holes modes. For a typical sensor capacitance of 5 pF, a noise performance of approximately 820 electrons is achievable; within the target of 1000 electrons.

4.3 Beam test studies

Beam tests of CBC modules have been carried out in conjunction with the UA9 tests, in the 400 GeV proton H8 beamline. The aims of the tests were to evaluate the performance of a CBC module in the presence of a well characterised beam, in particular the consequences of its binary readout. The precise measurements of particle trajectories provided by the telescope means that it can provide a good platform on which to test the CBC. In this section data collected from beam tests in September 2011 and October 2012 are analysed.

A CBC module was constructed for each of the two beam tests. Each module was integrated into the telescope as an extra plane, just downstream of the last telescope plane. This allowed the CBC module to operate parasitically, thus not interfering with the UA9 test. The modules and their integration into the telescope are discussed in the following sections.

4.3.1 CBC modules

A separate CBC module was made for each of the 2011 and 2012 beam tests. Sensors were mounted on Printed Circuit Boards (PCBs) and wire-bonded to the CBC.

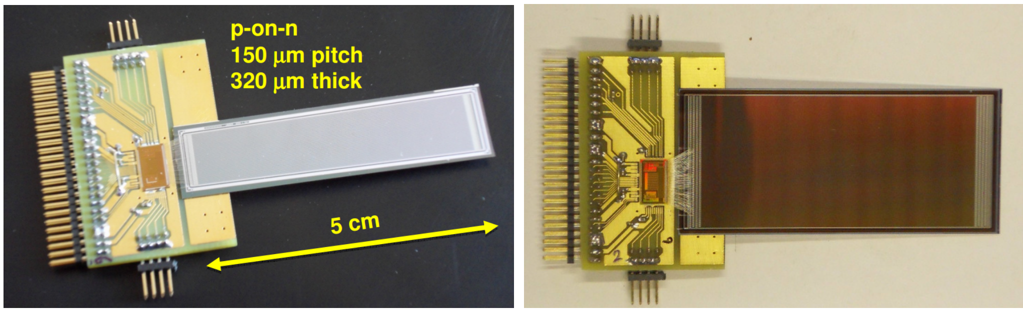

(a) (b)

Figure 4.8: CBC sensors mounted on test boards. (a) Hamamatsu sensor (2011), (b) Infineon sensor (2012).

Table 4.1: Sensor descriptions.

		Hamamatsu, 2011	Infineon, 2012
Number of strips		64	256
Pitch	[μm]	120-150 (fan shaped)	80
Active width	[mm]	7.68-9.60	20.48
Length	[mm]	50	50
Thickness	[μm]	320	300
Capacitance	[pf]	$\sim$5	$\sim$5

Details of the sensors used in each of the CBC modules are given in Table 4.1. As the Hamamatsu sensor had just 64 strips, only alternate CBC channels were bonded. With the Infineon sensor, all CBC channels were bonded to 128 strips away from the edge of the sensor. Figure 4.8 shows photographs of both sensors mounted on the test boards. Modules were housed in aluminium boxes similar to those used in the telescope (Section 2.5.5). Module improvements made for 2012 were a more mechanically stable box, and the inclusion of a temperature regulating Peltier device that maintained the CBC at a temperature of 20°C. Furthermore, the Infineon sensors used in 2012 give a better approximation to those proposed for future 2S-Pt modules to be used in the CMS Tracker (see Section 4.5).

4.3.2 Integration of CBC module with telescope

The CBC module is placed downstream of the telescope, close to plane 5 (several cm away). Figure 4.9 shows a CBC module in position. Strip sensors are positioned vertically (parallel to y) by convention.

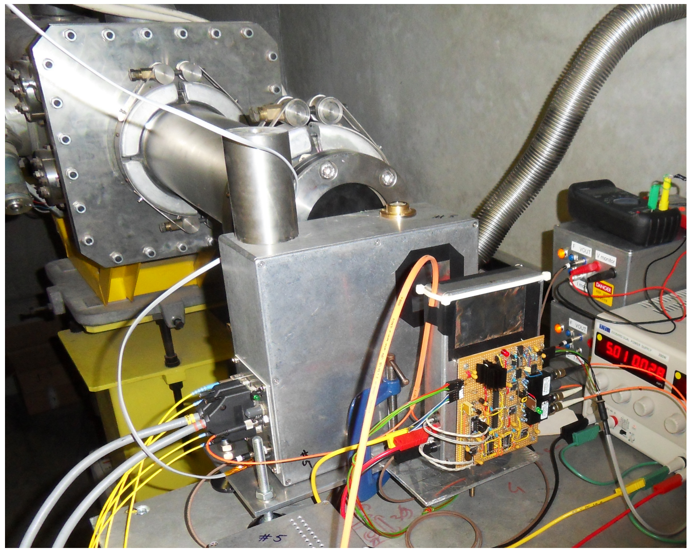

Figure 4.9: CBC module (Hamamatsu sensor) in position just downstream of the fifth telescope module. The beam pipe is seen in the background.

To accept data from the CBC module, the telescope DAQ has been modified from that described in Section 2.6. Figure 4.10 is a schematic diagram of the combined telescope and CBC module DAQ. Changes to the DAQ include an increase of the peak rate to 50 kHz following improvements to the event buffering in the online software. The trigger controller and sequencer boards were replaced with the CiDAQ; an FPGA based VME DAQ card that is essentially a reconfigured APV Emulator (APVe). The APVe is designed to simulate the APV25 buffers and determine their occupancy within 50 ns of each Level-1 trigger, and is used in the CMS counting room to warn the TCS of overflows with negligible transmission time, as well as to monitor synchronisation of the Tracker [112]. The CiDAQ receives triggers, performs fast control of the telescope planes and CBC module, and reads out signals from the CBC module.

Triggers are received from the same scintillators as the telescope. The CiDAQ throttles the trigger based on the buffer occupancies of the APV25 chips in the telescope according to the APV emulation, and the DAQ status from the FED. On receipt of a trigger, data are shifted out of the CBC at 40 MHz, and are transmitted optically to the CiDAQ in the counting room. The CIDAQ also provides a trigger timestamp. In 2011 each bunch crossing time period was divided into four time bins of 6.25 ns width. In 2012 this was improved to eight time bins of 3.125 ns

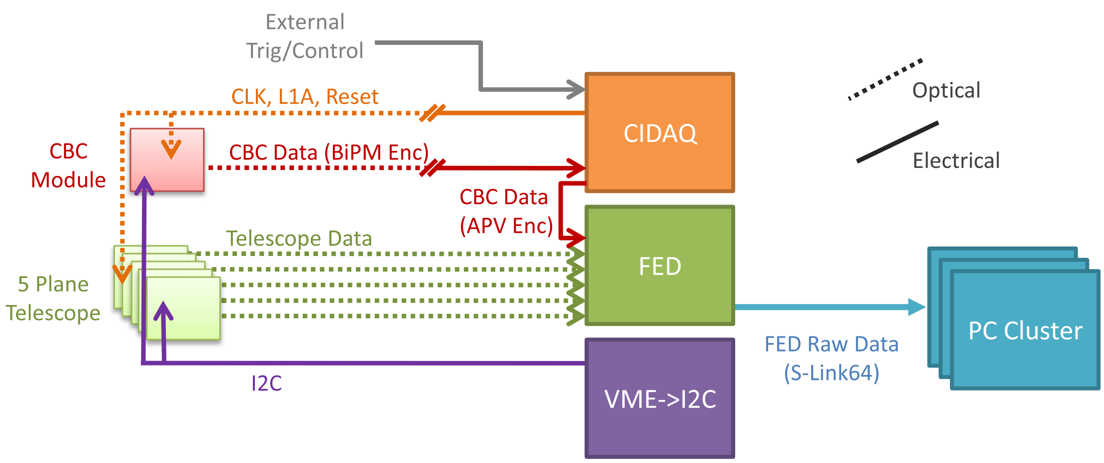

Figure 4.10: Integration of CBC module into the telescope DAQ.

width. Due to the length of cable between CiDAQ and CBC, it takes a finite time for trigger signals from the scintillators to arrive at the CiDAQ, and for the L1A signal to return to the CBC module. To account for this delay, a latency period of an integer number of clock cycles must be applied. The latency period is chosen as the number of clock cycles such that the CBC trigger timeslot best coincides with the peak of the signal pulse shape.

The CBC data stream is encoded on-module using a biphase mark encoding scheme, which is based on differential encoding in which the presence or absence of a transition is used to indicate a logical 1 or 0. The regularly changing polarity helps to maintain good synchronisation, and also provides DC balancing for the optical link. The CiDAQ decodes and buffers the CBC data before it is retransmitted to the FED, and synchronised with the APV25 data arriving from the telescope. In order to maintain compatibility with the telescope, the CiDAQ encodes the CBC frames as APV25 frames. In this way, CBC data are event synchronised with the telescope and propagate through the CMS-based online framework. Events can then be accessed online for monitoring and selection before storage to disk.

4.3.3 Selection cuts

Only a subset of all data collected by the DAQ is useful, and so the first step in the analysis is the selection of the event sample. It is necessary to select events that are both unambiguous and incident on the CBC sensor. The following selection cuts were made:

- Single track. To avoid ambiguity from multiple track events, only those with a single track in the downstream arm of the telescope were considered (with one and only one hit on each of the downstream planes). Events with no reconstructed telescope track are also excluded. This selection cut rejects $\sim$40% of events.

- Track incident on sensor. An x position cut is applied such that all tracks (as measured by the telescope) must be incident on the active region of the CBC sensor, and not less than 0.2 mm from the outermost bonded strip. This cut rejects a further $\sim$20% of events.

- Vertical cut. All tracks must be incident within 3 mm vertically of the nominal beam position. This reduces the effect of any small angular misalignment, and where a fan shaped sensor is used it ensures that the strip pitch is sufficiently constant. This cut rejects a further $\sim$10% of events.

- Time window. This removes all events where the random trigger does not fall within the optimum time bin of the sampling clock, relative to the signal pulse shape. In bunch structured beams, such as that of the LHC, this cut would not be necessary as the non-random trigger timing is adjusted to the phase of the clock. This cut allows an approximation to the bunch structured beam of the LHC. The rejection of events depends on the number of time bins accepted.

The close proximity of the CBC module to the fifth telescope plane, and the low beam divergence meant that no angular cut on tracks was required. Additionally, the good spatial resolution of the telescope compared with the strip pitch of the

CBC sensor allows the impact position on the CBC sensor relative to the periodic strip position to be measured. This allows a cut on interstrip position to be made, thereby allowing the study of any variation across the periodic strip position.

4.4 Results

During the 2011 beam test $>10^7$ events were collected by the CBC, and in the 2012 test $>10^8$ events were collected. The CBC was operated in single mode throughout each test. In each test the CBC was found to operate as expected, and no pipeline or latency errors were seen. Due to the improved module design, better timing resolution and larger data volume, the majority of results presented in this section are from the 2012 test. This will be the case unless otherwise stated.

In the following sections, efficiency will be measured and used frequently. For the case of this analysis, it can be defined as follows,

$$\eta = \frac{\text{Number of events in selection with } \geqslant 1 \text{ hit on the CBC sensor}}{\text{Number of events in selection}} \tag{4.1}$$

4.4.1 Timing measurements

In order to evaluate the performance of the CBC module in an environment similar to that expected during operation in CMS, it is beneficial to select events that fall within a narrow trigger phase window. This allows the sampling time to be optimised with respect to the charge deposition time, as would be the case in the synchronised LHC beam. In order to select the correct time bin to be used for further analysis, it was necessary to study the variation of efficiency with comparator threshold voltage for each time bin.

Figure 4.11a shows how the efficiency varies with comparator threshold voltage for each of the eight time bins (labelled TDC 0-7). The general trend for each time bin shows that with increased comparator threshold the efficiency declines, as a smaller

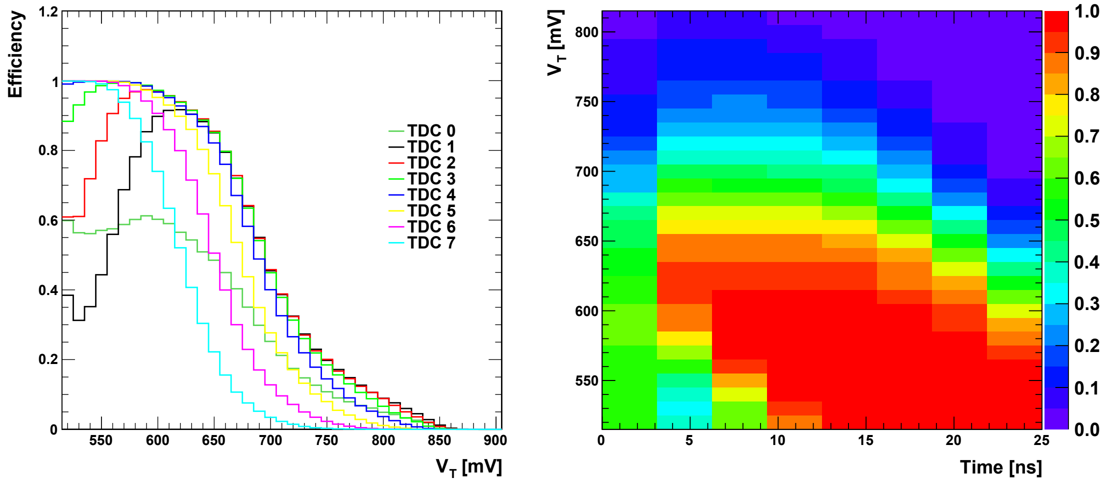

(a) (b)

Figure 4.11: (a) Efficiency as a function of comparator threshold voltage for each of the eight time bins. (b) The same data plotted on a 2-dimensional histogram.

proportion of events deposit sufficient charge to exceed the comparator threshold. Figure 4.11b shows the same data in a single 2-dimensional histogram. It shows more clearly that with the later TDC bins, the fall in efficiency with increased threshold starts at lower thresholds. Also seen is that with earlier TDC bins the efficiency is reduced for lower thresholds. To understand these effects it is necessary to consider the timing of signal pulses with respect to the CiDAQ and CBC trigger timeslots. Due to the clock delay between CiDAQ and CBC, and the fact that the latency period used can only be an integer number of clock cycles, there exists an arbitrary phase shift between the 40 MHz clock as seen by the CiDAQ and CBC. The trigger timeslots for CiDAQ and CBC will therefore in general be out of phase. Figure 4.12 shows the arrival of various pulses within the CiDAQ trigger timeslot. The CiDAQ and CBC trigger timeslots are shown with a phase shift of $\pi/2$.

First we consider the arrival of pulses late within the CiDAQ triggered timeslot, seen in blue. As the peak of the pulse shape occurs beyond the CBC trigger timeslot, smaller pulses can be missed. It is seen that the large pulse fires the comparator within the CBC trigger timeslot, but the small pulse fires the comparator in the subsequent timeslot and is therefore missed. At a high enough threshold, both small and large pulses will be lost, regardless of whether their heights are above the

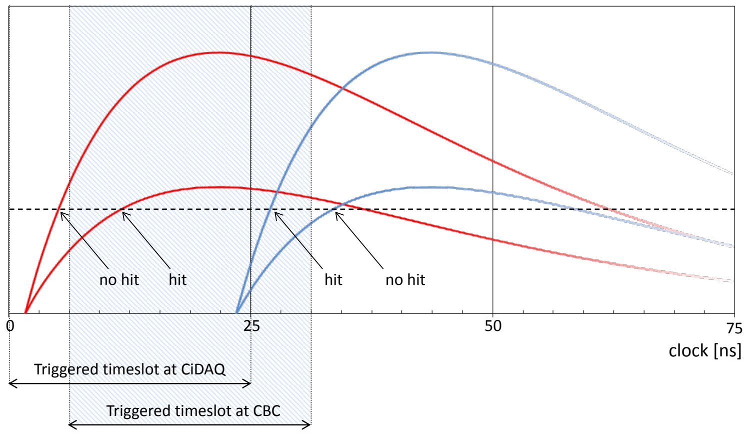

Figure 4.12: Early and late arrival of small and large pulses within the CiDAQ and CBC trigger timeslots. Reduction in efficiency can result when the timeslots are not synchronised.

threshold value. For sufficiently low threshold, both pulses will fire the comparator within the CBC trigger timeslot and will therefore be seen. This explains why the drop in efficiency begins with lower thresholds for pulses arriving late in the CiDAQ trigger timeslot. As the blue pulses move towards the left (representing earlier arriving signals), the drop in efficiency occurs at progressively higher thresholds, according to the pulse shape. This therefore implies that the rising edge of the pulse shape is represented by the rise in efficiency (from right to left) that is seen on Figure 4.11. For example, taking a 50% efficiency contour for the later time bins will represent the reverse of the pulse shape rising edge for a median sized pulse.

Now consider the arrival of early pulses, shown in red. It can be seen that the smaller pulse fires the comparator in the correct CBC trigger timeslot, however the larger pulse fires the comparator in the previous timeslot, and the hit is missed. At a low enough threshold both small and large pulses are lost, and only at sufficiently high thresholds can each pulse be seen. This explains the low efficiency that is seen with early pulses and low thresholds in Figure 4.11.

If the CiDAQ and CBC clocks could be brought into phase such that the two triggered timeslots are also in phase, then there would be no chance of large signals that arrive early being missed. Synchronisation could in principle be achieved by adding lengths of cable to the electronics to add further delay to the clock at the CBC, and then readjusting the latency period accordingly.

Two considerations must be made in the selection of the most appropriate time bin for subsequent analysis. Primarily, the efficiency should be high in the operational threshold region of ∼1 fC (542.8 mV, following calibration in Section 4.4.2). However efficiency should also be high at larger thresholds that correspond to the larger charge deposition events associated with optimum sampling time of the pulse shape. The efficiency is greatest at higher thresholds in time bin 2 (6.250-9.375 ns), however the efficiency drops at lower thresholds. With these considerations, time bin 4 (12.500-15.625 ns) is selected for subsequent analyses, as it has high efficiency at low thresholds, but maintains good efficiency at higher thresholds.

4.4.2 Signal distribution and threshold calibration

The distribution of charge deposition by a proton in the CBC sensor is expected to be described by a Landau-Vavilov-Bichsel (or Landau) distribution [113, 114]. This distribution can be reconstructed by scanning the comparator threshold across the range of the charge distribution in order to generate an efficiency S-curve, in a similar way to that described in Section 4.2.4, when an injection of a known charge was used. The S-curve represents the integral of the normalised charge distribution. By fitting an S-curve of the appropriate form to the measured data, the defining parameters of the underlying Landau distribution can be extracted.

As will be seen in Section 4.4.3, charge sharing between adjacent strips can lead to a reduction in efficiency. In order to minimise the effect of charge diffusing into adjacent strips, a further selection cut is made in which only those events with tracks incident near a strip implant are selected for analysis. This helps isolate the efficiency reduction to the effect of the comparator threshold. Only events with an interstrip position within 0.1 pitch units of a strip implant were selected (ie <0.1 or >0.9). Figure 4.24 (Section 4.4.4), shows that this selection cut leads to ∼90% of all selected events being one strip clusters.

In order to extract the maximum value of charge deposition, it was necessary to use the time bin with the greatest efficiency at high thresholds. For this reason, time bin 2 is used. Figure 4.13 shows the S-curve of efficiency as a function of comparator

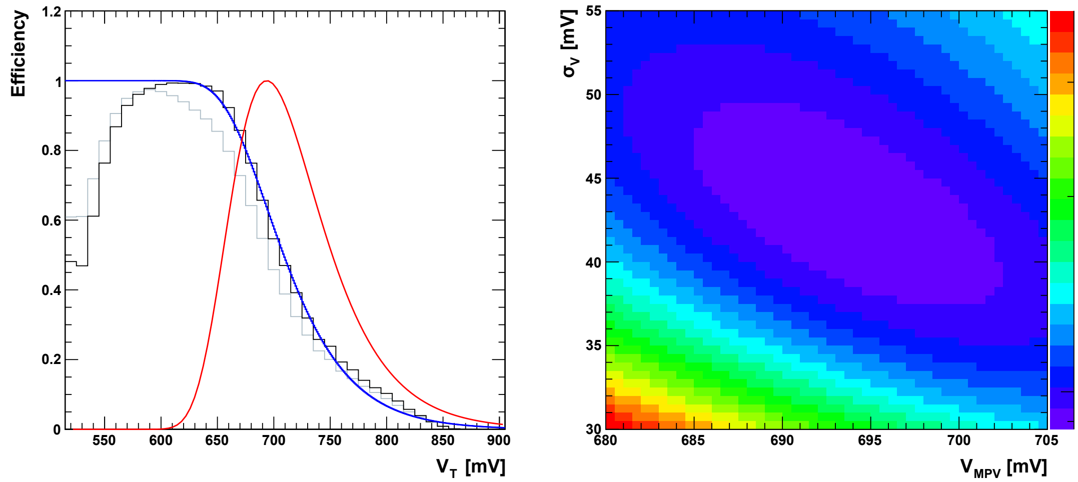

(a) (b)

Figure 4.13: (a) Efficiency as a function of comparator threshold voltage. Only data from time bin 4 are used as this gives the largest average signal. The black line includes a selection cut only on tracks incident in the vicinity (± 0.1 pitch) of a strip centre (the grey histogram shows data without this cut). Fitted to this is the S-curve in blue, given by equation 4.3. The most probable value and standard deviation are extracted and the resulting Landau distribution is shown in red (scaled in height). (b) the χ^2 distribution for most probable value and standard deviation.

threshold with the near-strip selection cut. Also shown for comparison (in grey) is the equivalent curve, without the near-strip cut. The position cut clearly delays the drop in efficiency with increased threshold as charge sharing is suppressed. The Landau distribution can be approximated by the following parameterisation,

$$L(x) = e^{-x-e^{-x}} \tag{4.2}$$

where $x = (V_{\mathrm{T}} - V_{\mathrm{MPV}})/\sigma_V$, and V_{MPV} and σ_V are the most probable value and standard deviation of the distribution respectively. The S-curve then comes from the following integral of this function,

$$S(x) = \frac{\int_x^{\infty} L(x')\,\mathrm{d}x'}{\int_{-\infty}^{\infty} L(x')\,\mathrm{d}x'}. \tag{4.3}$$

The use of time bin 2 does have the disadvantage of reducing efficiencies at low thresholds, as seen in Figure 4.11. However, as the charge deposition distribution is

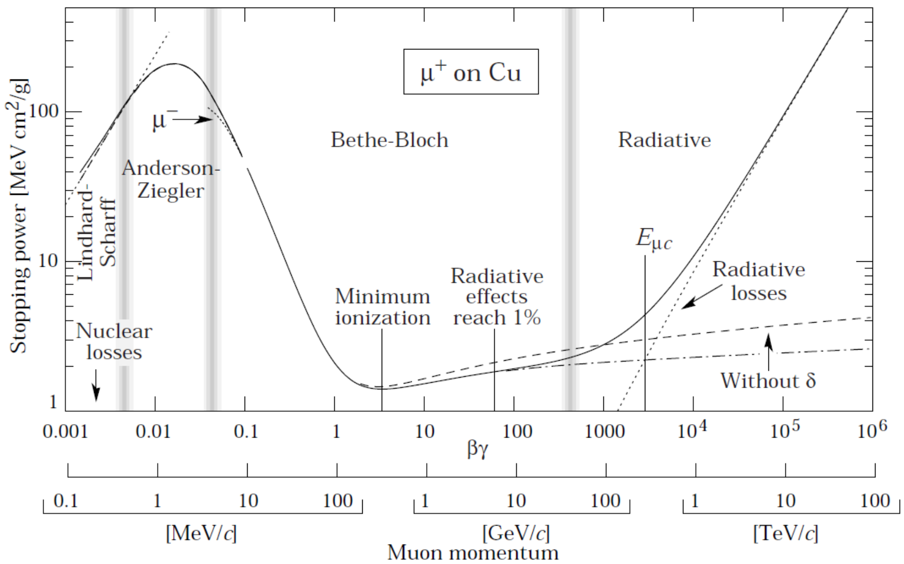

Figure 4.14: Stopping power for positive muons in copper as a function of $\beta\gamma$. Vertical bands indicate boundaries between different approximations. The central region is approximated by the Bethe-Bloch equation [100].

greater than the threshold value at which the efficiency reduces, these lower thresholds are not relevant in the fit, and the normalisation of the Landau distribution ensures that the fitted S-curve is constrained to unity at these lower thresholds. The integral is calculated numerically, and fitted to the data with a χ^2 minimisation. The best fit gives a most probable value of 693.7 mV and a standard deviation of 42.7 mV.

It is important to relate these comparator threshold voltage parameters to the size of the charge signal seen by the chip. An estimate can be made here of the expected charge deposited by a proton through the 300 μm silicon sensor. Figure 4.14 shows the energy loss rate, $\langle -\mathrm{d}E/\mathrm{d}x \rangle$, or stopping power, as a function $\beta\gamma$. This is for the specific case of muons in copper, however the form is general. In the central region, for a given material, the function depends only on $\beta\gamma$ of the incoming particle, and not its mass [100]. The central region is described well by the Bethe-Bloch equation,

$$-\left\langle \frac{\mathrm{d}E}{\mathrm{d}x} \right\rangle = K z^2 \frac{Z}{A} \frac{1}{\beta^2} \left[\frac{1}{2} \ln \frac{2 m_\mathrm{e} c^2 \beta^2 \gamma^2 T_\mathrm{max}}{I^2} - \beta^2 - \frac{\delta(\beta\gamma)}{2} \right] \tag{4.4}$$

where $K = 0.307075$ MeV g^{-1} cm^2 for silicon, z is the charge number of the incident particle and Z and A are the atomic and mass numbers of the absorber respectively.

I is the average ionisation potential of atoms in the material, estimated at 172 eV for silicon. The $\delta/2$ term is the density effect correction to ionisation energy loss. T_{max} is the is the kinematic upper limit to the kinetic energy that can be imparted to a free electron in a single collision, and is given by,

$$T_{\mathrm{max}} = \frac{2m_{\mathrm{e}}c^2\beta^2\gamma^2}{1 + 2\gamma m_{\mathrm{e}}/M + (m_{\mathrm{e}}/M)^2}. \tag{4.5}$$

Minimum ionising particles (MIPs) of unit charge have $\beta\gamma \sim 3$. The relativistic rise seen for greater values of $\beta\gamma$ comes from the $\beta^2\gamma^2$ growth of T_{max}, and is manifested as large energy transfers to electrons. This however does not necessarily represent the energy *deposition* in thin layers, as these energetic knock-on electrons can escape the material without depositing their energy. This must be accounted for, and so the *restricted energy loss rate* is used for thin layers. The effect of this is the replacement of the $\beta^2\gamma^2$ in the logarithmic term of the Bethe-Bloch equation with a constant, thus producing a so-called "Fermi plateau" for energies above minimum ionisation [100].

It should be noted that the mean and most probable values of the energy loss distribution are not equal, due to the asymmetry of the distribution. The mean is heavily weighted by very rare, large energy deposition events, and as such is difficult to determine experimentally. For this reason, the lower and more easily measured most probable value is generally used. This can be extracted from the Landau-Vavilov-Bischel distribution, and is shown as a function of kinetic energy in Figure 4.15 alongside the Bethe-Bloch and restricted energy loss relations, for muons in silicon. As the energy loss rate depends only on $\beta\gamma$ and not on mass, the relation can be used to extract the most probable energy loss for 400 GeV protons in 320 μm silicon of 85.3 ± 1.4 keV.

It has also been shown experimentally [115] that 115 GeV protons in 300 μm silicon have a most probable energy deposition of 85.5 ± 2.8 keV. This also corresponds to the Fermi plateau, and can therefore be used as an estimate for 400 GeV protons. Using this value, and assuming that 3.6 eV is needed to create each electron-hole pair, we get an estimate for the most probable charge deposition of 3.80 ± 0.12 fC.

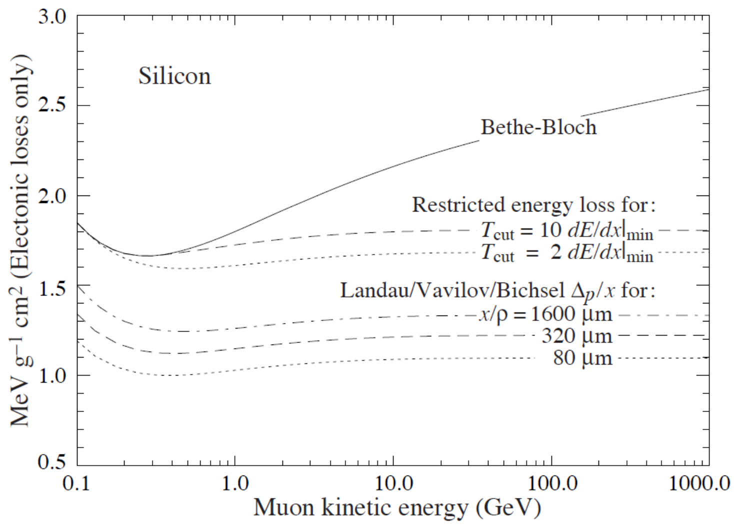

Figure 4.15: Plot of the Bethe-Bloch function alongside two examples of the restricted energy loss function and the Landau most probable energy deposition for various thicknesses. The plot is for muons incident on silicon [100].

Figure 4.16 shows this estimate plotted with the most probable value of the distribution in mV, alongside the laboratory measurements shown in Section 4.2.4. Taking the new data point and using the pedestal value of 488.9 mV we find a gain of 53.9 ± 1.7 mV fC^{-1}. This value can be used with the pedestal value to provide the comparator threshold voltage [mV] in terms of effective charge [fC],

$$Q_{\mathrm{T}} = \frac{V_{\mathrm{T}} - 488.9}{53.9}. \tag{4.6}$$

The standard deviation of the distribution is estimated as $\sigma_Q = 0.79$ fC, which contains a contribution from Gaussian noise (measured in the laboratory to be $\sim$0.14 fC). Subtracting the noise contribution we obtain a standard deviation of $\sigma_Q = 0.78$ fC. The ratio $\sigma_Q/Q_{\mathrm{MPV}} = 0.205$ is consistent with the expected ratio of $\sim$0.2 for 300 μm of silicon [24].

4.4.3 Noise and efficiency

Two of the most important considerations in the performance of a binary readout module are the efficiency and noise occupancy at the operating threshold.

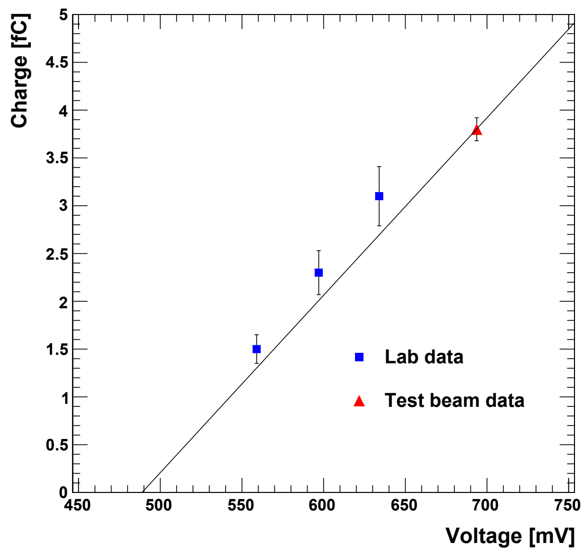

Figure 4.16: Charge signal as a function of comparator threshold voltage. The three test laboratory test pulses give a pedestal value of 488.9 mV, and carry correlated errors of ±10% that translate to the gain measurement. The test beam data point comes from the measured most probable value of signal in terms of comparator threshold voltage, and the theoretical and experimental prediction of charge deposition in the CBC sensor.

The noise occupancy is defined as the proportion of events in a given time period (eg bunch crossing) where there is no track incident on the CBC sensor, but in which the CBC module still registers an event. This is made possible by using the same event selection criteria as outlined in Section 4.3.3, but with the x position cut being made such that the track is incident beyond a margin of 2 mm either side of the CBC sensor (the noise occupancy was seen to plateau to a minimum value with a margin of around 2 mm). It was not necessary to make an event selection on time bin, as only events with no incident track were selected.

Figure 4.17 shows how noise occupancy per channel varies with comparator threshold. The noise is seen to reduce rapidly with increased threshold towards a minimum around the operational level of 1 fC. Beyond this the noise appears to flatten to a background level of $\sim 8 \times 10^{-4}$. This is most likely due to random hits incident on the sensor that had not been reconstructed by the telescope.

Figure 4.17 can be used to estimate the electronic noise level. The frequency of noise hits is given by

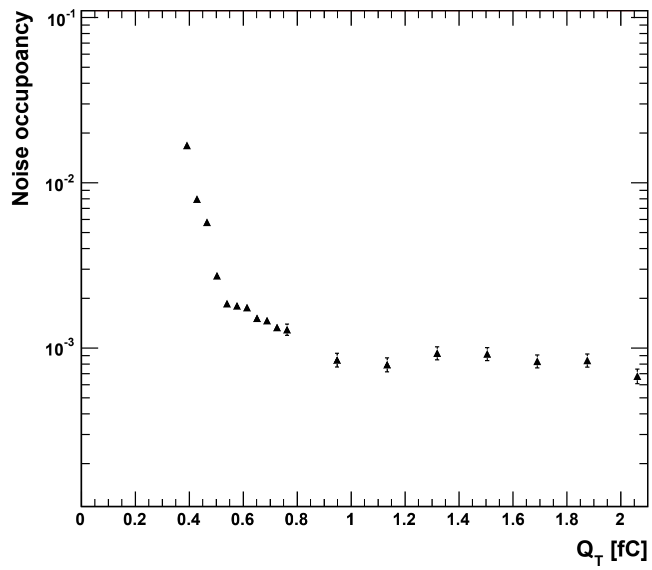

Figure 4.17: Noise occupancy as a function of comparator threshold.

$$f_{\mathrm{n}} = \frac{1}{4\sqrt{3}\tau} e^{-Q_{\mathrm{T}}^2/2Q_{\mathrm{n}}^2} \tag{4.7}$$

where τ is pulse shaping time and Q_{n} is the noise level [24]. The noise occupancy, P_{n}, over a given sampling interval Δt (25 ns in this case) is then given by the product $\Delta t\, f_{\mathrm{n}}$. Using equation 4.7, and taking natural logarithms, we get the following linear relation between Q_{T}^2 and $\ln P_{\mathrm{n}}$

$$\ln P_{\mathrm{n}} = \ln\left(\frac{\Delta t}{4\sqrt{3}\tau}\right) - \frac{1}{2}\left(\frac{Q_{\mathrm{T}}}{Q_{\mathrm{n}}}\right)^2 . \tag{4.8}$$

Figure 4.18 shows the first five data points from Figure 4.17, with an assumed background level of 8×10^{-4} subtracted. A linear regression fit to these five points gives a noise level of 1001 ± 32 electrons. An assumed uncertainty in the background level of 2×10^{-4} leads to a further uncertainty in noise level of 33 electrons. Combining these errors in quadrature we obtain an estimate for the noise of 1001 ± 46 electrons. This is greater than that seen in laboratory tests (Section 4.2.4), but in line with the specification of <1000 electrons for a sensor capacitance of up to 5 pF. No specification for noise occupancy has been defined, though Figure 4.18 shows

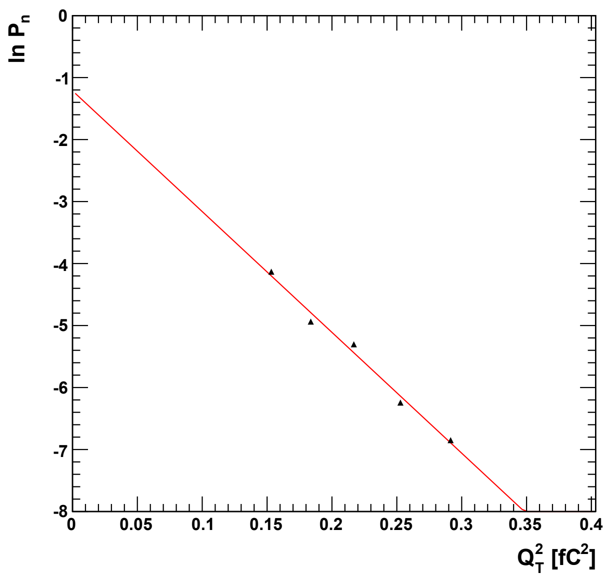

Figure 4.18: $\ln P_\mathrm{n}$ vs Q_T^2. This linear relation allows an estimate of the electronic noise level.

consistency with the ATLAS Semiconductor Tracker (SCT) requirement of noise occupancy below 5×10^{-4} at operating thresholds [116].

Due to the fact that only discrete position measurements are possible with a binary readout system, non-uniformities in efficiency may be seen depending on the precise position of the track relative to neighbouring strips. The high spatial resolution of the telescope allows a good estimate of the position of a track on the CBC sensor, relative to the periodicity of its strips. Due to the low divergence of the proton beam, the small scatter angle from the last telescope plane and the close proximity of the CBC sensor to the last telescope plane, the position of a track on the CBC sensor can be estimated simply as that measured on the last telescope plane. The interstrip position can be defined as the position of a track across one unit of strip pitch, with 0 and 1 defined as the position of two adjacent strip implants. Figure 4.19 shows the variation of efficiency across the interstrip position (note that the distribution is smeared horizontally, due to the telescope spatial resolution of 6.9 μm). In the central region the charge sharing between adjacent strips is maximised, leading to a lower signal on each strip, and a corresponding reduction in efficiency at higher thresholds. At operating thresholds the efficiency is uniformly above 99% at all

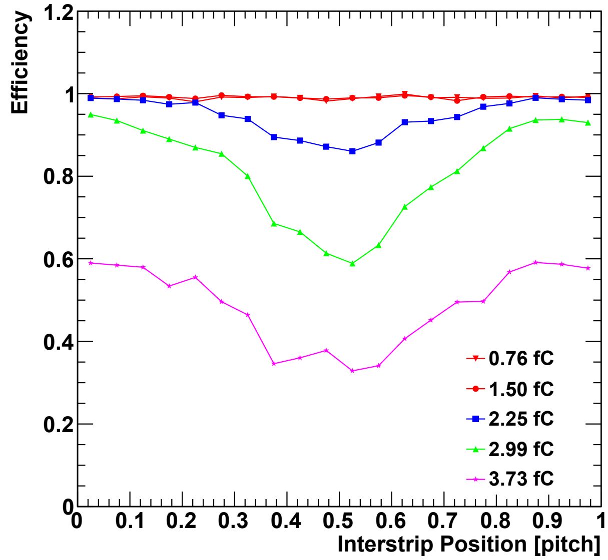

Figure 4.19: Efficiency as a function of interstrip position for various threshold values.

interstrip positions. This feature is consistent with results seen with ATLAS SCT strip detector modules [116].

4.4.4 Spatial resolution

The spatial resolution of hits in a tracking system is a key parameter in the ability to reconstruct tracks accurately. In the current analogue readout system used in the CMS Tracker, accurate position measurements are possible through the clustering algorithms that make use of analogue information of charge depositions on strips. In a binary readout system this is not possible, so it is important that the binary hit information can be interpreted correctly and give a sufficiently good estimate of the track position. A cluster in a binary system is defined as a group of adjacent strips that register a hit. The best estimate of the hit position represented by the cluster is then the midpoint of the cluster, leading to a pitch/2 discretisation of possible hit positions (depending on whether there are an even or odd number of strips in the cluster).

Figure 4.20 shows the distribution of cluster widths for tracks incident normal to the sensor, for thresholds of 0.76 fC and 2.25 fC. With a threshold of 0.76 fC it is seen

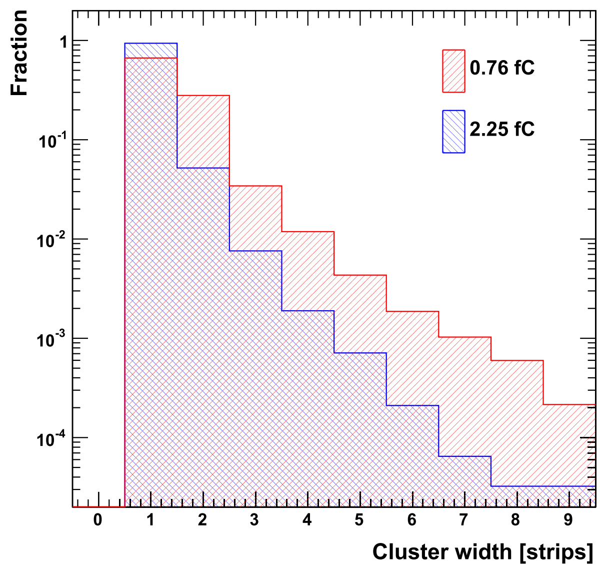

Figure 4.20: Cluster width distributions for incident tracks at thresholds of 0.76 fC and 2.25 fC.

that one and two strip clusters make up 66.6% and 27.9% of all clusters respectively. At larger thresholds the distribution is shifted further towards smaller clusters as charge depositions in strips adjacent to the true track position fail to exceed the threshold. Larger clusters can be attributed to merged clusters from two separate tracks (possibly as a result of upstream interactions) or the production of δ-rays within the sensor material (Section 4.4.5).

The residual for a track is defined in a similar way to that in Section 2.8.3, as the difference in measured hit position between the CBC sensor, d, and the telescope plane 5 hit position, f,

$$r = d - f. \tag{4.9}$$

The spread of the residual distribution is thus the resolution of the CBC sensor added in quadrature with the resolution of the fifth telescope plane. The CBC hit position is calculated as the product of the bonded CBC channel number and the strip pitch, with a positional shift in x to align the sensor with the telescope. As the Hamamatsu sensor was fan shaped, with pitch varying from 120 μm to 150 μm in y, it was necessary to determine the pitch at the beam position. This was done

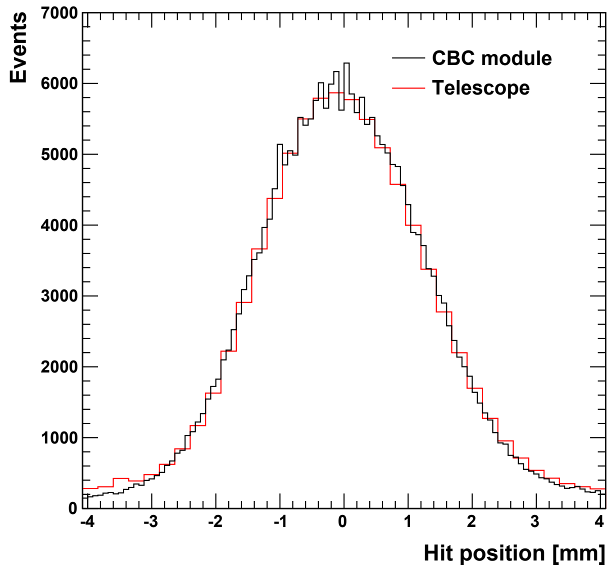

Figure 4.21: Beam profiles (in x) for the CBC module and fifth telescope plane (note that the number of events in the telescope plot has been rescaled).

by varying the input value for the pitch, and choosing the value that minimised the width of the residual distribution. The minimum width was found to be at 134.4 μm, and this was then taken as the sensor pitch at the beam position. The vertical selection cut then ensures that the pitch is effectively constant (as well as minimising the effect of any rotational misalignments between CBC sensor and telescope).

Alignment of the CBC sensor with the telescope is performed by setting the x positional shift such that the residual distribution is centred on zero. Once the alignment has been made the beam profile as seen with the CBC module can be compared with that of the telescope. Figure 4.21 shows good agreement between CBC module and telescope.

Figure 4.22 shows the residual distributions for the Hamamatsu and Infineon sensors with one and two strip clusters shaded in red and blue respectively. Wide bins are required in both plots in order to remove periodic patterns that arise as artifacts of the difference in strip pitch between the telescope and CBC sensors. Both distributions have an overall Gaussian form, and it can be seen that the residuals of two strip clusters have a narrower spread than those of one strip clusters. As the

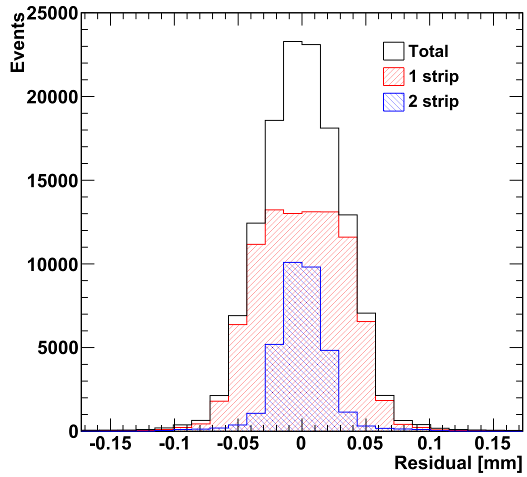

(a)

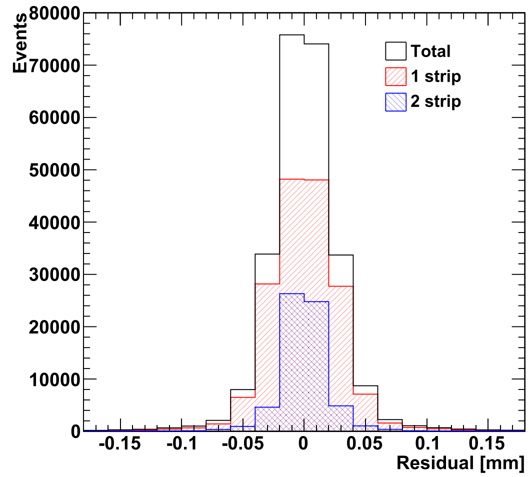

(b)

Figure 4.22: Residual distributions for one strip, two strip, and all clusters. (a) Hamamatsu sensor (2011), (b) Infineon sensor (2012).

distributions are symmetric it is possible to fold each over into the positive region by taking the absolute values of the residuals (note that this also means that the bin width can be halved without reintroducing the periodic pattern discussed). Figure 4.23 shows the separate distributions of absolute values of residuals from one and two strip clusters, for each of the two sensors.

One strip clusters from the Hamamatsu sensor exhibit the uniform residual distribution between ±pitch/2 that is characteristic of binary readout. Two strip clusters occur predominantly in the narrow region in between two adjacent strips, leading to the narrower residual distribution. As the border between regions of one and two strip cluster production is not precise, a smearing of the two distributions results. The smearing is further enhanced by the telescope resolution. The one strip cluster residuals are fitted with a Gaussian error function, returning a half-width of 49.8 μm and a standard deviation of 14.2 μm, giving a combined spread of 32.1 μm. The two strip cluster residuals are fitted with a Gaussian, with standard deviation 17.0 μm. With the Infineon sensor, due to the smaller strip pitch, the smearing is sufficient for both one and two strip distributions to be approximated by Gaussians, with standard deviations of 24.9 μm and 14.9 μm respectively. Table 4.2 gives the widths of the distributions of one and two strip clusters for each sensor, as well as the

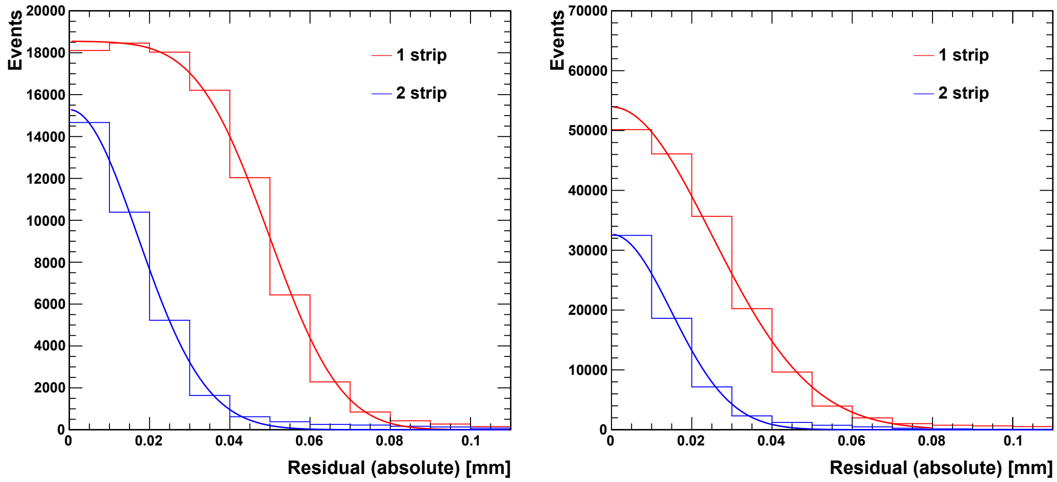

(a) (b)

Figure 4.23: Distribution of residual absolute values for one and two strip clusters. (a) Hamamatsu sensor (2011), (b) Infineon sensor (2012).

Table 4.2: Spatial resolutions of sensors [μm].

	Hamamatsu, 2011	Infineon, 2012
1 strip clusters	31.3	23.9
2 strip clusters	15.5	13.2
1 & 2 strip clusters (weighted mean)	27.4	21.1
Pitch/$\sqrt{12}$	38.8	23.1

weighted mean. All values have had the effect of the telescope resolution of 7.0 μm subtracted in quadrature. The resolutions obtained are better than the expected binary resolution of pitch/$\sqrt{12}$, as the cluster width provides additional information as to the position of the track.

The spatial variation of one and two strip clusters across sensor strips can be seen explicitly by plotting the fraction of one and two strip clusters as a function of interstrip position. This is shown in Figure 4.24, again for both sensors. It is clear that two strip clusters dominate primarily in the mid-strip region. The plot for the Hamamatsu sensor also clearly shows the flat distribution for one strip clusters implied by the residual plot. Note that the smearing from the telescope resolution is more significant in the case of the Infineon sensor due to the smaller strip pitch.

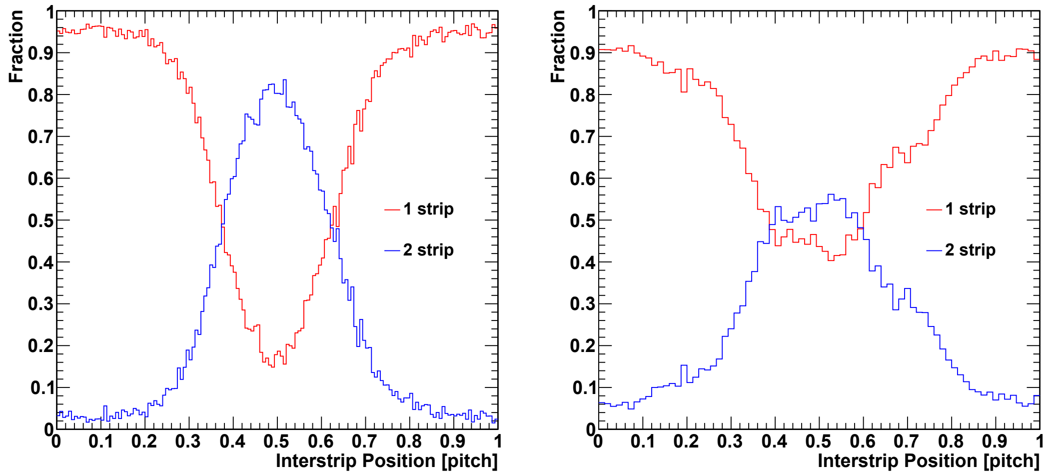

(a) (b)

Figure 4.24: Proportion of events that lead to one and two strip clusters, as a function of interstrip position. Values of 0 and 1 represent strip implant positions. (a) Hamamatsu sensor (2011), (b) Infineon sensor (2012).

4.4.5 Large cluster events

Figure 4.20 shows that while one and two strip clusters dominate, clusters of four or more strips account for 0.5% of selected events, and should therefore be understood. Large charge depositions corresponding to the high energy tail of the Landau distribution could explain clusters up to a few strips wide, but larger clusters require an alternative explanation.

Figure 4.25 shows normalised plots of residuals for 6, 8 and 10 strip cluster events. To gain adequate statistics, all data from the threshold range 0.58-1.13 fC are included. It is clear that each distribution shows two symmetric peaks about the origin, and furthermore these peaks are separated by roughly the corresponding cluster width. This indicates that any proton impact position would have been at one end of the cluster, suggesting that the cluster propagates out in only one direction from the impact position. One mechanism that could account for such events would be the production of δ-rays along the proton path, which propagate through the sensor material with a component transverse to the strip direction, depositing charge in adjacent strips and thus creating a wide cluster. Residuals with intermediate values

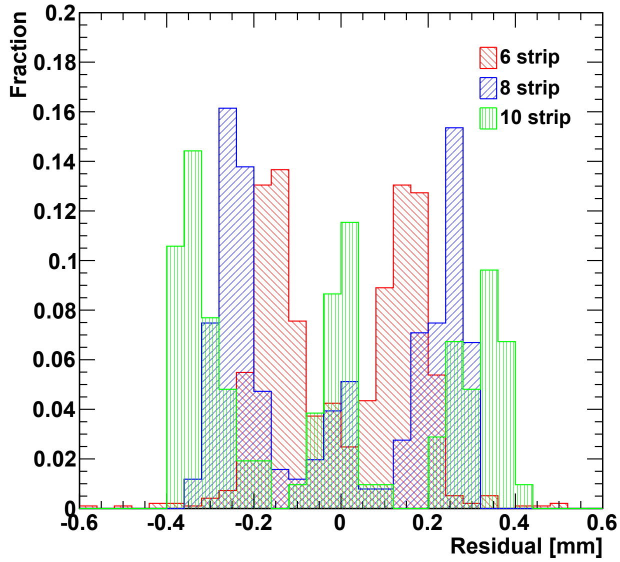

Figure 4.25: Residual distributions for 6, 8 and 10 strip clusters. Each distribution is normalised (966, 254, 104 events respectively).

could be at least partially explained by events in which multiple δ-rays are produced, propagating in opposite transverse directions.

To investigate the possible contributions from δ-rays, two simulation studies have been made. The first is a simple toy Monte Carlo simulation using a semiempirical model to calculate δ-ray production in silicon, and the second is a Geant4 simulation.

Toy Monte Carlo model

Following the method outlined in Ref. [117], the probability distribution per event for producing a δ-ray of a certain energy is calculated for 400 GeV protons incident on 300 μm of silicon. δ-rays are assumed to be produced only in the CBC sensor, and the contribution from those produced upstream is neglected.

It can be shown [117] that the probability of producing a δ-electron of energy $E > E_r$, in a material of thickness R, is given by

$$\mathrm{P}(E > E_r) = \mathrm{P}(\lambda > \lambda_r) = 1/\lambda_r \tag{4.10}$$

where E_r is the energy of a δ-ray that has an expected straight line penetration distance of r. λ_r is given by

$$\lambda_r = \frac{E_r - \bar{E}}{\xi} - (1 + \beta^2 - C_{\mathrm{E}}) - \ln k(R) \tag{4.11}$$

where C_{E} is Euler's constant ($\sim$0.5772), $\xi/R = 0.0178$ keVμm^{-1} for silicon, and $k = \xi/T_{\max}$, with $T_{\max}$ defined in equation 4.5. $\bar{E}$ is the expected energy loss in thickness R, and is given by the Bethe-Block formula (equation 4.4). δ has been parameterised for many media by Sternheimer [118]. For silicon we have

$$\delta(\beta\gamma) = 4.6052 \log_{10}(\beta\gamma) - 4.435. \tag{4.12}$$

Making the necessary substitutions of ξ, $\bar{E}$, K into equation 4.11, we obtain an expression for λ_r as a function of E_r,

$$\lambda_r = 56.18\frac{E_r}{R} - \ln R - 10.338 \tag{4.13}$$

with E_r in keV and R in μm. In the case that $R = 300$ μm, and using equation 4.10, we find a probability distribution function for producing a δ-electron of energy $E > E_r$ of

$$\mathrm{P}(E > E_r) = \frac{1}{\lambda_r} = \frac{5.34}{E_r - 85.66}. \tag{4.14}$$

The probability density then follows as

$$-\frac{\mathrm{d}P(E > E_r)}{\mathrm{d}E_r} = \frac{5.34}{(E_r - 85.66)^2}. \tag{4.15}$$

This function is then normalised by choosing an appropriate low cut off point of $E_{\min} = 90.00$ keV (assuming that $E_{\max}\sim\infty$). This distribution is sampled to give the probability per event for the production of a δ-electron of energy E_r. The expected straight line penetration distance (generally shorter than the total path length) of a δ-electron has been parameterised for aluminium, according to the following empirical form [119],

$$r = AE\left(1 - \frac{B}{1 + CE}\right) \tag{4.16}$$

where $A = 0.55\ \mathrm{mg\,cm^{-2}\,keV^{-1}}$, $B = 0.9841$ and $C = 0.003\ \mathrm{keV^{-1}}$, and r is in units of $\mathrm{mg\,cm^{-2}}$. Assuming the same approximation for silicon and taking its density as $2.329\ \mathrm{g\,cm^{-3}}$, we obtain the empirical relationship for the expected range of a δ-electron of energy E_r of

$$r = 2.362\,E_r\left(1 - \frac{0.981}{1 + 0.003E_r}\right) \tag{4.17}$$

where r is now in units of μm, and E_r is in keV.

For each event, the model assumes that a δ-ray is produced with an energy E_r, the production of which is isotropic, and at a random position throughout the thickness of the sensor. The straight line distance is estimated using equation 4.17, and from this the distance propagated transverse to the strip direction and within the sensor material is calculated. Assuming a linear energy loss along the straight line path, the energy deposited in the final strip is calculated, and if above the threshold value set the strip is included in the cluster. The energy threshold is set to 21390 eV, which represents $\sim$0.95 fC for silicon (equivalent to a comparator threshold voltage of 540 mV).

Figure 4.26 shows a normalised cluster width distribution for the Monte Carlo model compared with data, for cluster widths of >3 strips. Data are from the Infineon sensor (80 μm pitch), with a comparator threshold of $\sim$0.95 fC (540 mV). The model shows an excess over the data for clusters of more than 8 strips, although the general trends show good agreement. The assumption of isotropic δ-ray production is likely to be a source for overestimation of large clusters, due to the forward production of the higher energy δ-rays as a result of kinematic constraints.

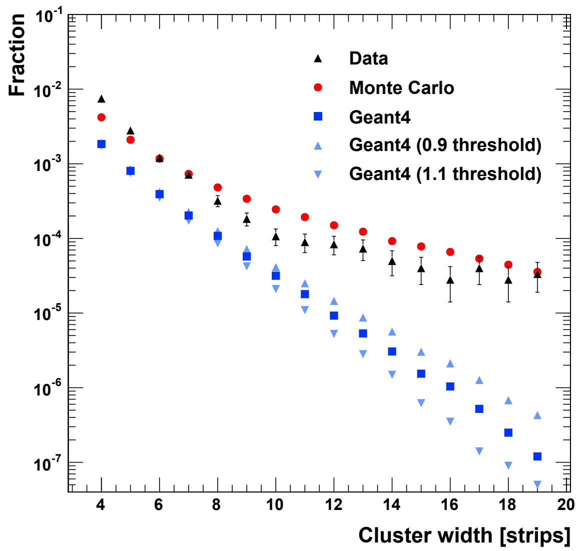

Figure 4.26: Fraction of all clusters of width greater than three strips, shown for data, compared with results from the simple Monte Carlo model and Geant4 simulation. In each case the comparator threshold is set to ∼0.95 fC (540 mV). The Geant4 simulation is additionally shown with threshold values of 0.9 and 1.1 times the nominal value.

Geant4 simulation

The Geant4 toolkit provides a comprehensive set of electromagnetic, hadronic and optical physics models, which can be used to describe the interaction of particles with matter over a wide range of energy and detector applications. Models are based on theory, experimental data or parameterisations [120]. In this simulation the low energy electromagnetic Livermore package [121] was used to improve validation at low energies. The Livermore models include atomic shell structure effects and extends the range of accuracy for electromagnetic interactions down to 250 eV. The approach uses evaluated libraries [122, 123, 124] that provide data for the calculation of cross sections and for the sampling of the final state from interactions of photons, electrons and ions with matter [120].

The geometry of the Infineon sensor was defined using Constructive Solid Geometry (CSG) modelling, with each strip modelled as a simple silicon cuboid, of dimensions $80 \times 10^5 \times 300$ μm^3 in x, y and z. The sensor comprised 41 adjacent strips in x, accommodating clusters of width 20 strips in either direction. The sensor was centered on the origin. The Geant4 particle gun was used to provide 400 GeV protons along the z-axis, incident in the centre of the middle strip. This was consistent with the geometric selection cut made on the data, in which only single tracks incident near the strip implant were selected.

The production and tracking of secondary particles produced in interactions may be suppressed if their expected range is below that of a user defined range cut, and the energy associated with them is instead deposited locally. The range cut is equivalent to an energy cut, but is used in preference as it allows for a simpler policy in how to handle different particles and materials [125]. For this simulation a range cut of 10 μm was used for photons, electron and positrons, which is sufficiently small compared to the sensor geometry.

In each event hits were recorded on strips in which the energy deposition exceeded a configurable threshold. The threshold was nominally set to 21390 eV, representing a comparator threshold of $\sim$95 fC (540 mV). Clustering of hits was performed, and a selection was made only of events in which a single cluster about the central strip was observed (for consistency with the data selection).

Figure 4.26 shows the normalised cluster width distribution for the Geant4 simulation, again compared with the data. It is clear that Geant4 is not in such good agreement with the data as the simpler Monte Carlo simulation. To understand the sensitivity of the simulation results to the comparator threshold level used, the threshold was varied from the nominal value by $\pm$10%, also displayed in Figure 4.26. The generation of charge carriers in silicon is well understood, so the small uncertainty in the threshold calibration (Section 4.4.2) is unable to account for the observed discrepancy.

Figure 4.27 shows the residual distributions from the Geant4 simulation, for cluster widths of 6, 8 and 10 strips. A large proportion ($\sim$90%) of clusters have residuals that are offset by half of the cluster width, which is consistent with observations from the experimental data (Figure 4.25), and indicates the presence of δ-rays. However the absence of the central peaks seen in Figure 4.25 suggests that the presence of multiple δ-rays cannot account for the wide clusters that are symmetrical about the impact position. An alternative explanation is needed to explain such events, and is

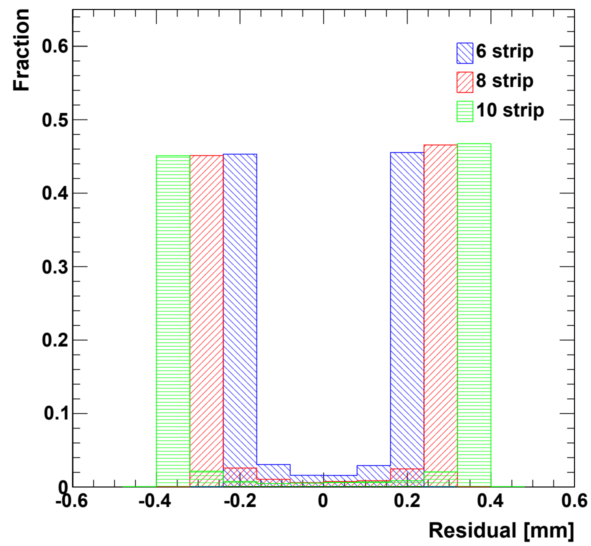

Figure 4.27: Residual distributions for 6, 8 and 10 strip clusters from the Geant4 simulation. Each distribution is normalised (39205, 10832, 3160 events respectively).

likely to concern higher level effects that should be included in simulations. Further refinements to the simulation would include the modelling of charge collection and noise in the sensor accounting for the effects of crosstalk and electrical noise in the chip. Further insight could also be gained from comparison of simulations with additional data, when available, from a range of experimental conditions including beam species and energy, as well as sensor geometry and operating voltages.

Whilst only poor quantitative agreement is reached by the toy Monte Carlo and Geant4 simulations, both indicate that δ-rays contribute to events with large clusters. The production of δ-rays has also been identified by large clusters and their residual distributions in the ATLAS SCT and Pixel detector [126], where the rate of δ-ray production, inferred from wide clusters, was found to agree with that expected from the reconstructed tracks, and with Monte Carlo simulation. In a full tracker at CMS, such measurements could in principle be used to correct the cluster centroid position of hits that produce a transverse δ-ray. This might be particularly useful in a binary readout system where the lack of charge information prevents the use of centroid finding algorithms [126].

4.4.6 Tilted Sensors

It is foreseen that high p_T candidates, or stubs, will be identified by the upgraded CMS Tracker, as part of the L1T. Modules currently under development are to provide this functionality in the CMS TOB, between radii of 540 mm and 1080 mm. The CBC2 is the next iteration of the CBC, and is designed for use within such modules (Section 4.5). One way the CBC2 can be used to select stubs is by discriminating against wide clusters, associated with low p_T tracks.

During the 2013 run, data were collected with sensors rotated across a range of different angles to the beam, in order to simulate various of p_T values. Sensors were rotated about the y-axis, at angles of 0°, 10°, 20° and 30° (Figure 4.28).

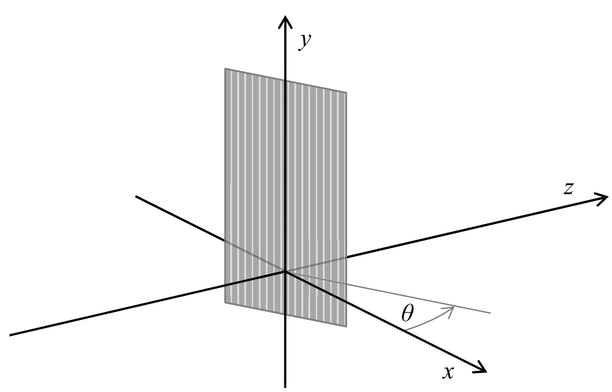

Figure 4.28: Sensors are tilted about the y-axis to simulate various p_T values.

Assuming a magnetic field of 4 T in the CMS Tracker, the p_T of a charged particle with vertex at the origin can be shown to vary with its charge number, q, and radial position, r, according to the following relation,

$$p_\mathrm{T} = \frac{0.6\, r\, q}{\sin\theta} \tag{4.18}$$

where θ is the incident angle that a particle makes with a barrel layer at r, in the r-ϕ plane, and p_T and r in units of GeV/c and m respectively. Assuming a unit charge, there exists a relation between p_T and θ, for any particle at a given radius. Figure 4.29 shows this relation for the inner and outer radii of the TOB.

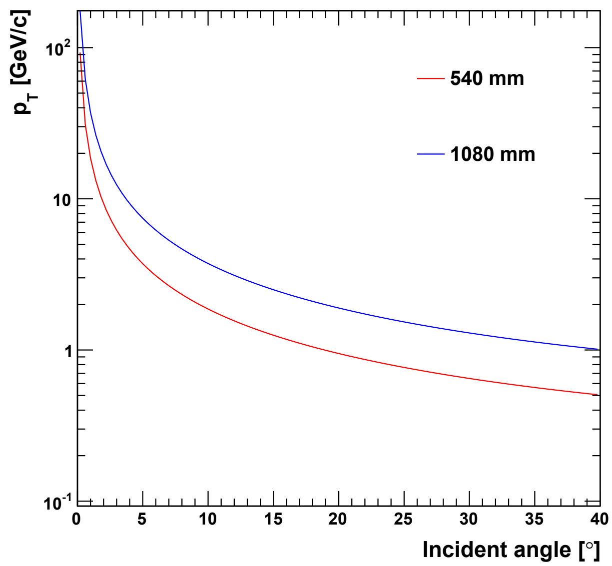

Figure 4.29: p_{T} as a function of incident angle for radii of 540 mm and 1080 mm.

Figure 4.30a shows the cluster width distribution at each sensor angle. Data were not collected with the 10° sensor for comparator thresholds beyond 530 mV (0.76 fC). For this reason only data collected at 530 mV are shown for all angles. Table 4.3 shows the fraction of 1, 2, 3 and 4 strip clusters as a function of angle and p_{T} at the TOB's inner and outer radii. Figure 4.30b shows the same data plotted in a 2-dimensional histogram, along with the mean value for each angle. The width of a sensor that a particle passes through scales linearly with $\tan\theta$, leading to the corresponding distribution of wider clusters seen with increased angle. The line added is linear with $\tan\theta$, and a best fit returns the following estimate for the mean cluster width, $\bar{W}$, as a function of θ,

$$\bar{W} = 1.4 + 1.3246 \tan\theta. \tag{4.19}$$

Using equation 4.18, we then find $\bar{W}$ as a function of p_{T},

$$\begin{aligned} \bar{W} &= 1.4 + 1.3246 \tan\left(\arcsin\left(\frac{0.6\,r\,q}{p_{\mathrm{T}}}\right)\right) \\ &= 1.4 + \frac{0.7948\,r}{\sqrt{p_{\mathrm{T}}^2 - 0.36 r^2 q^2}}. \end{aligned} \tag{4.20}$$

Table 4.3: Fraction of cluster widths for various incident angles.

θ [°]	p_{T} [GeV/c] (at 540 mm)	p_{T} [GeV/c] (at 1080 mm)	1 strip	2 strip	3 strip	4 strip
0	∞	∞	0.67	0.28	0.03	0.01
10	1.87	3.73	0.48	0.47	0.04	0.01
20	0.95	1.89	0.35	0.52	0.09	0.02
30	0.65	1.30	0.32	0.25	0.39	0.02

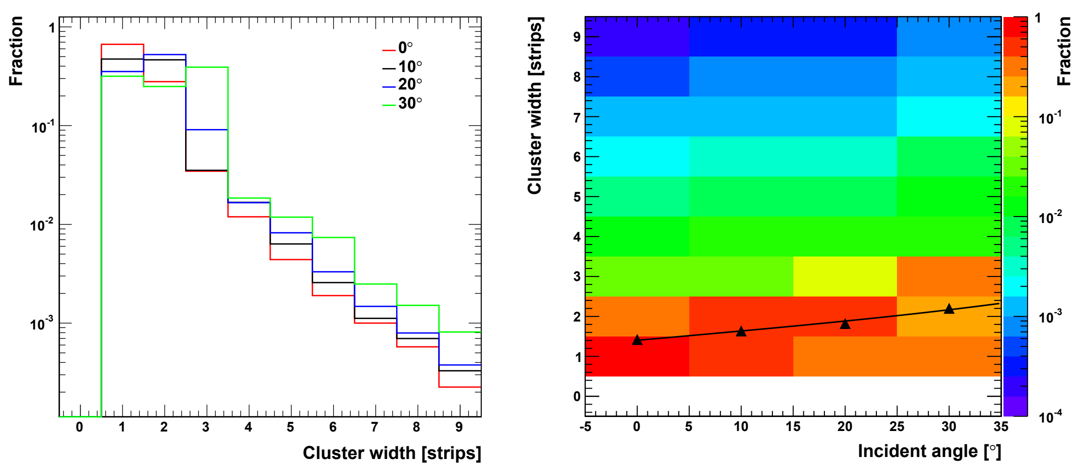

(a) (b)

Figure 4.30: (a) Cluster width distribution for sensors at 0°, 10°, 20° and 30°. (b) The same data in a 2-dimensional histogram. The points represent mean cluster width.

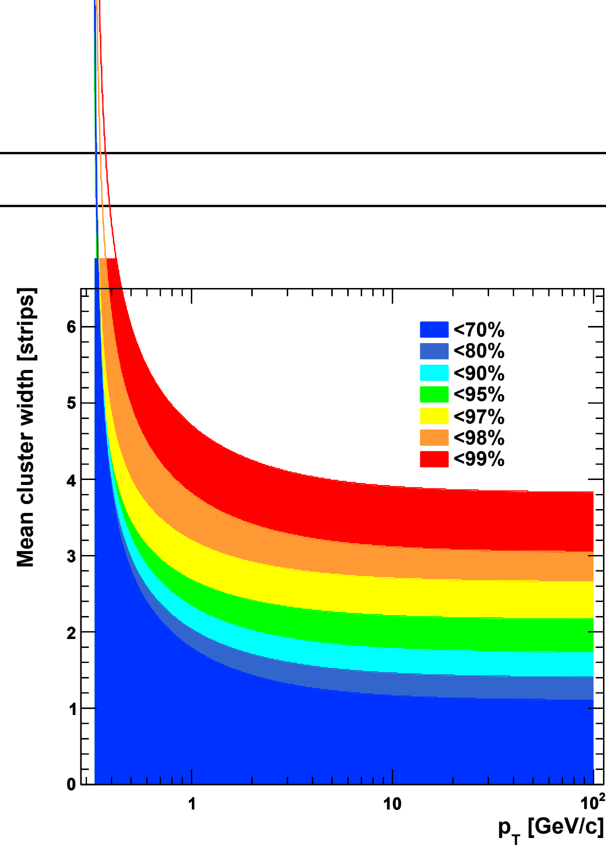

Figure 4.31: Cluster acceptance as a function of p_{T} and cluster width cut, for a barrel layer at $r = 540$ mm.

As there is a reasonably wide distribution of cluster widths at any particular p_{T}, any cut based on cluster width will inevitably reject a certain number of high p_{T} tracks (false negatives) and accept a number of low p_{T} tracks (false positives). For the purpose of selecting high p_{T} tracks based on cluster width, it is useful to know what proportion of tracks of a certain p_{T} are accepted with different cluster width cuts. The cumulative cluster width distribution allows an estimate of the cluster width cut required to accept a certain fraction of events, for a given incident angle (linear interpolation means that the cluster width cut estimate is not necessarily integer valued). A linear function of $\tan\theta$ is again fitted to the data for various acceptance values, and for each a relation between the cluster width cut and p_{T} is found. Figure 4.31 shows the regions of acceptance for tracks of various p_{T} for different cuts on cluster width, for a barrel layer at $r = 540$ mm.

It is seen for example that a cluster width cut of 3 strips will accept $\sim$96% of $p_{\mathrm{T}} = 1$ GeV/c tracks and $\sim$97% of $p_{\mathrm{T}} = 2$ GeV/c tracks. A cluster width cut of 2 strips will accept $\sim$80% of $p_{\mathrm{T}} = 1$ GeV/c tracks and $\sim$90% of $p_{\mathrm{T}} = 2$ GeV/c tracks. It is notable that even for $p_{\mathrm{T}} > 10$ GeV/c using a selection of up to four strip clusters, full acceptance is not seen. This is largely due to the rare wide clusters that always form as a result of δ-rays.

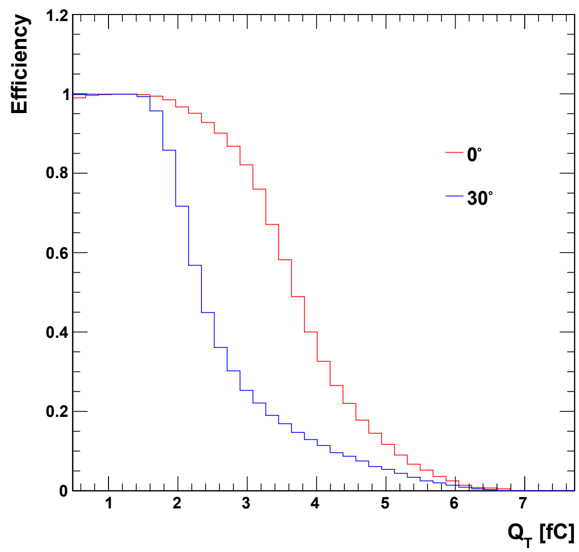

Figure 4.32: Efficiency as a function of threshold for incident angles of 0° and 30°.

An important consideration to be made with increased incident angle is that of efficiency reduction. Due to tracks passing through multiple strips, the path length through any particular strip is reduced, resulting in a smaller charge deposition on each strip. Figure 4.32 shows efficiency as a function of threshold for sensors at 0° and 30°. The drop in efficiency occurs at lower thresholds with the 30° sensor, however efficiency remains above 95% for thresholds up to 1.69 fC. This suggests that there is no significant drop in efficiency at operating thresholds for $p_{\mathrm{T}} > 0.65$ GeV/c at $r = 540$ mm or $p_{\mathrm{T}} > 1.3$ GeV/c at $r = 1080$ mm.

4.5 CBC2

The CBC2 is the next iteration of the CBC, and is designed to include Level-1 Trigger logic for readout of silicon strips with pitch 90 μm in the CMS TOB ($r > 500$ mm). The CBC2 is based on the same front-end circuitry as the CBC, with only minor modifications [108]. The chip has nearly double the number of input channels at 254 (plus 2 bits for null-event encoding), and is bump bondable to the substrate.

The CBC2 is designed to instrument double layer modules comprising two closely spaced silicon strip sensors. The chip design incorporates logic to identify high p_{T}

L1T primitives called stubs. The stub finding logic consists of two stages. The first stage is the Cluster Width Discrimination (CWD), which rejects wide clusters on both sensors, typically consistent with low p_{T} tracks. The rejection is configurable for clusters of greater than one, two or three strips. For two strip clusters the logic currently selects the strip with the lower address as the cluster centre, although the next iteration is planned to adopt half-pitch segmentation. The second stage in the logic looks for coincidence in ϕ between inner and outer layers, corresponding to a high p_{T} track. For any valid cluster in the inner layer, a valid cluster on the outer layer is accepted if it falls within a coincidence window of the cluster on the inner layer (Figure 4.33a). The outer layer coincidence window size and position defines the p_{T} cut. The central position of the window is configurable to ± 3 strips, and adjusted to account for the geometric displacement in ϕ between strips on either sensor. The width of the window is configurable in the range ± 8 strips from the central strip. Simulations have shown that tracks could be reconstructed with sufficient angular resolution to match them with Level-1 calorimeter objects [14].

Figure 4.33b shows the stacked strip p_{T} (2S-Pt) module that has been under development. It is designed to be lightweight and rely on commercial interconnection technologies [108, 127]. The sensor separation is in the 1-4 mm range, and the optimum value depends on the radial position in the Tracker and the p_{T} cut required. Strip sensors are wire bonded to the substrate and read out by 16 CBC2 chips. Each chip reads out 127 strips from each of the upper and lower sensor layers, with input channels connected alternately to strips on each layer.

As the CWD and correlation logic relies on inputs from neighbouring channels, links are required between chips in the region of their boundary. For each logic channel the input of the adjacent 30 channels is required (± 2 for CWD on both upper and lower sensors, ± 3 for coincidence window offset and ± 8 for coincidence window width). For this reason, 15 input and 15 output pads are assigned to interchip links. At present modules are designed to be independent units without such a transmission scheme between boundaries, however overlap of modules will ensure that high p_{T} tracks straddling adjacent modules will not be lost [108].

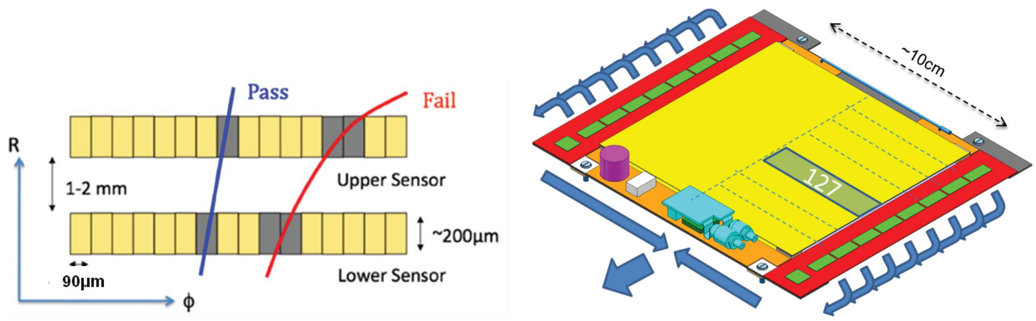

(a) (b)

Figure 4.33: (a) Stacked tracking concept for selection of high p_{T} tracks, (b) Proposed stacked strip 2S-Pt module [108].

The CBC2 was submitted for production in August 2012 and production began in early 2013. Its on-chip stub selection logic represents a significant step in the development of a Level-1 Trigger system that benefits from tracking information.

4.6 Summary

The CMS Binary Chip is a prototype of a proposed readout chip for use with silicon strips in the upgraded CMS Tracker in the HL-LHC. The binary, unsparsified architecture of the chip makes it well suited to handle the high multiplicities at the HL-LHC, while keeping data rates and power and cooling requirements down.

Tests have been performed in the laboratory, which have shown the chip to operate within specification in power, noise and timewalk. Beam tests have been conducted in the H8 beamline, with CBC modules operating parasitically off the beam telescope described in Chapter 2. The CBC operated as expected, without recording errors.

Hit finding efficiency was shown to be >99% where sampling of the CR-RC pulse shape corresponded to the peak, as would be the case when synchronised to a bunch structured beam. Efficiency was reduced elsewhere. Efficiency measurements were used to reconstruct the Landau distribution of charge deposition in the sensor by sweeping the comparator from a low to a high threshold voltage. Noise performance was seen to be consistent with that observed in the laboratory.

The weighted mean spatial resolution for 1 and 2 strip clusters was found to be 27.4 μm and 21.1 μm for the 134.4 μm and 80 μm sensors respectively. This is better than that expected from pitch/$\sqrt{12}$, and can be attributed to a correlation between cluster width and interstrip position.

Large clusters (>3 strips) were seen, which cannot be accounted for by charge sharing alone. Monte Carlo simulations show that the production of δ-rays within the sensor material contributes to the presence of such large clusters.

Measurements with sensors tilted about the axis parallel to the strips could be used to simulate charged particles of various p_{T} within the high magnetic field of the CMS Tracker. Cluster width has been found to be capable of providing only a very crude selection cut on p_{T}. Hit finding efficiency was seen not to reduce with sensors tilted at 30° (equivalent to $p_{\mathrm{T}} = 0.65$ GeV/c at $r = 540$ mm).

The CBC2 is the next iteration of the chip, and includes on chip correlation logic for the selection of high p_{T} tracks according to hits on two closely spaced sensors.

Chapter 5

Conclusions

The HL-LHC is the proposed luminosity upgrade to the LHC, which will see luminosity increased towards 5×10^{34} $\mathrm{cm^{-2}s^{-1}}$. This presents many challenges to accelerator hardware such as magnets, collimators and cryogenic systems. Upgrades to the machine will follow a phased approach, with much work being undertaken during three long shutdown periods. As well as accelerator components, the LHC experiments will also require significant upgrades in order to maintain performance in the high luminosity environment.

The phenomenon of crystal channeling is one proposed technique that could be used in beam collimation. The use of bent crystals to channel away particles from the beam halo onto downstream absorbers would reduce the damage to accelerator components that would result from amorphous scatter of particles from conventional collimators. A beam telescope was constructed for use with the UA9 collaboration, which could measure the three dimensional trajectories of 400 GeV protons in the presence of a bent crystal. The telescope comprised five pairs of orthogonal silicon strip sensors, and had a readout system based heavily on that of the CMS Tracker. The track reconstruction method used to characterise crystal channeling provided a separate three parameter fit in x and y, giving an upstream angle, downstream angle, and impact position at the crystal. The spatial resolution of each telescope sensor of 6.91 μm, together with the multiple scatter angle of 2.4 μrad, was found to give a resolution on the deflection angle of 5.2 μrad, and a resolution on the incident angle of 2.5 μrad. This performance was sufficient to measure crystal channeling phenomena and make any required angular selection cuts. Observations of crystal channeling in silicon strip crystals have shown channeling efficiency of nearly 50% achievable for a crystal bend angle of 250 μrad, with a 5 μrad cut on incident angle. Results also show a significant reduction in channeling efficiency when a wider angular selection is made, which highlights the important point that a low divergence beam is crucial for efficient beam extraction in a future crystal based collimation system. This will place restrictions on precisely where around the accelerator ring such a system will work optimally.

The relative success of strip crystals over quasi-mosaic crystals in these observations suggests that strip crystals should be favoured for use in collimation, as also noted by the T980 experiment [128]. Through beam tests in the H8, and the subsequent analysis of data, a systematic approach to the study of strip crystals has developed, which can be used in future beam tests to promptly characterise crystal properties such as bend angle, torsion and channeling efficiency. Further studies of advanced crystal concepts will be possible with the telescope. Multiple volume reflection is one such concept, as discussed in Chapter 2. Crystals with decreasing curvature along the beam direction are also of interest as they have been shown to suppress dechanneling [129]. Such crystals can also provide a focussing effect by deflecting particles by different amounts depending on their transverse impact position [129, 130].

Translation of the telescope to a heavy ion beam was not trivial due to the large signals deposited in the sensors (>4000 MIPs). The APV25 readout chips showed the characteristic saturation expected from such large signals. Hit reconstruction needed modification, and a cluster midpoint algorithm was found to be optimal. Track reconstruction could proceed in the same way as with the proton beam. The sensor resolution was seen to be 13.65 μm, which led to a resolution on deflection angle and incident angle of 6.7 μrad and 5.8 μrad respectively. No channeling measurements were made with the heavy ion beam, though the performance of the telescope indicated that this would be possible in the future.

Although the telescope is capable of observing crystal channeling of heavy ions, its performance could be improved. Firstly its angular resolution is largely dominated by the scatter angle of heavy ions. This could be reduced with the use of thinner sensors, without cost to efficiency due to the large signals observed. Also, as well as channeling capabilities the larger nuclear interaction rate expected with heavy ions should be understood. The telescope should therefore be able to measure the trajectories of lower energy secondary particles produced in nuclear interactions, for which the hit finding algorithm would need refining to allow smaller signals to be seen in a saturated APV25 chip.

In addition to tests in the H8 beamline, UA9 has performed tests in the SPS, with good collimation efficiency observed for both protons and lead ions [131, 132]. Plans now are underway to extend UA9 activities to the LHC, with the main goal of allowing a direct comparison of the collimation cleaning efficiency with and without the use of crystals. The proposed experiment is called LUA9 [54]. Operation in the high energy LHC beam presents extra challenges due to concerns over the radiation tolerance of crystals and secondary absorbers. Accidental exposure of a crystal to the nominal beam intensity could have serious implications for crystal integrity, and in these conditions a good understanding of thermal and radiation effects is required. Early tests are encouraging [61], but further post-irradiation studies are foreseen. Additionally, the much smaller channeling acceptance angle necessitates very precise crystal alignment mechanisms [54].

The CMS Tracker will require significant upgrades in preparation for increased luminosity at the HL-LHC. Increased particle flux will lead to greater radiation dose and the need for higher granularity in order to keep occupancies down. A novel challenge will be the inclusion of tracking information in the Level-1 Trigger, which will ensure that the trigger rate can remain sufficiently low without raising p_{T} thresholds beyond suitable levels. The CBC is a prototype for the proposed readout chip for silicon strips in the upgraded CMS Tracker. Its simple binary unsparsified readout architecture will maintain manageable data rates, while also keeping power consumption and cooling requirements down. The CBC has been tested in laboratory and beam test environments and has been shown to perform well, operating within noise and power specification and without errors. CBC modules in the 400 GeV proton H8 beamline have been shown to have good spatial resolution despite the loss of pulse height information. Large clusters, which degrade position resolution, can be largely attributed to δ-ray production within the sensor material. This has been verified through simulation, although no explaination has been found for the abundance of large clusters centred on a particle impact position. Further refinements to the Geant4 simulation may help determine the source of such clusters, and whether or not they are the result of a chip issue. Tilting of the sensors in the beam to simulate various p_{T} values has shown that efficiency remains high at operating thresholds ($\sim$1 fC) for $p_{\mathrm{T}} > 0.65$ GeV/c at $r = 540$ mm. Overall, the chip has performed well and to specification, and has highlighted no significant issues for concern looking ahead to further iterations.

The CBC2 is the next iteration of the chip, and is designed to instrument double layer modules in the outer Tracker. On-chip logic will help identify high p_{T} candidates, or stubs, using cluster width discrimination and by selecting correlated hits between closely separated sensors. Plans are underway to develop a beam telescope comprising CBC2 modules, which will allow evaluation of the performance of the stub-finding logic with various incident angles and sensor separations. Testing of modules containing Level-1 Trigger logic in a high energy beam will represent a significant step in the development of a final Tracker system for use in the HL-LHC.

References

[1] L. Evans and P. Bryant, "LHC Machine," *Journal of Instrumentation* **3** (2008).

[2] The CMS Collaboration, "The CMS experiment at the CERN LHC," *Journal of Instrumentation* **3** (2008).

[3] The ATLAS Collaboration, "The ATLAS Experiment at the CERN Large Hadron Collider," *Journal of Instrumentation* **3** (2008).

[4] The LHCb Collaboration, "The LHCb Detector at the LHC," *Journal of Instrumentation* **3** (2008).

[5] The ALICE Collaboration, "The ALICE experiment at the CERN LHC," *Journal of Instrumentation* **3** (2008).

[6] The CMS Collaboration, "Observation of a new boson at a mass of 125 GeV with the CMS experiment at the LHC," *Physics Letters B* **716** (2012).

[7] The ATLAS Collaboration, "Observation of a new particle in the search for the Standard Model Higgs boson with the ATLAS detector at the LHC," *Physics Letters B* **716** (2012).

[8] LHC Higgs Cross Section Working Group, "Handbook of LHC Higgs Cross Sections: 1. Inclusive Observables," (2011), no. CERN-2011-002,.

[9] The CMS Collaboration, "CMS Physics: Technical Design Report, Volume 1: Detector Performance and Software," *CERN-LHCC* (2006).

[10] R. Fliller *et al.*, “Results of bent crystal channeling and collimation at the Relativistic Heavy Ion Collider,” *Physical Review ST Accelerators and Beams* **9** (2006).

[11] R. Barate *et al.*, “Search for the standard model Higgs boson at LEP,” *Physics Letters B* (2003).

[12] The CMS Collaboration, “CMS Tracker System Project: Technical Design Report,” *CERN-LHCC* (1997).

[13] The CMS Collaboration, “The CMS Magnet Project: Technical Design Report,” *CERN-LHCC* (1997).

[14] M. Pesaresi, *Development of a new Silicon Tracker at CMS for Super-LHC*. PhD thesis, Imperial College, London, 2010.

[15] V. Khachatryan *et al.*, “CMS Tracking Performance Results from early LHC Operation,” *European Physical Journal* (2010).

[16] The CMS Collaboration, “The CMS Electromagnetic Calorimeter Project: Technical Design Report,” *CERN-LHCC* (1997).

[17] M. French *et al.*, “Design and results from the APV25, a deep sub-micron CMOS front-end chip for the CMS tracker,” *Nuclear Instruments and Methods in Physics Research Section A* (2001).

[18] J. Troska *et al.*, “Optical readout and control systems for the CMS tracker,” *Nuclear Science, IEEE Transactions* (2003).

[19] C. Foudas *et al.*, “The CMS Tracker Readout Front End Driver,” *Nuclear Science, IEEE Transactions* **52** (2005).

[20] The I^2C Specification. `http://www.i2c-bus.org/`.

[21] F. Drouhin *et al.*, “The CERN CMS Silicon Strip Tracker Control System,” Tech. Rep. CMS-CR-2004-032, CERN, 2004.

[22] M. Raymond and G. Hall, "CMS microstrip tracker readout at the SLHC," (2008), no. CERN-2008-008,.

[23] E. Cano *et al.*, "CMS data to surface transportation architecture," (2002).

[24] H. Spieler, *Semiconductor Detector Systems*. Oxford University Press, 2006.

[25] M. Raymond *et al.*, "The APV25 0.25 μm CMOS readout chip for the CMS tracker," in *Nuclear Science Symposium Conference Record, 2000 IEEE*. 2000.

[26] The CMS Collaboration, "CMS TriDAS project: Technical Design Report, Volume 1: The Trigger Systems," *CERN-LHCC* (2000).

[27] C. Seez, "The CMS trigger system," *The European Physical Journal C* **34** (2004).

[28] The CMS Collaboration, "CMS TriDAS project: Technical Design Report, Volume 2: Data Acquisition and High-Level Trigger," *CERN-LHCC* (2002).

[29] D. Giordano, "The CMS High-Level Trigger Selection," Tech. Rep. CMS-CR-2004-025, CERN, 2004.

[30] S. Abdullin *et al.*, "Physics potential and experimental challenges of the LHC luminosity upgrade," *European Physical Journal C* **39** (2005).

[31] CMS Collaboration, "Technical proposal for the upgrade of the CMS detector through 2020," Tech. Rep. CERN-LHCC-2011-006. LHCC-P-004, 2011.

[32] L. Rossi and O. Brüning, "High Luminosity Large Hadron Collider: A description for the European Strategy Preparatory Group," tech. rep., CERN, 2012.

[33] F. Zimmermann, "CERN Upgrade Plans for the LHC and its Injectors," *Proceedings of Science* **EPS-HEP2009** (2009).

[34] W. Scandale and F. Zimmermann, "Scenarios for sLHC and vLHC," *Nuclear Physics B - Proceedings Supplements* (2008).

[35] W. Fischer *et al.*, “LHC beam-beam compensation studies at RHIC,” (2010), no. FERMILAB-CONF-09-722-APC,.

[36] G. Hall, “The upgrade programme of the CMS Tracker at SLHC,” *Proceedings of Science* **VERTEX2008** (2008).

[37] R. Bellazzini *et al.*, “Micropattern gas detectors: the CMS MSGC project and gaseous pixel detector applications,” *Nuclear Instruments and Methods in Physics Research Section A* **471** (2001).

[38] J. Whitmore, “CMS Hadron Calorimeter front-end upgrade for SLHC Phase I,” *Nuclear Instruments and Methods in Physics Research Section A* **617** (2010).

[39] W. Erdmann *et al.*, “Upgrade plans for the CMS pixel barrel detector,” *Nuclear Instruments and Methods in Physics Research Section A* **617** (2010).

[40] Micro-TCA Standard `http://www.picmg.org/pdf/MicroTCA_Short_Form_Sept_2006.pdf`.

[41] C. Roland, “Track reconstruction in heavy ion collisions with the CMS silicon tracker,” *Nuclear Instruments and Methods in Physics Research Section A* **566** (2006).

[42] M. Weber, “Power distribution for SLHC trackers: Challenges and solutions,” *Nuclear Instruments and Methods in Physics Research Section A* **592** (2008), no. 12, 44–55.

[43] M. Raymond *et al.*, “The CMS binary chip for microstrip tracker readout at the SLHC,” *Journal of Instrumentation* **7** (2012).

[44] Losito, R and Laface, E and Scandale, W, “The UA9 Experiment at the CERN-SPS,” (2009), no. CERN-ATS-2009-131,.

[45] M. Pesaresi *et al.*, “Design and performance of a high rate, high angular resolution beam telescope used for crystal channeling studies,” *Journal of Instrumentation* **6** (2011).

[46] Jeanneret, J B and Leroy, D and Oberli, L R and Trenkler, T, "Quench levels and transient beam losses in LHC magnets," Tech. Rep. LHC-Project-Report-44, CERN, 1996.

[47] O. S. Bruning *et al.*, *LHC Design Report.* CERN, 2004.

[48] F. Roncarolo, R. Appleby, and R. M. Jones, "Beam Coupling Impedance Studies on LHC FP420 Multi-pocket Beam Pipe Prototype," *Conference Proceedings* **C0806233** (2008).

[49] R. Assmann, J. Jeanneret, and D. Kaltchev, "Efficiency for the imperfect LHC collimation system," (2002).

[50] S. Hasan, *Bent silicon crystals for the LHC collimation: Study with an ultrarelativistic proton beam.* PhD thesis, Universita Degli Studi Dell Insubria, 2007.

[51] R. Assmann *et al.*, "Designing and building a collimation system for the high-intensity LHC beam," 2003.

[52] R. W. Assmann *et al.*, "The final collimation system for the LHC," (2006), no. LHC-PROJECT-Report-919. CERN-LHC-Project-Report-919,. revised version submitted on 2006-09-15.

[53] S. Redaelli, "Do we really need a collimator upgrade," *Conference Proceedings* (2012).

[54] W. Scandale *et al.*, "LHC Collimation with Bent Crystals - LUA9," Tech. Rep. CERN-LHCC-2011-007. LHCC-I-019, CERN, 2011.

[55] E. N. Tsyganov, "Some Aspects of the Mechanism of a Charge Particle Penetration Through a Monocrystal," (1976), no. FERMILAB-TM-0682,.

[56] V. K. V. Biryukov, Y. Chesnokov, *Crystal Channeling and Its Application at High-Energy Accelerators.* Springer, 1997.

[57] A. P. Pathak, "Interatomic potential and energy loss in planar channelling," *Journal of Physics C* **8** (1975).

[58] W. Scandale, D. Still, A. Carnera, G. Della Mea, D. De Salvador, *et al.*, "High-efficiency volume reflection of an ultrarelativistic proton beam with a bent silicon crystal," *Physical Review Letters* **98** (2007).

[59] V. Previtali, *Performance Evaluation of a Crystal-Enhanced Collimation System for the LHC*. PhD thesis, SB, Lausanne, 2010.

[60] A. Baurichter *et al.*, "Channeling of high-energy particles in bent crystals experiments at the cern sps," *Nuclear Instruments and Methods in Physics Research Section B* (2000) 27–43.

[61] A. Lechner *et al.*, "Robustness Test of a Silicon Strip Crystal for Crystal-Assisted Collimation Studies in the LHC," (2013), no. CERN-ACC-2013-0272,.

[62] S. Carturan *et al.*, "Germanium strips for channeling: Study of the crystal quality after slicing and chemical etching," *Materials Chemistry and Physics* **132** (2012), no. 23, 641–651.

[63] V. Biryukov and S. Bellucci, "Nanotube diameter optimal for channeling of high-energy particle beam," *Physics Letters B* **542** (2002) 111–115.

[64] W. Scandale, "Crystal-based collimation in modern hadron colliders," *International Journal of Modern Physics* **A25S1** (2010) 70–85.

[65] C. R. A and J. A. Ellison, *Relativistic channeling*. Springer, 1987.

[66] A. Vodopianov *et al.*, "Control of charged particle trajectories by means of a bent monocrystal," *Journal of Experimantal and Theoretical Physics Letters* **30** (1979) 474–478.

[67] V. Avdeichikov *et al.*, "Output accelerated beam of JINR Synchrophasotron using a curved single crystal," *JINR Rapid Communication* (1984) 1–84.

[68] A. Asseev *et al.*, "Extraction of the 70 GeV proton beam from the IHEP accelerator towards beam line 2(14) with a bent single crystal," *Nuclear Instruments and Methods in Physics Research Section A* **309** (1991), no. 12,.

[69] A. Asseev, E. Myae, S. Sokolov, and Y. Fedotov, “On increasing the bent crystal extraction efficiency by using a thin internal target,” *Nuclear Instruments and Methods in Physics Research Section A* **324** no. 12,.

[70] A. Afonin *et al.*, “The schemes of proton extraction from ihep accelerator using bent crystals,” *Nuclear Instruments and Methods in Physics Research Section B* **234** (2005), no. 12, 14–22.

[71] F. Ferroni, “Proton extraction from the SPS with a bent crystal,” *Nuclear Instruments and Methods* **A351** (1994) 183–187.

[72] R. A. Carrigan, “Crystal extraction at the Tevatron,” (2005).

[73] H. Akbari *et al.*, “First results on proton extraction from the cern-sps with a bent crystal,” *Physics Letters B* **313** (1993), no. 34, 491–497.

[74] X. Altuna *et al.*, “High efficiency multipass proton beam extraction with a bent crystal at the SPS,” *Physics Letters B* **357** (1995) 671–677.

[75] G. Arduini *et al.*, “Deflection and extraction of pb ions up to 33 tev/c by a bent silicon crystal,” *Physical Review Letters* **79** (1997) 4182–4185.

[76] R. A. Carrigan *et al.*, “Extraction from tev-range accelerators using bent crystal channeling,” *Nuclear Instruments and Methods in Physics Research Section B* **90** (1994), no. 14, 128–132.

[77] R. A. Carrigan *et al.*, “First observation of luminosity-driven extraction using channeling with a bent crystal,” *Physical Review ST Accelerators and Beams* **1** (1998).

[78] J. Klem, *Proton extraction from a high-energy beam with bent crystals.* PhD thesis, Helsinki Institute of Physics, 1998.

[79] D. Still *et al.*, “Recent T980 Crystal Collimation Studies at the Tevatron Exploiting a Pixel Detector System and a Multi-Strip Crystal Array,” *Conference Proceedings.* **C1205201** (2012) 559–561.

[80] A. G. Afonin *et al.*, “High-efficiency beam extraction and collimation using channeling in very short bent crystals,” *Physical Review Letters* **87** (2001).

[81] Y. M. Ivanov *et al.*, “Volume reflection of a proton beam in a bent crystal,” *Physical Review Letters* **97** (2006).

[82] S. Baricordi *et al.*, “Optimal crystal surface for efficient channeling in the new generation of hadron machines,” *Applied Physics Letters* **91** (2007).

[83] W. Scandale *et al.*, “First observation of proton reflection from bent crystals,” (2006), no. CERN-AT-2006-007-MAS,.

[84] W. Scandale *et al.*, “Apparatus to study crystal channeling and volume reflection phenomena at the SPS H8 beamline,” *Review of Scientific Instruments* **79** (2008) 023303.

[85] W. Scandale and otehrs, “Observation of nuclear dechanneling for high-energy protons in crystals,” *Physics Letters B* **680** (2009), no. 2, 129–132.

[86] W. Scandale *et al.*, “Volume reflection dependence of 400 gev/c protons on the bent crystal curvature,” *Physical Review Letters* **101** (2008).

[87] E. Scandale *et al.*, “First observation of multiple volume reflection by different planes in one bent silicon crystal for high-energy protons,” *Physics Letters B* **682** (2009), no. 3, 274–277.

[88] W. Scandale *et al.*, “High-efficiency deflection of high-energy protons through axial channeling in a bent crystal,” *Physical Review Letters* **101** (2008) 164801.

[89] R. Fliller *et al.*, “RHIC crystal collimation,” *Nuclear Instruments and Methods in Physics Research Section B* **234** (2005), no. 12, 47–56.

[90] R. A. Carrigan and other, “Channeling collimation studies at the Fermilab Tevatron,” *Proc. SPIE International Society for Optical Engineering* **6634** (2007).

[91] W. Scandale *et al.*, “The UA9 experimental layout,” *Journal of Instrumentation* **6** (2011).

[92] M. Fiorini *et al.*, “Experimental Study of Crystal Channelling at CERN-SPS for Beam-Halo Cleaning,” (2006), no. CERN-AT-2006-009,.

[93] A. Mazzolari *et al.*, “Fabrication of Silicon Strip Crystals for UA9 Experiment,” *Conference Proceedings* **C100523** (2010), no. IPAC-2010-THPEC080,.

[94] W. Scandale *et al.*, “Apparatus to study crystal channeling and volume reflection phenomena at the SPS H8 beamline,” *Review of Scientific Instruments* **79** (2008).

[95] Y. Ivanov, A. Petrunin, and V. Skorobogatov, “Observation of the elastic quasi-mosaicity effect in bent silicon single crystals,” *Journal of Experimental and Theoretical Physics Letters* **81** (2005).

[96] V. Brigljevic *et al.*, “FEDkit: A Design Reference for CMS Data Acquisition Inputs,” Tech. Rep. CMS-CR-2003-036, CERN, 2003.

[97] V. Brigljevic *et al.*, “Using XDAQ in application scenarios of the CMS experiment,” *eConf* **C0303241** (2003).

[98] M. Pentia, G. Iorgovan, and A. Mihul, “Multiple scattering error propagation in particle track reconstruction,” *Romanian Journal of Physics* **40** (1995).

[99] W. T. Scott, “The Theory of Small-Angle Multiple Scattering of Fast Charged Particles,” *Reviews of Modern Physics* (1963).

[100] J Beringer et al. (Particle Data Group) *Physical Review D* (2012).

[101] K. Banzuzi *et al.*, “Performance and calibration studies of silicon strip detectors in a test beam,” *Nuclear Instruments and Methods in Physics Research Section A* **453** (2000).

[102] J. Jowett, R. Bruce, and S. Gilardoni, “Luminosity Limit from Bound-Free Pair Production in the LHC,” in *Particle Accelerator Conference.* 2005.

[103] W. Adam *et al.*, "The effect of highly ionising particles on the CMS silicon strip tracker," *Nuclear Instruments and Methods in Physics Research Section A* **543** (2005).

[104] M. Huhtinen, "Highly ionising events in silicon detectors," Tech. Rep. CMS-NOTE-2002-011, CERN, 2002.

[105] R. Bainbridge *et al.*, "The Effect of Highly Ionising Events on the APV25 Readout Chip," Tech. Rep. CMS-NOTE-2002-038, CERN, 2002.

[106] I. R. Tomalin, "Test-Beam Analysis of the Effect of Highly Ionising Particles on the Silicon Strip Tracker," Tech. Rep. CMS-NOTE-2003-025, CERN, 2003.

[107] L. Gatignon, "Magnets Kit for the Experimental Areas of the CERN PS/SPS complex," Tech. Rep. CERN-OPEN-2004-003, CERN, 1991.

[108] D Braga and others, "CBC2: a microstrip readout ASIC with coincidence logic for trigger primitives at HL-LHC," *Journal of Instrumentation* **7** (2012).

[109] S. Bonacini, K. Kloukinas, and P. Moreira, "E-link: A Radiation-Hard Low-Power Electrical Link for Chip-to-Chip Communication," (2009).

[110] Dabrowski, W. and others, "Design and performance of the ABCD chip for the binary readout of silicon strip detectors in the ATLAS semiconductor tracker," in *Nuclear Science Symposium, IEEE*. 1999.

[111] L. Jones, "CMS Binary Chip User Guide," (2010).

[112] G. Iles, "The APV Emulator to Prevent Front-End Buffer Overflows Within the CMS Silicon Strip Tracker," `CERN-LHCC/2002-034`.

[113] H. Bichsel, "Straggling in thin silicon detectors," *Reviews of Modern Physics* **60** (1988).

[114] H. Bichsel, "A method to improve tracking and particle identification in TPCs and silicon detectors," *Nuclear Instruments and Methods in Physics Research Section A* **562** (2006).

[115] S. Hancock *et al.*, "Energy loss and energy straggling of protons and pions in the momentum range 0.7 to 115 GeV/c," *Physical Review A* **28** (1983).

[116] F. Campabadal, "Beam tests of ATLAS SCT silicon strip detector modules," *Nuclear Instruments and Methods in Physics Research Section A* **538** (2005).

[117] G. Hall, "Ionisation energy losses of highly relativistic charged particles in thin silicon layers," *Nuclear Instruments and Methods in Physics Research* **220** (1984).

[118] R. M. Sternheimer, "Density effect for the ionization loss of charged particles," *Physical Review* **145** (1966).

[119] K. H. Weber, "An easy distance-energy-relationship for electrons in the energy range from 3 keV to 3 MeV," *Nuclear Instruments and Methods* **25** (1964).

[120] G. Cirrone *et al.*, "Validation of the Geant4 electromagnetic photon cross-sections for elements and compounds," *Nuclear Instruments and Methods in Physics Research Section A* **618** (2010), no. 13, 315–322.

[121] S. Chauvie *et al.*, "Geant4 low energy electromagnetic physics," in *Nuclear Science Symposium Conference Record, 2004 IEEE*, vol. 3, pp. 1881–1885. 2004.

[122] D. E. Cullen *et al.*, "EPDL97: the Evaluated Photon Data Library, 1997 Version," (1997).

[123] S. T. Perkins, D. E. Cullen, and D. E. Seltzer, *Tables and graphs of electron-interaction cross sections from 10 eV to 100 GeV derived from the LLNL Evaluated Electron Data Library (EEDL), Z=1-100.* Lawrence Livermore National Laboratory, Livermore, CA, 1991.

[124] S. T. Perkins, M. H. Chen, D. E. Cullen, and J. H. Hubbell, *Tables and graphs of atomic subshell and relaxation data derived from the LLNL Evaluated Atomic Data Library (EADL), Z=1-100.* Lawrence Livermore National Laboratory, Livermore, CA, 1991.

[125] S. Agostinelli *et al.*, "Geant4 a simulation toolkit," *Nuclear Instruments and Methods in Physics Research Section A* **506** (2003), no. 3, 250–303.

[126] "Measurement of delta-rays in ATLAS silicon sensors," Tech. Rep. ATLAS-CONF-2013-005, CERN, 2013.

[127] S. Mersi *et al.*, "CMS Tracker layout studies for HL-LHC," Tech. Rep. CMS-CR-2011-362, CERN, 2011.

[128] V. Zvoda *et al.*, "Advanced Bent Crystal Collimation Studies at the Tevatron T-980," *Conference Proceedings* **C110328** (2011) 73–75.

[129] A. Afonin *et al.*, "A device based on a bent crystal with a variable curvature for controlling particle beams at accelerators," *Instruments and Experimental Techniques* **56** (2013) 123–129.

[130] M. A. Gordeeva *et al.*, "First results on the focusing of a 70-GeV proton beam by a curved single crystal," *Soviet Journal of Experimental and Theoretical Physics Letters* **54** (1991).

[131] W. Scandale, "UA9 Results from Crystal Collimation Tests in the SPS & Future Strategy," Tech. Rep. EuCARD-REP-2013-002, 2013.

[132] W. Scandale *et al.*, "Comparative results on collimation of the SPS beam of protons and Pb ions with bent crystals," *Physics Letters B* **703** (2011).